2019

Wettability of quartz surfaces under carbon dioxide geo-sequestration conditions. A theoretical study

Aleksandr Abramov

Edith Cowan University

Copyright Warning

Wettability of Quartz Surfaces under Carbon Dioxide Geo-Sequestration Conditions. A Theoretical Study

Aleksandr Abramov

Submitted for the Degree of
Doctor of Philosophy

Edith Cowan University

School of Engineering

2019

Abstract

The wettability of rocks under reservoir conditions is important to ensure and secure long term underground storage of carbon dioxide. The composition of those rocks vary significantly and are influenced by the fact that quartz is the second most abundant mineral in the earth's continental crust. Thus, the CO_2 wettability of quartz dominates the overall CO_2 trapping performance of storage and cap rocks. If depleted oil or gas reservoirs are used for storage of CO_2 quartz surfaces of rocks in reservoirs which have been previously exposed to hydrocarbons might be covered with chemisorpt hydrocarbon molecules. The CO_2 wettability of these chemically modified quartz is studied in this work with molecular dynamics.

To model quartz surfaces with chemisorpt hydrocarbons both CLAYFF and DREIDING force fields are coupled at atomic site charge level using the density functional theory and the Bader charge analysis. Augmented with modified charges of the OC bond, CLAYFF and the DREIDING force fields are applied to solve the practical problem of calculating the contact angle of a water droplet on alkylated quartz surfaces in a CO_2 environment. A systematic computational study of wettability of fully hydroxylated and alkylated (001) α-quartz surface in carbon dioxide atmosphere with respect to surface concentration of pentyl groups is performed. Alkylated quartz surfaces have been shown to be extremely hydrophobic even when the surface density of hydroxyl groups is close to the highest naturally observed. The study also verifies that a comprehensive description of wettability of alkylated quartz surface requires three parameters: the theoretical contact angle, the apparent contact angle and the hidden contact angle. These contact angles are determined at the tip level of pentyl groups and the level of the quartz surface. The hidden contact angle is calculated as the angle of a water "skirt", which is formed between the level of the quartz surface and the tip level of pentyl groups.

Additionally, the concept and the method of how to determine computational contact angles of a liquid droplet resting on a solid surface from individual snapshots of molecular dynamics simulations have been formulated, implemented and analysed in this work. Spherical coordinates to circumscribe a sphere around given configuration of water molecules form the basis of the method, which is thus natural and consistent with the droplet's geometric computational framework.

Declaration

I certify that this thesis does not, to the best of my knowledge and belief:

i. incorporate without acknowledgment any material previously submitted for a degree or diploma in any institution of higher education;
ii. contain any material previously published or written by another person except where due reference is made in the text of this thesis; or
iii. contain any defamatory material.

Aleksandr Abramov

27/07/2019

Acknowledgments

This work was supported by Edith Cowan University Petroleum Engineering PhD Scholarship and by resources provided by the Pawsey Supercomputing Centre with funding from the Australian Government and the Government of Western Australia.

Table of Contents

List of tables

List of figures

1. Introduction

1.1. Scope and objective

Carbon geo-sequestration is a viable mitigation strategy to tackle consequences of excessive anthropogenic emissions of carbon dioxide (IPCC, 2005). The strategy, among other options, relies on depleted oil or gas reservoirs as possible storage formations. After being exposed to hydrocarbons, cap rocks of these formations may undergo chemical transformations, which change their wettability (Ali et al., 2019) and thus capacity, reliability and security of the structural and residual trapping (Stefan Iglauer, Pentland, & Busch, 2014). The aim of this work is to understand influence of these chemical transformations on the wettability of quartz surfaces in presence of carbon dioxide and to quantify this influence.

1.2. Methods, procedures and process

To study the effects of chemisorpt hydrocarbons on the wettability of the hydroxylated quartz a range of methods of computational chemistry, materials science and solid state physics is used. Known and reliable force fields (Cygan, Liang, & Kalinichev, 2004; Mayo, Olafson, & Goddard, 1990; van Beest, Kramer, & van Santen, 1990) are adapted to the new chemical environments using the density functional theory (Hohenberg & Kohn, 1964; Kohn & Sham, 1965). Investigation on how the surface density of alkyl groups affects quartz's wettability in carbon dioxide atmosphere is then performed using classical molecular dynamics (Gonzalez, 2011). A possibility to use spheroidal geometric constructions to calculate the contact angle using individual snapshots of molecular dynamics simulations is studied with the most stable surface of the pristine quartz.

1.3. Results, observations and conclusions

Insights gained at the molecular level indicate that the wettability of alkylated quartz is a complex phenomenon complete characterisation of which requires a number of parameters. Reported contact angles obtained at different surface levels are compared with the contact angle that is most likely to be measured in an experiment. Quantitative confirmation of the hydrophobicity of the hydroxylated and alkylated quartz is obtained.

1.4. Novel and additive information

This research contributes to the scientific and engineering community in two ways. Firstly, there is a fundamental contribution in the form of modified and adapted for the modelling of

the alkylated quartz force fields. Secondly, there is a practical contribution in the form of a deeper understanding of the wetting processes of chemically modified with hydrocarbons quartz surfaces. Reported quantification of the wettability of the latter surfaces with respect to the concentration of alkyl groups is of particular importance for the engineering applications and development of effective carbon geo-sequestration projects.

1.5. Thesis organization

The dissertation is organized as follows. In chapter two author presents an overview of information in existing literature on the subject of climate change, carbon capture and storage technology, parameters affecting applicability and efficiency of the technology, specifically the contact angle in quartz-water-carbon dioxide systems. The chapter ends with a summary of identified knowledge gaps. In chapter three an overview of existing computational methods utilized to eliminate the knowledge gaps is given. The following chapters are organized as self-sufficient and potentially publishable summaries of research results obtained as independent and yet connected to each other parts of this project. In chapter four a possibility of using spheroidal geometric constructions for calculation of the contact angle is explored. The most stable pristine quartz surface is used as a proving ground for proposed in the chapter method. In chapter five an oxygen-carbon bond connecting quartz crystal to alkyl rest is modelled using the density functional theory. Charges on both atoms of the bond are estimated using the Bader charge analysis. In chapter six a systematic study of wettability of hydroxylated and alkylated quartz with respect to the surface pentyl density is performed. From chapter four through chapter six, the narrative thus naturally proceeds from development of a method to calculate the contact angle of a spherical droplet (chapter four), to a solution of encountered scientific problem of adapting known force fields to chemical environments of studied alkylated quartz surfaces (chapter five), and finally to application of modified contact angle calculation method and modified force fields to systematic study of wettability of alkylated quartz (chapter six). The work is concluded in chapter seven.

1.6. Publications

A. Abramov, S. Iglauer, "Analysis of individual molecular dynamics snapshots simulating wetting of surfaces using spheroidal geometric constructions", accepted for publication in The Journal of Chemical Physics.

A. Abramov, S. Iglauer, "Application of the CLAYFF and the DREIDING force fields for modelling of alkylated quartz surfaces", Langmuir, DOI: 10.1021/acs.langmuir.9b00527, URL: https://pubs.acs.org/doi/10.1021/acs.langmuir.9b00527.

A. Abramov, A. Keshavarz, S. Iglauer, "Wettability of fully hydroxylated and alkylated (001) alpha-quartz surface in carbon dioxide atmosphere", Journal of Physical Chemistry C, DOI: 10.1021/acs.jpcc.9b00263, URL: https://pubs.acs.org/doi/10.1021/acs.jpcc.9b00263.

2. Literature review

2.1. Global warming

2.1.1. Overview

Operating for over than 30 years (since 1988) an intergovernmental scientific body - The Intergovernmental Panel on Climate Change (IPCC) unambiguously links human industrial activity (Figure 1) and changes in the climate and ecosystems observed globally (Figure 2, Figure 3). The IPCC uses recorded from 1850 instrumental measurements and data derived from paleoclimate archives to set a long-term context (IPCC, 2013). As Figure 1 shows industrial activity of the civilization manifests itself in exponentially growing emissions of carbon dioxide, which reach 10 GtC per annum. Action of natural CO_2 sinks significantly mitigated the impact, but from 1800 measured atmospheric growth rate of CO_2 have been steadily increasing and reached more than 3 GtC per annum, Figure 1. These anthropogenic emissions result in 25% increase in CO_2 concentration over a period of 50 years, from 1960 to 2010, Figure 2. Increased carbon dioxide concentrations are consistently observed in the Northern and Southern Hemispheres. Higher content of the acid gas in the atmosphere also leads to increased ocean acidity; reduced pH levels have been recorded for several decades in a row (IPCC, 2013), Figure 2.

Numerous indicators demonstrate that Earth's climate is changing (warming), and from 1950 trends of the change are steady and the rate is alarming, Figure 3: land surface temperature increased by 1°C, sea surface temperature increased by 0.3°C, marine air temperature increased by 0.4°C, sea level increase by more than 100 mm, summer arctic sea-ice extent decreased by $5 \cdot 10^6$ km^2. Increasing trends are also demonstrated by tropospheric temperature, ocean heat content and specific humidity; decreasing trends are observed for Northern Hemisphere snow cover and glacier mass balance, see Figure 3. Thus, collected and analysed by the intergovernmental body paleoclimate data shows clear connection between CO_2 concentration and global temperature. With more than 40% CO_2 concentration increase since preindustrial times, atmospheric CO_2 content became higher than it has ever been over the past 800 000 years (more than 410 ppm in 2018 (scripps.ucsd.edu)). Every of the past three decades had been warmer than the previous decades since 1950, with the first decade of the twenty first century been the warmest of all (IPCC, 2013).

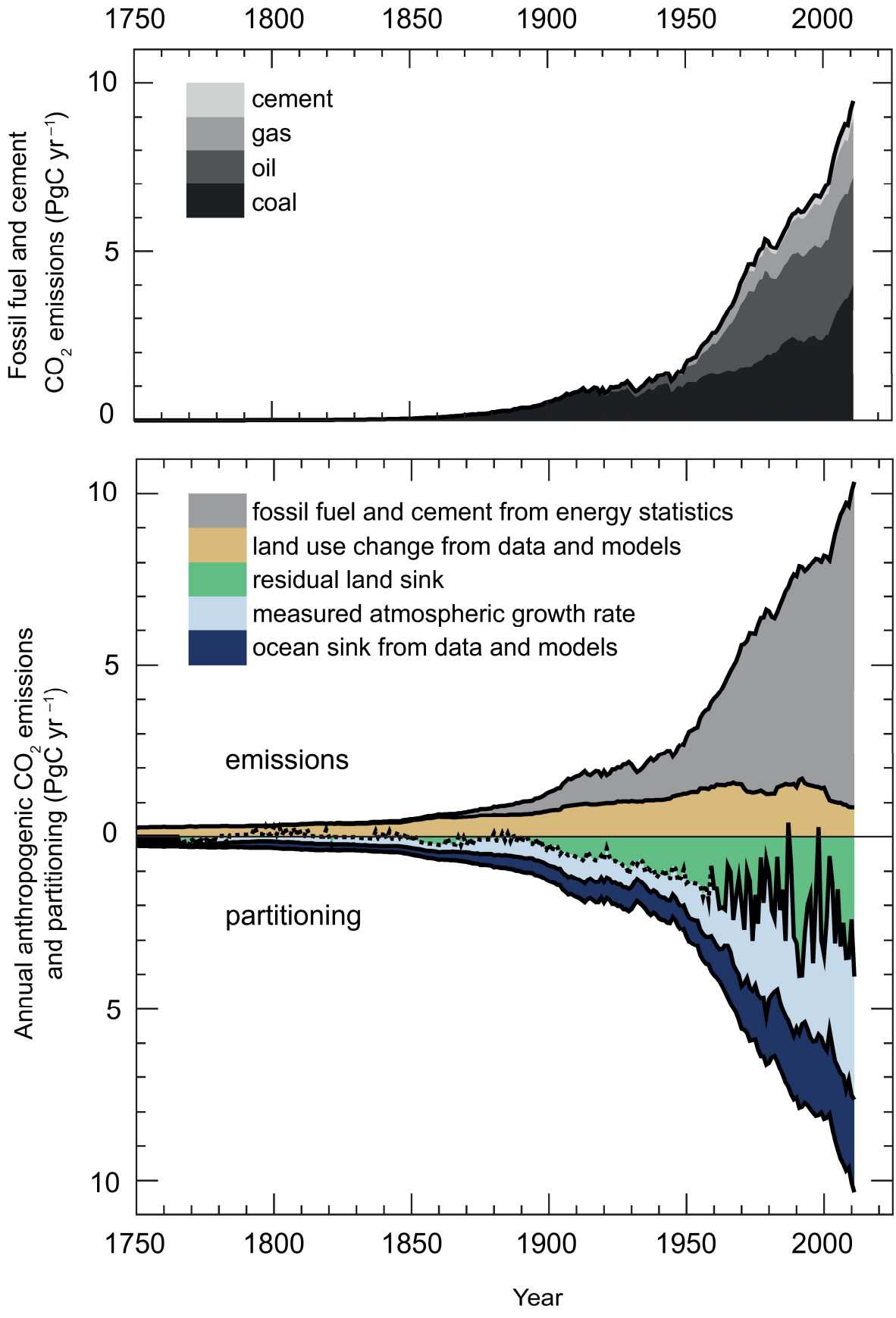

Figure 1. Emissions of carbon dioxide due to industrial and agricultural activities (1 Petagram of carbon = 1 PgC = 10^{15} grams of carbon = 1 Gigatonne of carbon = 1 GtC). Image source: (IPCC, 2013).

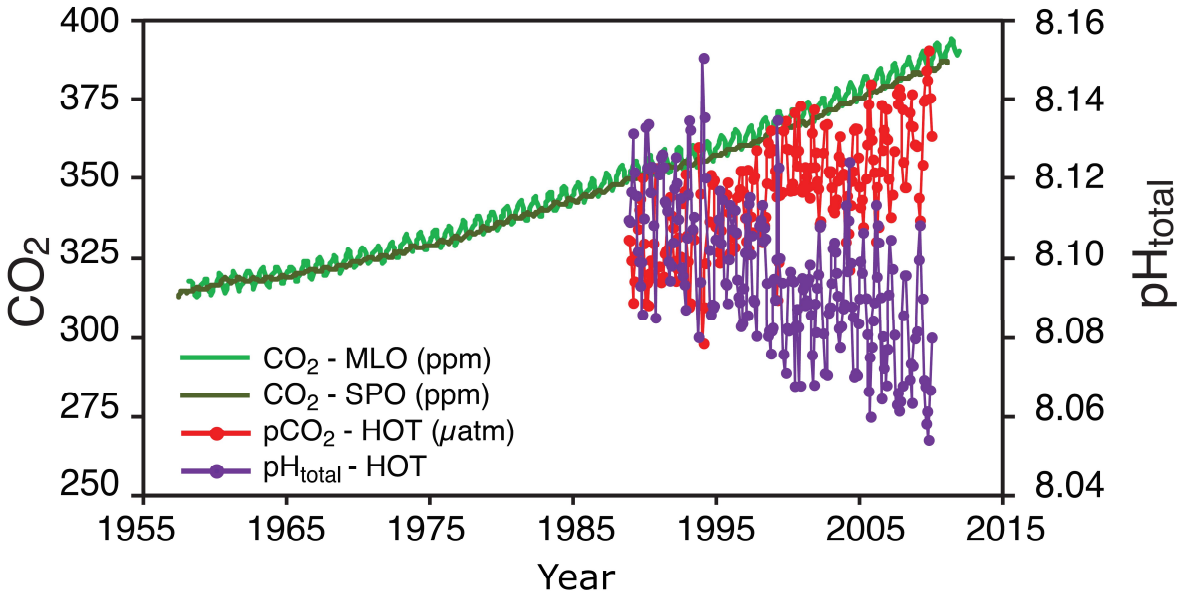

Figure 2. Atmospheric CO_2 concentration, CO_2 partial pressure (pCO_2, left axis) and pH of oceanic surface. MLO: Mauna Loa Observatory, Hawaii; SPO: South Pole; HOT: Hawaii Ocean Time-Series station. Image source: (IPCC, 2013).

This warming is explained by increased heat uptake from the sun by the climate system. The difference between absorbed and reflected energy, i.e. the radiative forcing, has been increasing with increase in CO_2 concentration due to anthropogenic industrial activity. In fact, the increase in the atmospheric concentration of CO_2 since 1750 is the largest contributor to the total radiative forcing. As a result of warming caused by anthropogenic radiative forcing ice sheets and glaciers are losing mass. Arctic sea ice area has been declining since 1980, as well as the Greenland ice sheet. With smaller snow and ice area more of sun's heat is absorbed by the land and oceans, which creates an alarming positive feedback influencing the climate system.

Existing climate system trends, see Figure 3, led the IPCC to the following conclusions (IPCC, 2013): (i) warming in the climate system is undeniable; (ii) human influence on the climate system is clear; (iii) continued greenhouse gases emission causes further climate change and long term negative consequences. Limiting the climate change requires significant and permanent reduction of greenhouse gases emission.

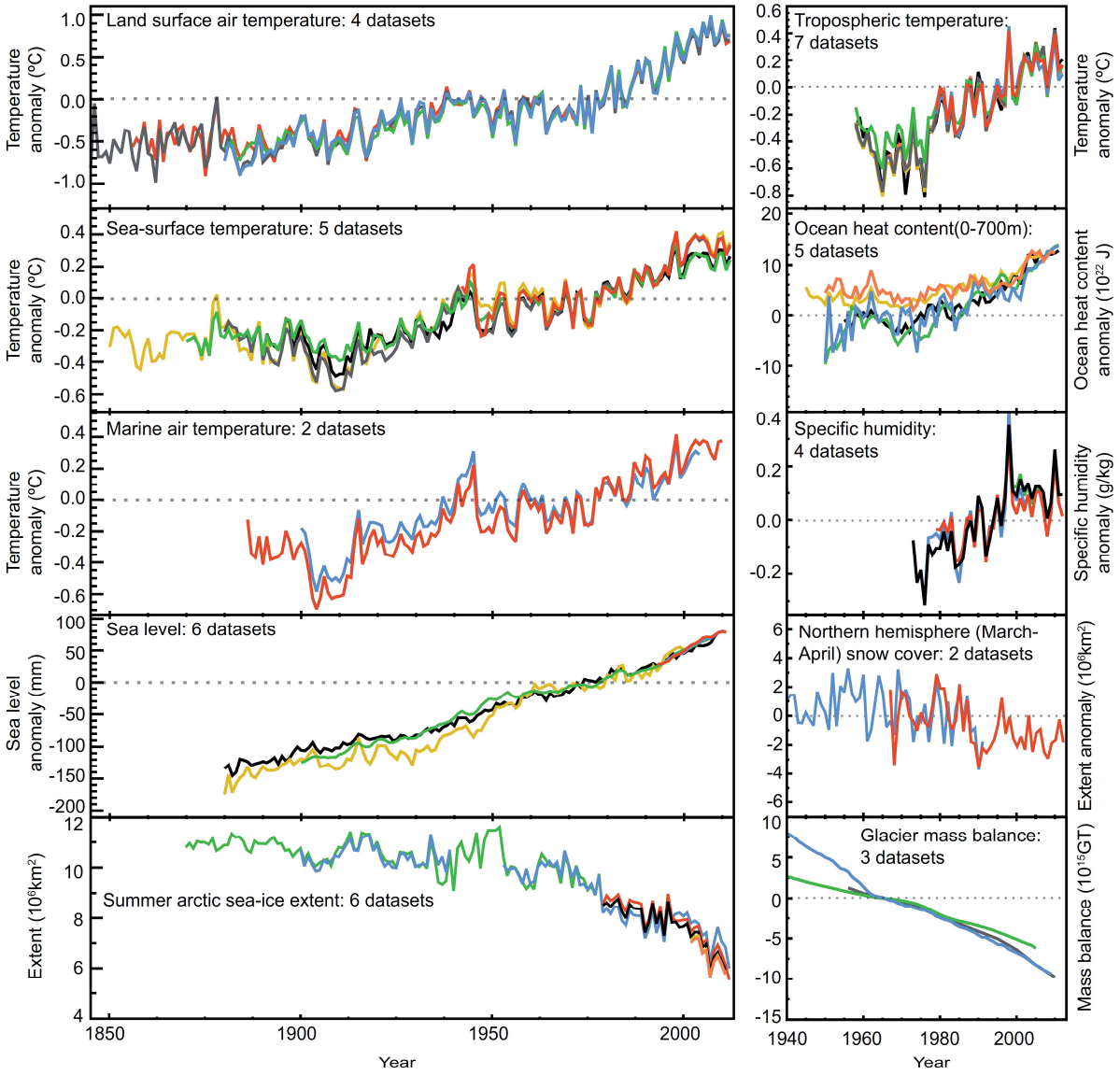

Figure 3. Climate change indicators. Image source: (IPCC, 2013).

Greenhouse gases emission causes the primary effect of the climate change - the warming. There are number of secondary effects among which are the following, see Figure 2 and Figure 3: rise of sea levels, increase in oceans acidity, change of weather and precipitation patterns, spread of tropical diseases, to list some. Mentioned global processes are intrinsically negative, although some local effects may be considered as to say "positive", such as appearance of new sea routes and accessibility of otherwise ice covered areas, warmer winters and reduced energy consumption for heating. The net worldwide outcome of these developments is believed to be extremely negative and catastrophic.

In October 2018 the IPCC issued a special report "Global warming of 1.5°C" (IPCC, 2018), where the authors argue that increase in global temperature above 1.5°C, which is estimated

to happen around 2030 if current trends of CO_2 emission are preserved, could render the planet unsuitable for living in long term due to irreversible changes, such as the loss of ecosystems. A Greenpeace representative summarized the report in three words written in capital letters: "ACT NOW, IDIOTS" (www.bbc.com).

2.1.2. Response strategies

Apart from a passive strategy of doing nothing regarding the climate change it is possible to single out several active strategies which can be used on their own or in combination (IPCC, 2014): (i) adaptation; (ii) mitigation and (iii) climate engineering.

As the word "adaptation" suggests the corresponding strategy implies changing the living environment so it better fits warmer conditions. These changes may include usage of heat resistant and less water demanding plants, flood protective structures, higher foundations and street levels, light coloured roofs, weather control techniques, to name a few.

The mitigation strategies can be developed on premises that emission of greenhouse gases originates from energy production satisfying certain energy consumption, improvements can be implemented on both sides. Limiting energy consumption measures include altering behaviour, lifestyle and diet of the population (mode and demand for mobility, households' energy use, choice of longer-lasting products, reduction in food wastes), as well as energy conservation and energy efficiency. According to the IPCC these are the key mitigation strategies on the energy demand side to limit CO_2 concentration to about 450 ppm by 2100 (IPCC, 2014). On the energy supply side reducing the carbon intensity (decarbonizing) of electricity generation is crucial to achieve cost-effective mitigation of negative consequences of the climate change. This can be accomplished by switching the energy production to renewable sources and specifically to nuclear energy, which share of world electricity generation has been in decline since 1993 (IPCC, 2014). If such switch in energy production is not feasible in certain locations, then large CO_2 emitters can be equipped with carbon capture and storage facilities which remove carbon dioxide from the exhaust fumes. In addition to these measures natural or artificial reservoirs absorbing carbon dioxide, or carbon sinks, can be preserved, enhanced or created. Oceans (at the expense of acidification) and forests are among the largest carbon sinks.

Special case of a mitigation strategy is the climate engineering or geoengineering. The strategy is largely represented by two subcategories: solar radiation management and removal of CO_2 from the atmosphere. The former method aims to reflect part of incoming sun light back to space. The letter method is analogous to the carbon capture and storage although it deals with very low CO_2 concentrations due to which it is much less efficient.

2.2. Carbon capture and storage

2.2.1. Overview

Carbon dioxide Capture and Storage (CCS) technology can reduce CO_2 emissions of fossil fuel power plants, where the gas is captured, transported to a place of storage and isolated from the atmosphere deep underground (Bachu, 2003; GCCSI, 2018; IPCC, 2005). The technology is appealing as it can be used on already operating power stations, as well as on prospective ones. The capturing is the most efficient when it is done at the emission source where three different types of capture systems may be applied: (i) post-combustion; (ii) pre-combustion and (iii) oxyfuel combustion (IPCC, 2005). In the first system CO_2 removed after combustion of organic or fossil fuels. In the second system carbon based fuel is partially oxidised to form hydrogen and carbon monoxide, which then reacts with water to form CO_2 and hydrogen. CO_2 is next removed to leave hydrogen for further processing or combustion. In the oxyfuel (or oxy-firing) combustion fuel is burnt in pure oxygen which produces only CO_2 and water. The first two systems are used by the industry for purposes different from the CCS, the third system is in demonstration stage.

To separate CO_2 from fume gases absorption, adsorption or membrane technologies can be applied. Out of three methods absorption via amine scrubbing is the most mature and widely used by the industry technology, for example, in natural gas processing. After separation CO_2 is transported in supercritical state using existing or specially constructed pipeline networks to a place of storage where it is then injected into a geological formation at depth below 800 m (IPCC, 2005). This formation may be an oil reservoir where CO_2 is used for the enhanced oil recovery or it may be specially dedicated for CO_2 storage formation, see Figure 4.

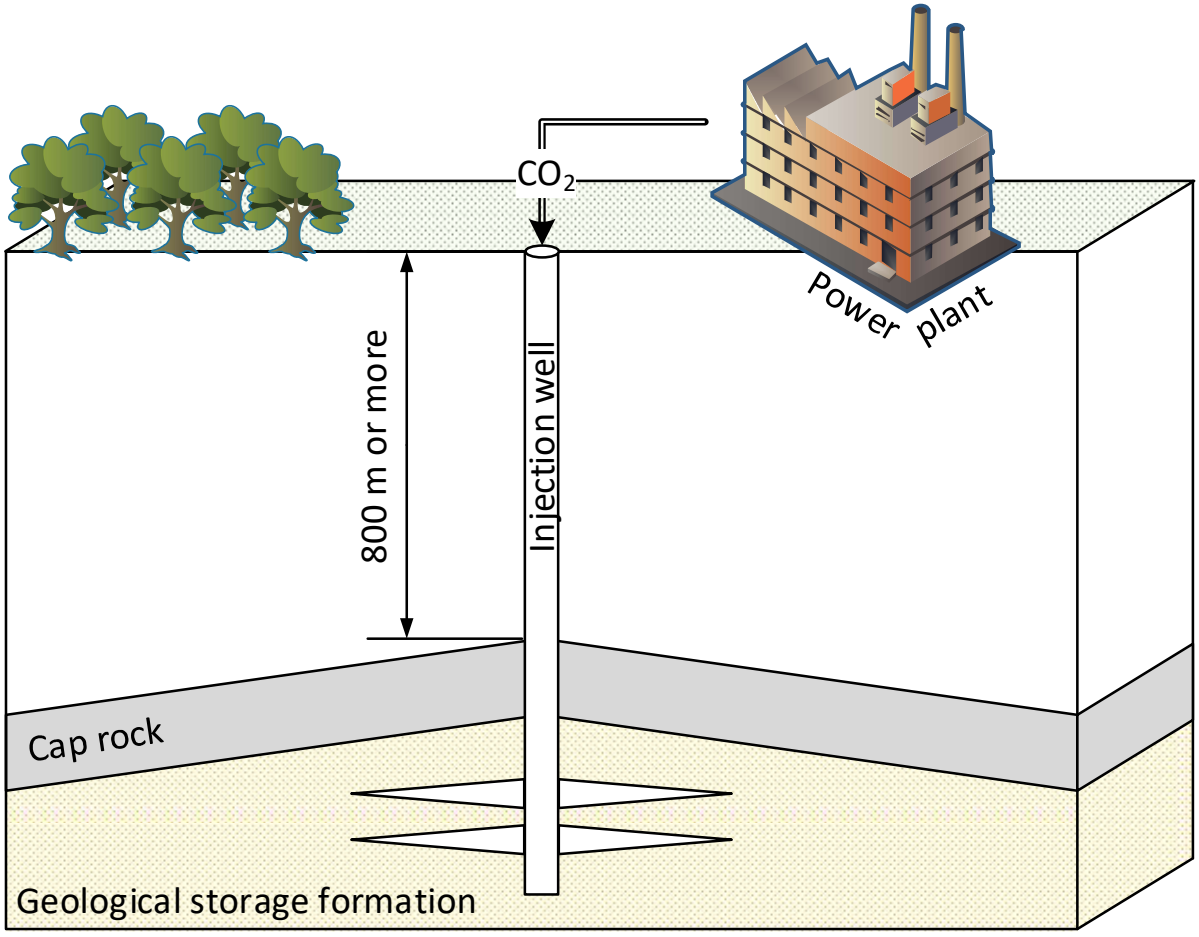

Figure 4. Schematic illustration of carbon dioxide capture and storage technology. Geological storage formations may vary and can be selected from specially dedicated for storage formations, depleted oil or gas reservoirs, deep aquifers, coal beds or salt caverns.

The storage formation must be determined carefully (Bachu, 2003) so that acting trapping mechanisms prevent CO_2 from leaking back to the surface because of its buoyancy. Four trapping mechanisms have been identified and are being actively studied: (i) structural trapping; (ii) residual trapping; (iii) solubility (or dissolution) trapping and (iv) mineral trapping (Stefan Iglauer et al., 2014).

The structural trapping is well understood mechanism preventing upward hydrocarbon migration. Over geological timescale oil, gas or both accumulate and separate from water beneath impenetrable cap rocks. As with hydrocarbons these natural seals stop low density supercritical CO_2 from moving toward the surface retaining it underground. It should be noted that actual seal configuration does not have to be dome like, overlaying along geological faults seal formations can play similar role.

In the residual trapping micrometre sized bubbles of CO_2 disconnected from the main body of the gas are immobilised in the pore space of the storage formation. CO_2 mobility is halted by the capillary forces which balance or exceed the buoyancy forces.

In the solubility or dissolution trapping some portion of CO_2 dissolves into water present in the pore space of surrounding rocks. This causes increase in water density and its corresponding downward motion.

The mineral trapping refers to formation of minerals which are produced as a result of chemical reactions between CO_2, water, ions present in water and rocks of the storage reservoir. Reacted CO_2 becomes permanently captured in the solid phase.

Among the major difficulties reducing confidence in the carbon capture and storage technology is limited ability to robustly predict storage security of the first two trapping processes.

2.2.2. Carbon geo-sequestration projects

The Global CCS Institute (GCCSI) headquartered in Melbourne, Australia (www.globalccsinstitute.com), in its CO_2RE database identifies 23 large-scale CCS projects already operating or under construction, with additional 28 pilot and demonstration projects conceived or functioning (GCCSI, 2018). These facilities capture 43 Million Tonnes Per Annum (MTPA) of CO_2.

The current level of development in CCS technology was reached in more than 45 years. Enhanced oil recovery (EOR) pioneered practical implementations of CCS in 1972 with Val Verde EOR facility in the Sharon Ridge oilfield in Texas. Governmental regulations introduced in Norway in 1991 motivated Statoil to start the Sleipner CO_2 storage facility in 1996, which became the first in the world project where CO_2 was injected into a dedicated geological formation. Injection of CO_2 on the Snohvit gas field, which started in 2008, was required by a license condition also imposed by the Norwegian State. In Weyburn and Midale oil fields in Canada CO_2 have been injected for EOR from 2000 and 2005, respectively. The In Salah CO_2 storage facility in Algeria injected carbon dioxide into the Krechba formation, a depleted gas reservoir, from 2004 to 2010. Over the next five years geochemical, geophysical and production techniques were applied to observe the CO_2 storage process. Obtained data was then used to improve modern monitoring, modelling and verification methodologies.

The second decade of the twenty-first century was the most fruitful in terms of CCS applications in diverse industrial areas and reached sequestration capacity. The technology is now in use in coal-fired power plants, iron and steel factories, chemical and hydrogen production plants.

The first large-scale carbon capture facility in power generation was commenced in 2014 with reconstructed Unit 3 of Boundary Dam Power Station in Saskatchewan province in western Canada (1 MTPA). The first commercial application of CCS in the oil sands industry was also achieved in Canada by Shell in cooperation with the Canadian Federal Government and the Provincial Government of Alberta in 2015 in the Quest facility (1 MTPA).

After 2009 six large-scale CO_2 sequestration facilities began operation in the US. Launched in 2017 the Illinois industrial CCS facility uses dedicated storage (1 MTPA), other five capture and storage units operate in EOR mode: Century natural gas processing plant (8.4 MTPA), Air Products hydrogen production steam methane reformer (1 MTPA), Coffeyville gasification plant producing fertilisers (1 MTPA), Lost Cabin natural gas processing plant (0.9 MTPA), Petra Nova coal-fired power plant with carbon capture (1.4 MTPA).

In Brazil Petrobras started operating CCS facilities in Santos Basin in 2015. In 2017 ten floating production storage and offloading units at the Lula, Sapinhoa and Lapa fields were injecting CO_2 for EOR (2.5 MTPA).

In Saudi Arabia the Uthmaniyah facility was functioning since 2015. CO_2 from a natural gas processing plant is used for EOR on the largest in the world Ghawar field (0.8 MTPA).

The first large-scale CCS facility in the iron and steel industry started operation in 2016 in the United Arab Emirates. The Emirates Steel Industries factory in Mussafah captures and transports CO_2 to Abu Dhabi National Oil Company for EOR (0.8 MTPA).

The EOR project in Jilin oilfield in China was in development since 1990. This first large-scale CCS facility operating in China entered Phase III in 2018 (0.6 MTPA).

The Gorgon liquefied natural gas project in Australia involving the development of the Greater Gorgon gas fields, in some of which the natural gas contains high concentrations of CO_2, is expected to capture and reinject up to 4 MTPA of CO_2 upon completion.

2.3. Wettability and carbon dioxide storage capacity of rocks

Reliability and long term security of the structural and the residual trapping mechanisms are strongly influenced by the wettability of storage formations in CO_2 atmosphere and related capillary effects. The wettability or wetting may intuitively be understood as an ability of a liquid to spread over a solid surface. The degree of spreading is determined by a balance between adhesive and cohesive forces. The macroscopic phenomenon of wetting essentially originates from intermolecular interactions occurring when the liquid and the solid are brought in contact with each other. It is implied that apart from contacting liquid and solid a third party is in play - the gas in which wetting is observed. In such a setup wettability of the solid may be understood as its preference to be in contact with or to be wet by either of two fluids the liquid or the gas.

Wettability can quantitatively be characterised by the contact angle given by the Young equation, which expresses thermodynamic equilibrium between three phases - the solid phase, the liquid phase and the gas phase (Atkins & De Paula, 2006):

$$cos\theta = \frac{\gamma_{SL} - \gamma_{SG}}{\gamma_{LG}},$$

where θ is the contact angle, γ is the interfacial tension and S, L and G stand for the solid, the liquid and the gas, respectively, see Figure 5 and Figure 6.

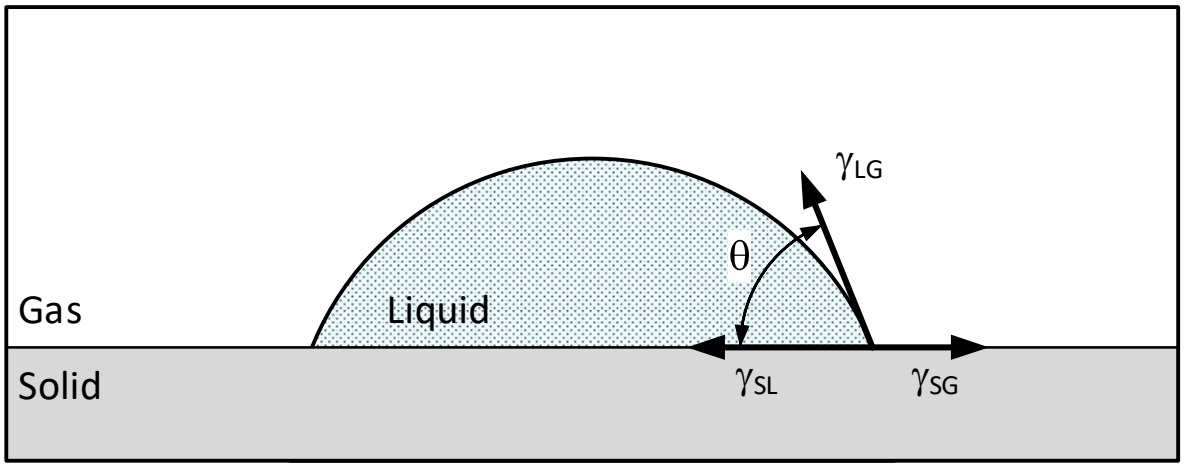

Figure 5. A liquid droplet on a solid surface and variables used in the Young equation.

The contact angle can take values between 0 and 180 degrees. The value 90 degrees separates wetting (less than 90 degrees) and non-wetting (more than 90 degrees) regimes. Complete

surface wetting is identified by the zero contact angle and completely non-wetting state is characterised by the contact angle 180 degrees.

The contact angle is related to the capillary pressure, which is the pressure difference across the interface which separates two fluids (Stefan Iglauer et al., 2014):

$$P_c = \Delta P = P_{nw} - P_w,$$

where Pnw and Pw are pressures of the non-wetting (carbon dioxide) and wetting (water) phases.

If a formation pore is modelled as a capillary tube, then it can be shown that the contact angle is connected to the capillary pressure through the Young-Laplace equation (Dake, 1978):

$$\Delta P = 2\gamma C,$$

where γ is the interfacial tension of the fluid pair, C is the mean curvature of the interface.

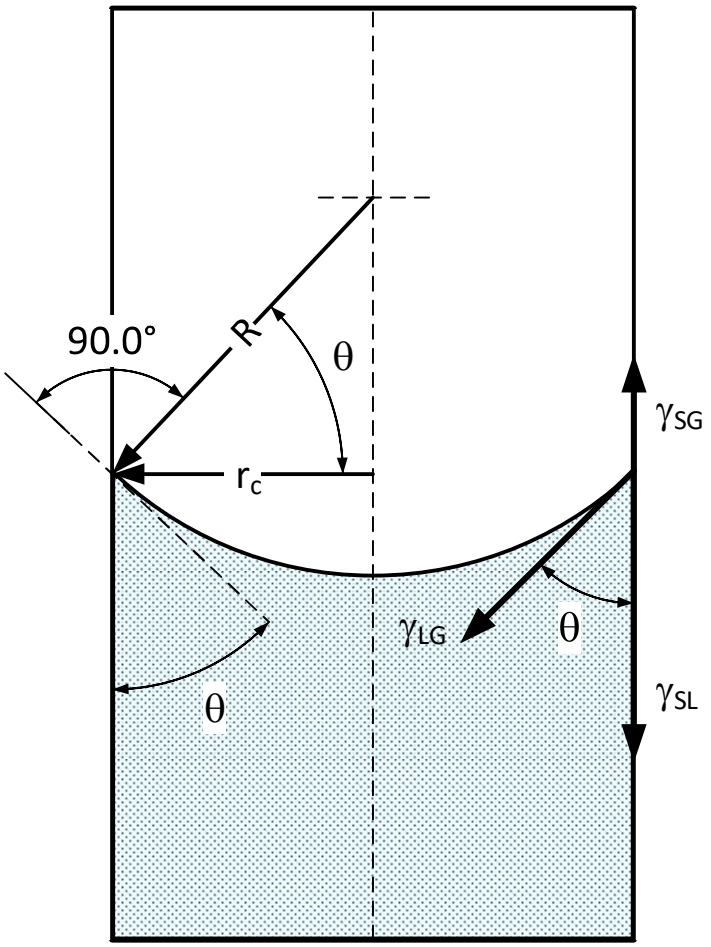

Figure 6. Capillary rise of a liquid illustrating parameters used in the Young-Laplace equation.

For a capillary tube shown in Figure 6:

$$P_c = 2\gamma/R,$$

$$R = r_c/cos\theta,$$

$$P_c = 2\gamma cos\theta/r_c,$$

where R is the principle radius of curvature, and r_c is the radius of the capillary tube (or pore radius).

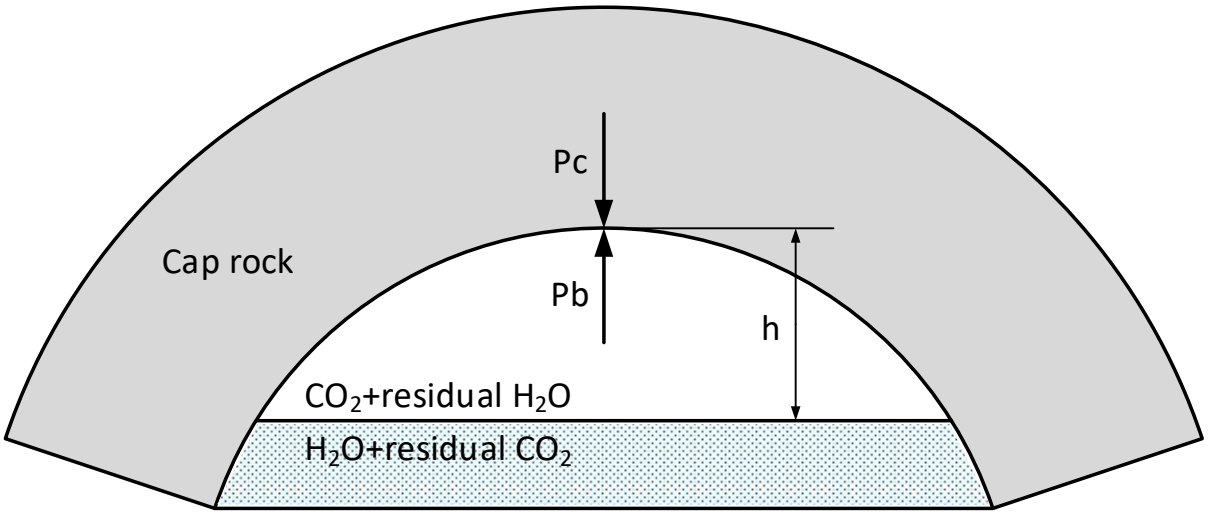

Figure 7. Schematic illustration of CO_2 structural trapping.

Capillary pressure which prevents non-wetting phase (carbon dioxide in the context of carbon capture and storage) from entering the pores is counterbalanced by the buoyancy of the non-wetting phase:

$$P_b = \Delta\rho gh,$$

where $\Delta\rho$ is the density difference between CO_2 and water, g is acceleration due to gravity, h is the height of the CO_2 plume, see Figure 7.

Equating Pc and Pb an estimation of the CO_2 storage capacity is obtained (Stefan Iglauer et al., 2014):

$$h = \frac{2\gamma cos\theta}{\Delta\rho g r_c}.$$

There are four variables in obtained equation: water-CO_2 interfacial tension, the contact angle, the density difference between CO_2 and water, and the radius of the capillary tube (the

pore radius). The latter one is the most difficult to estimate due to complex pore morphology of real rocks. Because of the same reason it is also less representative of real pore environments. On the other hand, the first two variables have extensively been studied in experimental and theoretical works. The third variable, the density difference, predominantly depends on properties of CO_2 which in turn strongly depend on pressure and temperature conditions.

2.4. Properties of carbon dioxide in geological conditions

At standard conditions of pressure and temperature CO_2 is a stable gas with the density 1.976 kg/m^3 (IPCC, 2005). Physical state of carbon dioxide varies with temperature and pressure according to its phase diagram, Figure 8 (www.chemicalogic.com). Three phases solid, liquid and gas coexist at -56.5°C and 5.18 bar. CO_2 becomes supercritical at 31.1°C and 73.9 bar. It is important to note that at supercritical conditions CO_2 fills available volume as a gas, but can have densities comparable with densities of its liquid state from 150 to more than 800 kg/m^3, depending on pressure and temperature, see Figure 9 (Bachu, 2003; IPCC, 2005).

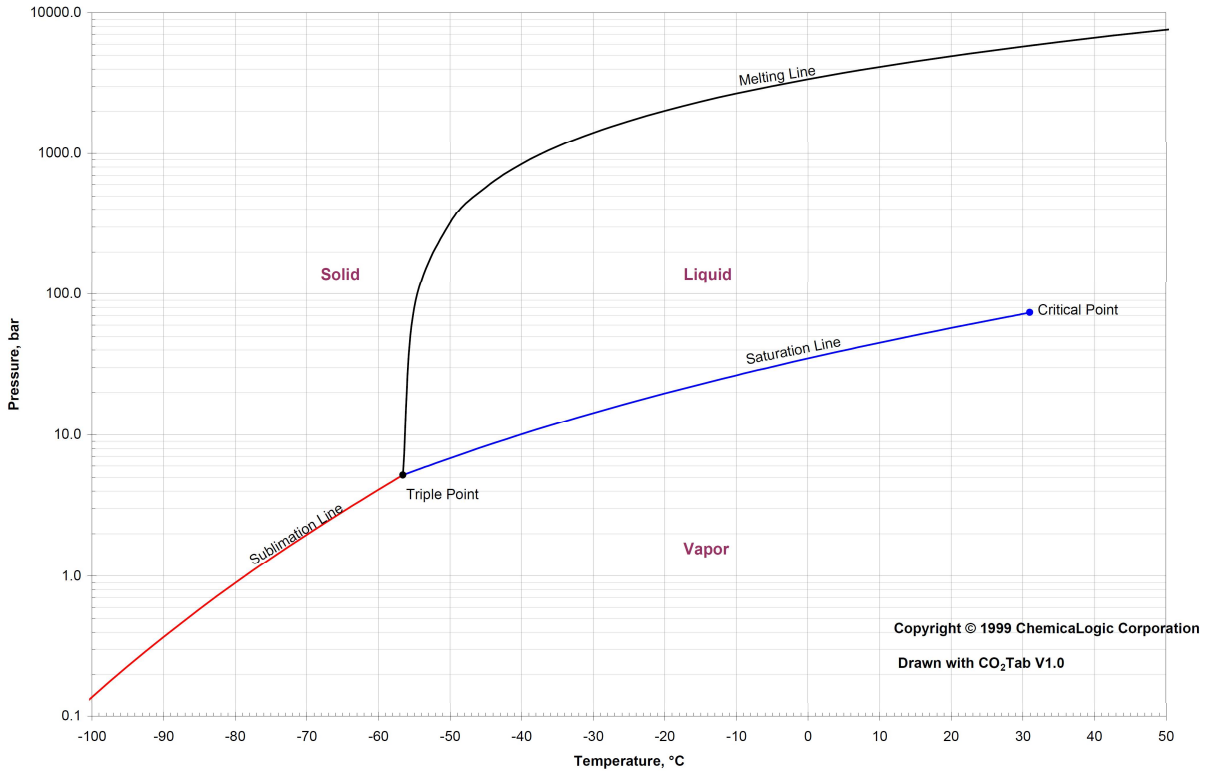

Figure 8. Phase diagram of carbon dioxide. Image source: ChemicaLogic Corporation, Copyright (c) 1999 ChemicaLogic Corporation, USA. All rights reserved.

Density of carbon dioxide is crucial for the storage efficiency and safety. Larger densities increase amount of stored CO_2 in terms of its mass and decrease its upward acting buoyancy force. As Figure 9 illustrates CO_2 density strongly linked to pressure and temperature and thus to depth at which it is stored. The greater the depth the greater the pressure and the greater the temperature, but their effect on CO_2 density is opposite. In the beginning CO_2 density increases rapidly with pressure, then temperature counteracts pressure which stabilises the density. Considering interplay of pressure and temperature with depth it was show that there exist an optimal depth range from 800 to 1000 m for "cold" geological basins and from 1500 to 2000 m for "warm" geological basins, where CO_2 density reaches plateau and almost ceases increasing or even decreases (Bachu, 2003). Expected storage pressure and temperature conditions and physical state of CO_2 at optimal depths can be determined from the hydrostatic and the geothermal gradients.

Variations of pressure P and temperature T with depth are given by formulae:

$$P = \rho_w g z,$$

$$T = T_s + Gz,$$

where ρ_w is water density, g is the acceleration due to gravity, z is the depth, Ts is the surface temperature, G is the geothermal gradient.

Eliminating the depth, the pressure and the temperature can be combined in one equation and superimposed onto CO_2 phase diagram (Bachu, 2003):

$$P = \frac{\rho_w g}{G}(T - T_s).$$

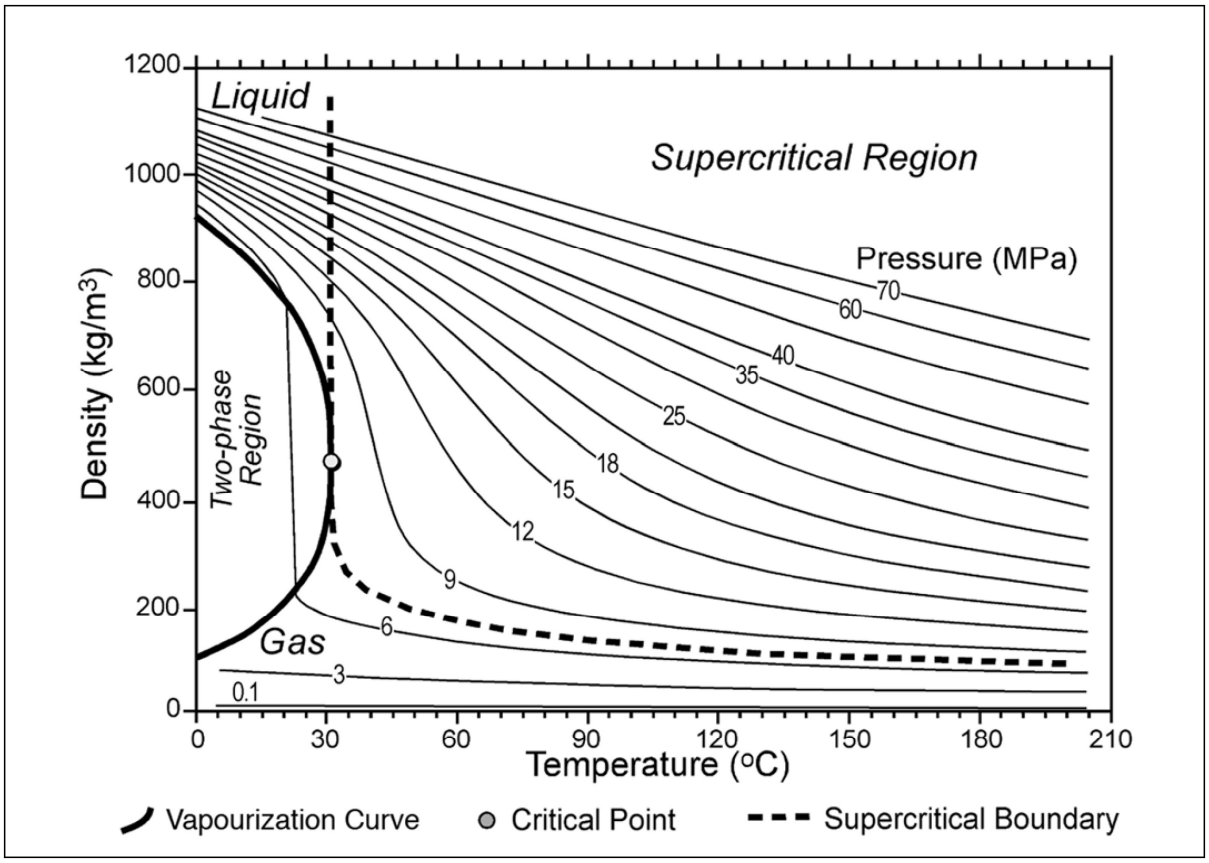

Figure 9. CO_2 density as a function of temperature and pressure. Image source: (Bachu, 2003; IPCC, 2005).

Overlay of geological conditions and physical states of CO_2 in coordinates pressure versus temperature is depicted in Figure 10. The "cold" and the "warm" basin conditions shown in Figure 10 are defined by the surface temperatures -2 and 30°C, respectively, and by the geothermal gradients 20 and 60°C/km, respectively (Bachu, 2003). The CO_2 saturation line is constructed with the Span and Wagner equation of state (Span & Wagner, 1996) using a web based tool (www.energy.psu.edu). The diagram in Figure 10 illustrates that if stored at the optimal depths, CO_2 could be either in supercritical or liquid states with pressures ranging from 7.85 to 19.62 MPa and temperatures covering interval from 14 to 150°C. In "cold" basins as depth increases from 800 to 1000 m CO_2 density decreases from 874 kg/m^3 (at 14°C and 7.85 MPa) to 868.2 kg/m^3 (at 18°C and 9.81 MPa), respectively. In "warm" basins as depth increases from 1500 to 2000 m CO_2 density increases from 273.5 kg/m^3 (at 120°C and 14.7 MPa) to 320 kg/m^3 (at 150°C and 19.62 MPa), respectively.

Figure 10 also depicts one (out of many) possible "critical path", the path in the pressure-temperature space which crosses the critical point when CO_2 moves upwards from the storage formation. Apart from this unique route characteristic phase transformations in warmer

conditions are from the supercritical state to the gas state and in the colder conditions from the liquid state to the gas state (with uptake of the latent heat). In colder conditions more general metamorphoses from the supercritical to the liquid and then to the gas states are possible as well.

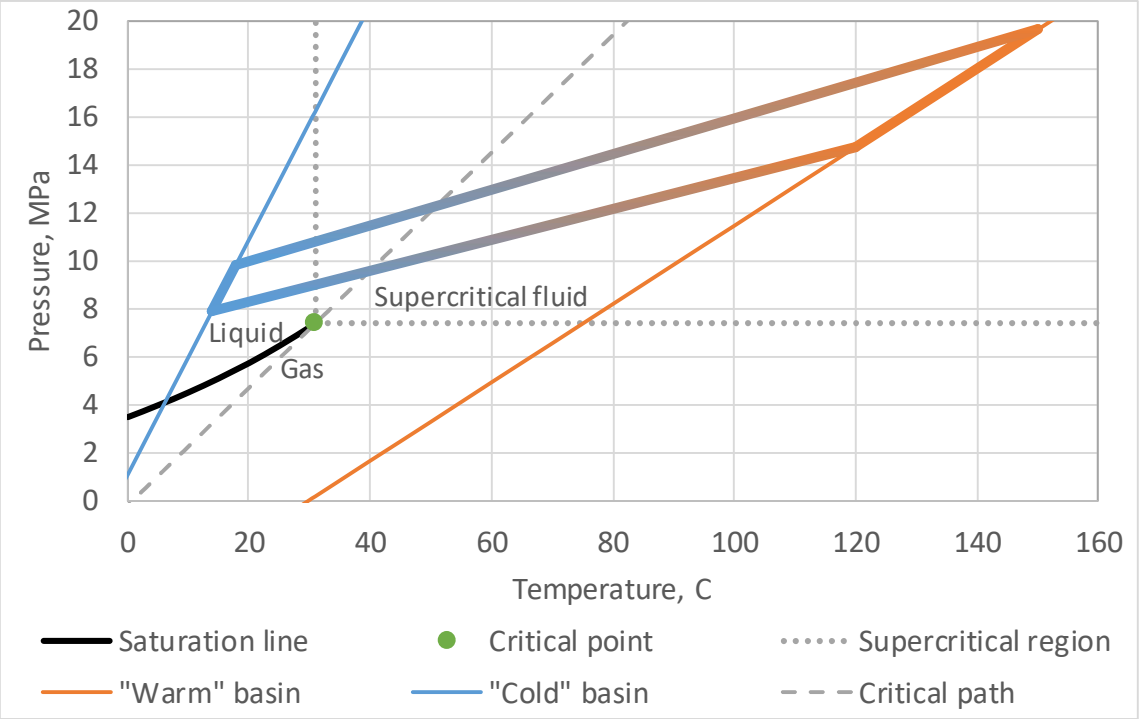

Figure 10. Possible geological pressure and temperature conditions in "cold" and "warm" basins worldwide superimposed onto carbon dioxide phase diagram. Thickened lines highlight conditions at optimal depths 800-1000 m for "cold" and 1500-2000 m for "warm" basins, respectively. Interpolation between optimal "cold" and "warm" conditions (gradient coloured lines) shows range of pressures and temperatures expected at CO_2 storage depths. Image is constructed on basis of (Bachu, 2003).

2.5. Quartz wettability in presence of carbon dioxide

Quartz is the second most abundant mineral in the Earth's continental crust (about 12% by weight) (Anderson & Anderson, 2010; Marshall & Fairbridge, 1999), it is behind feldspars which compose about half of the crust. In addition to its global natural abundance quartz is present in large concentrations in cap rocks, more than 50% by weight (Stefan Iglauer, Al-Yaseri, Rezaee, & Lebedev, 2015). Quartz wettability is therefore crucial for characterisation of overall wettability of real multi-mineral cap rocks. To understand and quantify wettability of quartz surface it has extensively been studied not only in numerous experiments but also with advanced methods of theoretical chemistry and materials science.

2.5.1. Experimental studies

Experimental wettability studies explored different gaseous atmospheres including air (Mazurek, Pogorzelski, & Boniewicz-Szmyt, 2009; Roshan, Al-Yaseri, Sarmadivaleh, & Iglauer, 2016), water vapour saturated air (Lamb & Furlong, 1982), hydrogen sulphide and carbon dioxide (Broseta, Tonnet, & Shah, 2012; Espinoza & Santamarina, 2010). Variety of water solutions have been tested ranging from distilled water (Sklodowska & Matlakowska, 1997) to brines of different salinity (Ahmed Z. Al-Yaseri, Lebedev, Barifcani, & Iglauer, 2016; Ahmed Zarzor Al-Yaseri, Roshan, Lebedev, Barifcani, & Iglauer, 2016; Broseta et al., 2012). Diversity of combinations surface-liquid-gas examined in the experiments is enriched by multiplicity of contact angle measurement methods. The are many approaches to measure the contact angle experimentally which are described in specialized textbooks, for example, Chapter 1 "Contact Angle and Wetting Properties" in (Bracco & Holst, 2013) offers nine methodologies for assessing the contact angle experimentally. Some common techniques to measure the contact angle relatively widely seen in research literature are: the sessile drop method (Sarmadivaleh, Al-Yaseri, & Iglauer, 2015), the captive bubble method (Kaveh, Rudolph, van Hemert, Rossen, & Wolf, 2014; Saraji, Goual, Piri, & Plancher, 2013), the capillary rise method (Koh, Hao, Smith, Chau, & Bruckard, 2009) and the direct measurement with the atomic force microscopy (Deng, Xu, Lu, Wang, & Shi, 2018).

In the sessile drop method, a water droplet is placed on the surface of a mineral in atmosphere of the less dense phase, i.e. air, CO_2 or other gases. The captive bubble method is an analogous approach where the less dense phase is injected underneath the surface of a mineral submerged into denser phase, i.e. water. In the capillary rise method, the contact angle is calculated using the values of experimentally measured capillary rise and radius (Bracco & Holst, 2013). In contrast to other methods, where droplet sizes are in the range of millimetres, the atomic force microscopy is used to measure the contact angle of micrometre-sized droplets. In the technique, the force between the sharp tip and a surface as a function of their separation is detected and used to reproduce the shape of the sample. Very high resolution of less than nanometre is attainable with the atomic force microscopy (Bracco & Holst, 2013).

At the micrometre level of the atomic force microscopy, size of the water droplet (or bubble, in a more general case) has negligible effect on the contact angle measured in air atmosphere (Deng et al., 2018). For larger droplets, however, size matters and affects outcome of

measurements. The gravitational influence becomes significant when radius of the droplet exceeds the threshold value given by the capillary length. This threshold condition is fulfilled when the gravitational forces become comparable with the surface tension forces. Relative importance of one type of forces over the other is formally expressed by a dimensionless number, the Bond number (also known as the Eötvös number) (Hager, 2012):

$$B_O = \frac{\Delta\rho g r^2}{\gamma},$$

where $\Delta\rho$ is the density difference between the liquid and vapour phases, g is acceleration due to gravity, r is the droplet radius, γ is the interfacial tension of the fluid pair.

The droplet size therefore becomes an important parameter affecting measurements of the contact angle when:

$$B_O \geq 1.$$

Experimental assessments of the contact angle for all droplet sizes are influenced by the surface roughness and heterogeneity (Drelich, Miller, & Good, 1996). It was demonstrated in (Deng et al., 2018) that even for a micrometre sized water droplet the contact angles measured along the triple-phase contact line may have almost twofold difference, ranging from 27.8° to 48.9°. To quantify effects of surface's roughness and heterogeneity on the contact angle and to link contact angles obtained for ideal smooth and homogeneous surfaces with real contact angles on rough and heterogeneous surfaces two models have been developed (Cassie & Baxter, 1944; Wenzel, 1936). Effect of surface roughness on the contact angle is expressed by an equation proposed by Robert Wenzel (Wenzel, 1936):

$$cos\theta_W = R_f cos\theta,$$

where θ_W and θ are the Wenzel contact angle and the contact angle obtained on the smooth and homogeneous surface, respectively; R_f is the roughness factor which is defined as the ratio of the area of the rough surface to the area of projected flat surface (in practice the roughness factor is always larger than one).

Wenzel's theory assumes that the roughness grooves are completely filled with liquid for which the contact angle is measured, the assumption which is not required for the Cassie-Baxter model (Cassie & Baxter, 1944):

$$cos\theta_{CB} = f_1 cos\theta_1 + f_2 cos\theta_2,$$

where θ_{CB} is the Cassie-Baxter contact angle; f_1 and f_2 are the area fractions for surface components 1 and 2, for which the contact angles are θ_1 and θ_2, respectively (in principle, the model can be extended to any number of surface components).

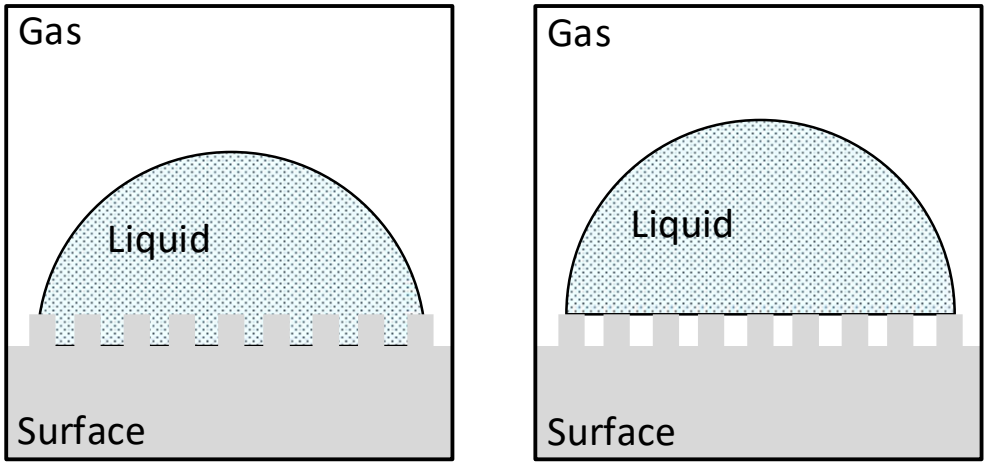

Figure 11. Liquid droplet on a rough and inhomogeneous surface. The Wenzel (left) and the Cassie-Baxter (right) models.

The Cassie-Baxter model can handle situations where the roughness grooves are filled with a gas (Figure 11), which becomes one of the surface components, let us say the second one. In a water-air system this means that θ_2=180°, and with f_2=1-f_1 one arrives at:

$$cos\theta_{CB} = f_1(cos\theta_1 + 1) - 1.$$

It is interesting to note that for a given surface material the contact angle can be tuned if necessary just by altering f_1. In the context of CO_2 storage, just because of surface roughness and the Cassie-Baxter wetting regime, the contact angles of water may be heightened and CO_2 storage capacity and security may be reduced.

As may be inferred from presented in this section material the contact angle is a sensitive to number of parameters characteristic. Among those parameters are surface chemistry (hydrophilicity and hydrophobicity (Stefan Iglauer, 2017)) and surface conditions (roughness and homogeneity, pre-treatment and crystal face (Deng et al., 2018)), size of the droplet (or bubble), method used to measure the contact angle (Drelich et al., 1996). In addition, in the context of carbon geo-sequestration, attention should be paid to salinity of the denser phase and ionic strength of the solution, experimental atmosphere including type of gas and its

pressure and temperature. Increase in salinity, valency of dissolved ions, and in carbon dioxide pressure causes increase in CO_2-wettability, while effect of temperature is less clear (Stefan Iglauer, 2017). Understanding of influence of these latter four factors (pressure and temperature, salinity, type of ions) on water/CO_2 wetting behaviour of quartz is crucial for correct estimation of CO_2 storage capacity and security of existing and prospective carbon geo-sequestration projects.

An attempt (Roshan et al., 2016) to understand effects of pressure and temperature on the contact angle was made using an analytical expression derived in (Garcia, Osborne, & Subashi, 2008, 2009):

$$cos\theta = -1 - \frac{\Delta\rho}{\gamma}\int_{z_{min}}^{\infty} V_s(z)dz,$$

where $\Delta\rho$ is the density difference between the liquid and vapour phases, γ is the interfacial tension of the fluid pair, V_s is the potential energy of the adsorbate molecule due to the substrate (the substrate potential), z_{min} is the position of the minimum of the potential near the surface.

Because of high CO_2 compressibility there is one strongly dominating factor affecting the contact angle with varying pressure - carbon dioxide density, which upon increase enhances CO_2-mineral interactions (Stefan Iglauer, 2017). In terms of presented equation, the effect of pressure may be understood as follows. With increase in pressure the density difference between the liquid (water) and vapour (CO_2) phases decreases, see Figure 9. It was shown that the ratio of the van der Waals potential integral over the interfacial tension for given temperature, brine composition and mineral substrate is constant (Ahmed Zarzor Al-Yaseri et al., 2016). Reduced due to increased pressure density difference in the second term on the right hand side of the equation is thus the main factor responsible for increase of the contact angle.

For the sake of completeness effect of pressure on the interfacial tension should be characterised too. Pressure increase from ambient conditions causes rapid decrease in water-CO_2 interfacial tension from about 70 to 30 mN/m at temperatures ranging from 278 to 333 K (Hebach et al., 2002), after pressure reaches the saturation or supercritical values the interfacial tension remains almost unchangeable (Hebach et al., 2002). It is necessary to note

that in relative terms the effect of pressure on water-CO_2 interfacial tension is much smaller than its effect on CO_2 density, Figure 9.

With variations in temperature there is no sole dominating factor, the density difference and the interfacial tension of the fluid pair are both affected; as well as the kinetic energy of the adsorbate molecules, which in turn results in variations in explored by the adsorbate molecules energies of the potential well. That is why the effect of temperature on the contact angle is more intricate. For example, the contact angle decreases with increase in temperature for coal and increases with increase in temperature for quartz (Stefan Iglauer, 2017). Qualitative picture of the advancing contact angle dependence on pressure and temperature of a deionized water droplet on quartz surface cleaned with air plasma in carbon dioxide atmosphere is shown in Figure 12.

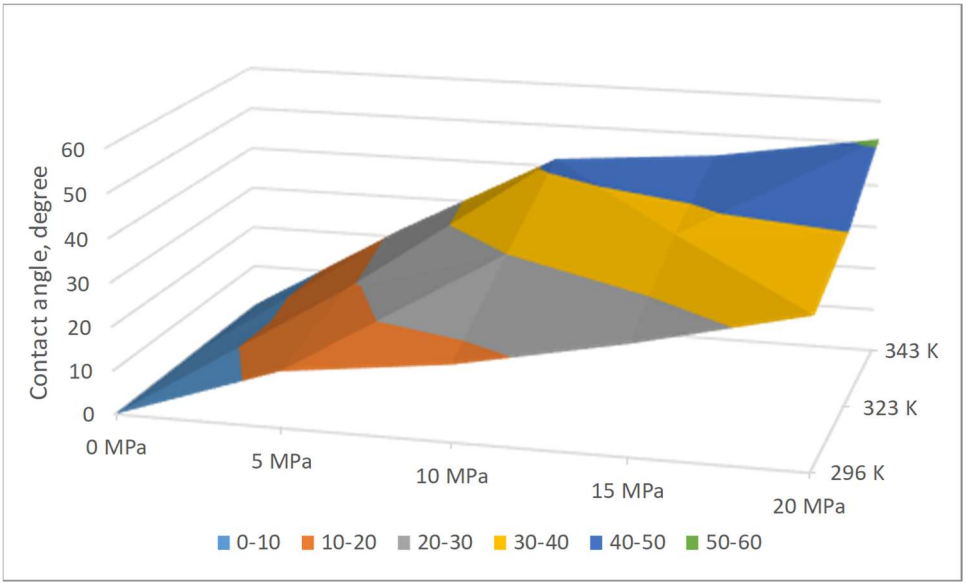

Figure 12. Advancing contact angle of a deionized water droplet on rough quartz surface (RMS 560 nm) cleaned with air plasma in carbon dioxide atmosphere at different conditions of pressure (in MPa) and temperature (in Kelvin). Source of data: (Ahmed Z. Al-Yaseri et al., 2016).

It is clear from Figure 12 that increase in temperature and pressure has the same qualitative effect on the contact angle of a water droplet on quartz surface in CO_2 atmosphere, both parameters increase the contact angle. It is also clear that at the geological sequestration conditions the contact angle is high, up to 50°, and the quartz surface is only weakly water-wet (Ahmed Z. Al-Yaseri et al., 2016).

Experimentally measured advancing contact angles θa should be expected to be a good approximation of the static contact angles defined by the Young's equation (Bracco & Holst,

2013). In general, the wetting phenomena is dynamic, the contact angles formed by expanding liquid are called "advancing" - θa, and the contact angles formed by contracting liquid are called "receding" - θr. The difference between the advancing and the receding angles originates from surface roughness and heterogeneity and is referred to as the contact angle hysteresis:

$$H = \theta_a - \theta_r.$$

After the PT-conditions, water salinity and type of dissolved ions are known to significantly affect quartz wettability in CO_2 atmosphere, Figure 13. The effect of salinity is explained by screening of surface charges by salt ions of opposite charge which from double layer reducing surface electrostatic potential and thus reducing overall surface polarity and hydrophilicity (Stefan Iglauer, 2017). The higher the salt concentration the higher the contact angel. The effect increases with higher valency (i.e. higher charge concentration per unit of volume) and with higher ionic strength:

$$I = \frac{1}{2}\sum_{i=1}^{n} c_i z_i^2,$$

where n is the number of types of ions in the solution, c_i is the molar concentration of ion i (mol/L), z_i is the charge of ion i.

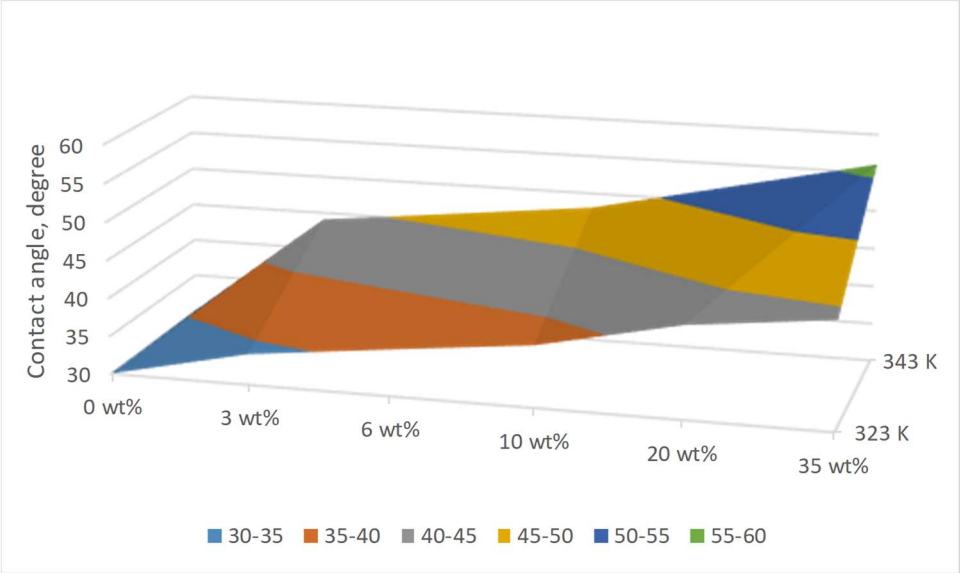

Figure 13. Advancing contact angle of a water droplet on rough quartz surface (RMS 560 nm) cleaned with air plasma with varying concentration of NaCl (in wt%) at 10 MPa of carbon dioxide pressure at two temperatures (in Kelvin). Source of data: (Ahmed Z. Al-Yaseri et al., 2016).

To facilitate understanding of natural phenomena and ensure reproducibility of the results idealized conditions are used in laboratories in which only few parameters are varied. Often clean mineral and quartz surfaces are prepared in strongly oxidizing solutions. On the other hand, in practical realizations of the carbon capture and storage technology mineral surfaces are far from ideal. Coal beds and depleted oil or gas reservoirs are considered as possible storage medium for carbon dioxide. Within these formations mineral surfaces aged in oil, alkylated surfaces with chemisorpt hydrocarbons, and composed of organic matter coal are interfaces encountered by stored CO_2. Experimental studies indicate that in these structures surfaces of minerals are in the best case intermediate wet and can be strongly CO_2-wet (Ali et al., 2019; Arif, Barifcani, Lebedev, & Iglauer, 2016; Stefan Iglauer et al., 2014).

2.5.2. Theoretical studies

There are number of works employing computational methods to simulate wetting behaviour of water on surfaces of minerals including quartz, in particular in presence of carbon dioxide and often in the context of the carbon geo-sequestration (Bagherzadeh, Englezos, Alavi, & Ripmeester, 2012; C. Chen, Chai, Shen, & Li, 2018; C. Chen, Chai, Shen, Li, & Song, 2017; C. Chen, Wan, Li, & Song, 2015; C. Chen, Zhang, Li, & Song, 2015; Giovambattista, Debenedetti, & Rossky, 2007; S. Iglauer, Mathew, & Bresme, 2012; Javanbakht, Sedghi, Welch, & Goual, 2015; Liang, Tsuji, Jia, Tsuji, & Matsuoka, 2017; Liu, Yang, & Qin, 2010; McCaughan, Iglauer, & Bresme, 2013; Tenney & Cygan, 2014; Tsuji, Liang, Kunieda, Takahashi, & Matsuoka, 2013). These studies, among other aims, complement the experimental results especially in situations when quantification of the contact angle is hampered by parameters which are difficult or even impossible to control precisely because of side chemical reactions or contaminations. In case of quartz, the surface chemistry (hydrophilicity and hydrophobicity) is one of such parameters. This factor is the first in terms of importance for characterisation of the contact angle, followed by pressure, temperature, salinity and salt type (Stefan Iglauer, 2017). Yet, the very exact structure of the surface of silica polymorphs remains unknown even in 2018 (Eder et al., 2015; Feya et al., 2018). Theoretical studies explored possible surface structures and identified contact angles on pristine (S. Iglauer et al., 2012) and hydroxylated (C. Chen, Wan, et al., 2015) surfaces, as well as the dependence of the contact angle on the degree of hydroxylation (C. Chen, Zhang, et al., 2015). Effect of CO_2 contamination with CH_4,

Ar and H_2S on the water-CO_2 interfacial tension and on the contact angle of a water droplet in CO_2 atmosphere on a silica surface was studied in (C. Chen et al., 2018).

Number of quartz polymorphs and crystal faces have been studied in the context of CO_2 sequestration and storage, although, in general, α-quartz is the crystal phase thermodynamically stable at reasonable geological conditions (Swamy, Saxena, Sundman, & Zhang, 1994), and the (001) surface of α-quartz is regarded as the most stable surface of pristine (de Leeuw, Higgins, & Parker, 1999) and hydroxylated α-quartz (Murashov, 2005; Yang & Wang, 2006). The pristine surface of α-quartz was used in (S. Iglauer et al., 2012). In this computational work of professor Bresme the (001) surface was reconstructed. In studies reported in (C. Chen et al., 2018; C. Chen, Wan, et al., 2015; C. Chen, Zhang, et al., 2015) previously developed force field and a surface model database for silica (Emami et al., 2014) were used. In the latter work the surface models were derived from the $(10\overline{1})$ plane of α-cristobalite, which is stable above 1470°C and metastable at lower temperatures, and from the (100) plane of α-quartz. In a work (C. Chen et al., 2017) the $(2\overline{0}2)$ plane of α-cristobalite was used to study how ion type and salinity affect wettability of quartz in presence of CO_2.

Although variability of measured and calculated contact angles is high (Stefan Iglauer et al., 2014), theoretical results in general show reasonable qualitative agreement with experimental studies (Stefan Iglauer, 2017); deviations from the agreement can be explained by experimental atmosphere, measuring technique, droplet size, surface pre-treatment, surface heterogeneity and roughness (Deng et al., 2018). If conditions of experiments and theoretical investigations are carefully matched, quantitative agreement can be demonstrated, e.g. the contact angle of a water droplet on hydroxylated quartz surface at 318 K at 10 MPa CO_2 pressure was calculated to be 22.6° using classical molecular dynamics simulations, and experimental measurements amounted to 20-21° (C. Chen, Wan, et al., 2015).

Modelling approaches and used approximations are of paramount importance in simulations of interfacial phenomena. Reported in literature results indicate that for the hydroxylated quartz surface fixation of hydroxyl groups, or perhaps even the whole surface, may be an oversimplification. The contact angle of a water droplet on quartz surface in CO_2 atmosphere at temperature 318 K was found to be 22.5° in works (C. Chen et al., 2017; C. Chen, Wan, et

al., 2015) (actual stated contact angle values are 22.6 and 22.4° for 2015 and 2017 papers, respectively). In (C. Chen, Wan, et al., 2015) CO_2 pressure was 10 MPa and concentration of silanol groups was 9.4 per nm^2, fixed quartz surface was used. In (C. Chen et al., 2017) CO_2 pressure was 20 MPa and concentration of silanol groups was 4.7 per nm^2, atoms of hydroxyl groups were not fixed. Doubling of CO_2 pressure and two-fold reduction in concentration of OH groups must lead to significant increase in the contact angle, but it stayed the same. It must be added that in (C. Chen, Wan, et al., 2015) the crystal surface was taken from the surface model database for silica (Emami et al., 2014), where it was derived from the (100) plane of α-quartz. In (C. Chen et al., 2017) the $(2\bar{0}2)$ plane of α-cristobalite was used. Although the crystal phase and the surface index are important, the primary factor (for relaxed and coordinated surfaces) which influences the contact angle is the surface chemistry (hydrophilicity and hydrophobicity), which in case of hydroxylated quartz is mostly defined by concentration and (artificially limited) mobility of silanol groups, as demonstrated by the given comparison of two studies.

2.6. Quartz crystal

Crystalline silica (SiO_2) has many polymorphs, some of them are α-quartz, β-quartz, α-cristobalite, β-cristobalite, coesite and stishovite (Demuth, Jeanvoine, Hafner, & Ángyán, 1999). Structures and properties of these polymorphs are known and understood. Low temperature polymorphs, such as α-quartz, exist at ambient conditions (Swamy et al., 1994). Upon heating at normal pressure α-quartz transforms into β-quartz at 573°C, see Figure 14. The transition temperature sharply increases with pressure. Above approximately 3 GPa and 1200°C α-quartz becomes unstable and with increase in pressure transforms to coesite, and with increase in temperature transforms to β-quartz. This range of pressures and temperatures covers geological carbon geo-sequestration conditions, where α-quartz is thermodynamically favourable polymorph.

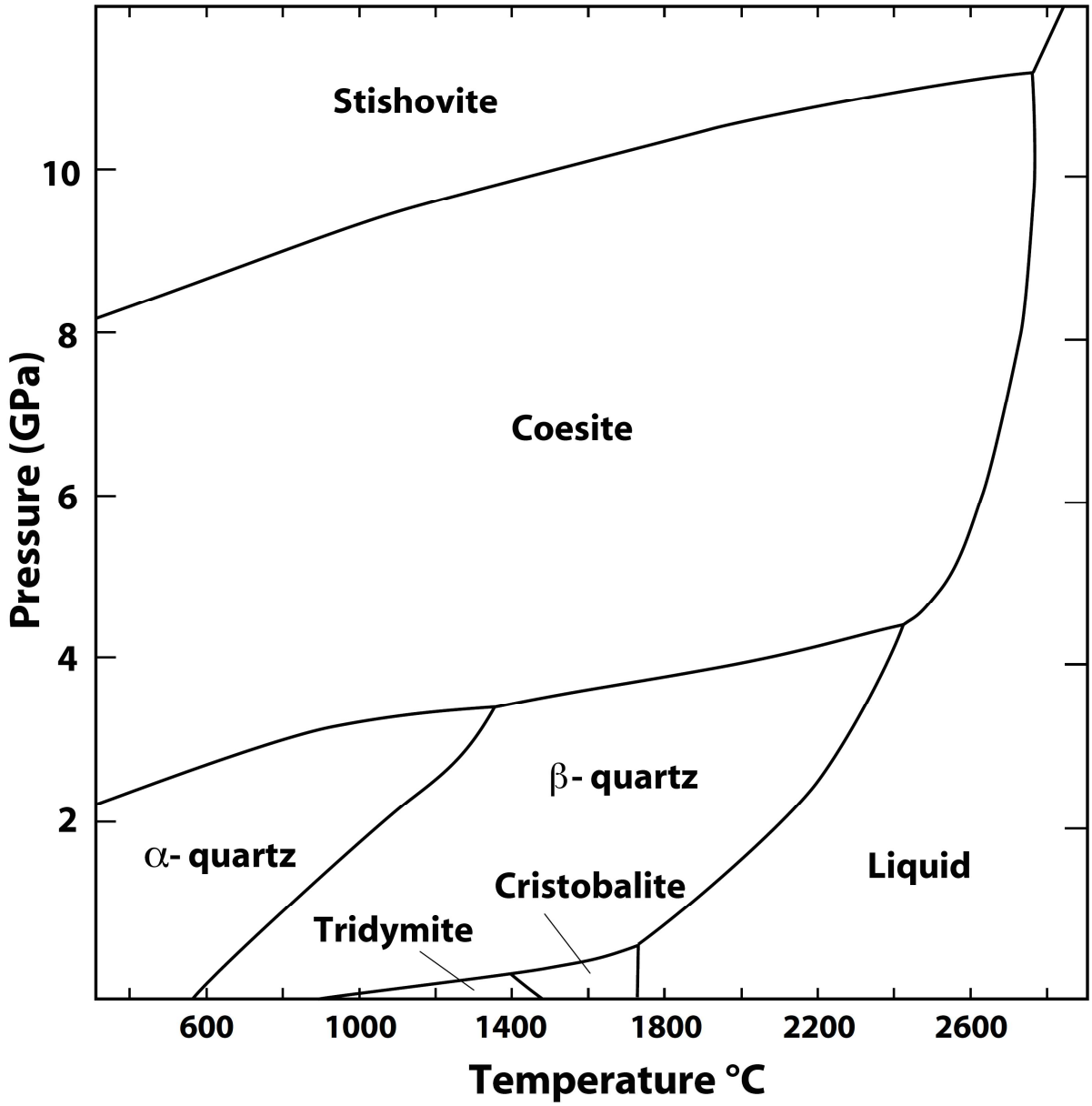

Figure 14. Approximate phase diagram of silica. Image source: (serc.carleton.edu), drawn by Dexter Perkins and John Brady on basis of (Swamy et al., 1994).

The primitive hexagonal unit cell of α-quartz (Levien, Prewitt, & Weidner, 1980) contains 3 silicon and 6 oxygen atoms, Figure 15. Crystallographic vectors and angles of the primitive cell are: a=4.916 A, b=4.916 A, c=5.4054 A, α=90°, β=90°, γ=120°. The crystal can have two enantiomorphically related (chiral) space groups $P3_121$ and $P3_221$ (Adeagbo, Doltsinis, Klevakina, & Renner, 2008). Both space groups belong to the hexagonal crystal family and the trigonal crystal system which is characterised by the three-fold rotational symmetry.

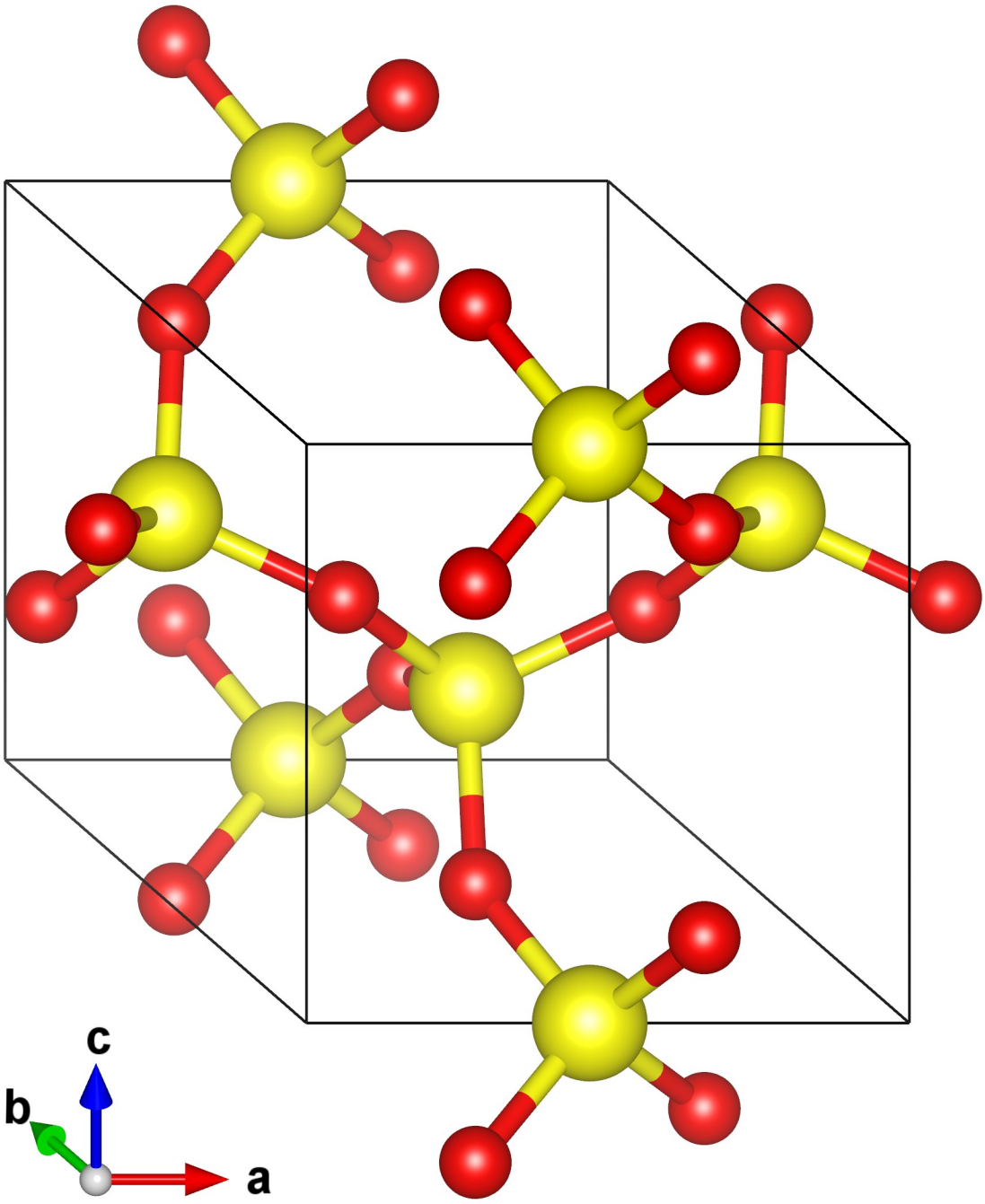

Figure 15. The primitive unit cell of α-quartz. Yellow balls are silicon atoms; red balls are oxygen atoms.

2.7. Quartz surface

Importance of quartz and properties of its surface were emphasized by many authors because of several reasons among which are the following: catalytic role of dust grains in astrochemistry, biotoxicity related to undercoordinated silicon and oxygen atoms (Goumans, Wander, Brown, & Catlow, 2007), applications of quartz in construction industry and in piezoelectric devices (Malyi, Kulish, & Persson, 2014), abundance of the mineral in Earth's

crust (de Leeuw et al., 1999; Yang & Wang, 2006). Number of works are dedicated to properties and prediction of quartz surface structure using methods of computational chemistry and materials science (Y.-W. Chen, Cao, & Cheng, 2008; de Leeuw et al., 1999; Eder et al., 2015; Feya et al., 2018; Goumans et al., 2007; Malyi et al., 2014; Murashov, 2005; Yang & Wang, 2006). This effort of theoretical groups is a response to a lack of complete understanding of detailed surface structure from the experimental view point (Goumans et al., 2007; Malyi et al., 2014). The situation with quartz surface structures is well expressed by a quotation taken from (Eder et al., 2015): *"Despite the many application areas, the atomic surface structures of silica polymorphs are neither well understood nor well characterised"*.

According to contemporary models of α-quartz (001) surfaces there are by and large two extreme types of ideal structures: (i) the pristine (no hydroxyl groups, stable Si-O-Si bridges) and (ii) the fully hydroxylated. The ideal fully hydroxylated theoretical silica surface is covered with geminal silanol groups, which gives concentration of OH groups (or single silanol groups) about 9.4 per nm^2 (Emami et al., 2014) (slightly depends on calculated lattice parameters). Any real hydroxylated silica surface (excluding possible contaminations and defects) is a combination of isolated silanols, vicinal silanols, geminal silanols and Si-O-Si bridges. Average concentration of OH groups (or single silanol groups) on real hydroxylated surfaces under ambient conditions is 4.5-6.2 per nm^2 (Iler, 1979). This silanol density agrees well with relatively recent comprehensive review paper where average concentration of OH groups is said to be a physicochemical constant of 4.6 or 4.9 groups per nm^2, depending on averaging technique, the least square or the arithmetical mean, respectively (Zhuravlev, 2000).

Top view of fully hydroxylated (001) quartz surface is shown in Figure 16, side views are shown in Figure 17. This surface structure is reconstructed in number of theoretical studies (Goumans et al., 2007; Murashov, 2005; Yang & Wang, 2006). Zigzag hydrogen bonded network with short and long hydrogen bonds was noticed and explicitly discussed in (Goumans et al., 2007; Yang & Wang, 2006). Reported short and long distances of hydrogen bonds are 1.74 A and 2.11 A in (Yang & Wang, 2006) and 1.81 A and 2.34 A in (Goumans et al., 2007). The PBE functional (Perdew, Burke, & Ernzerhof, 1996) and parameters of the calculations used in (Goumans et al., 2007) resulted in slightly upward orientation of the hydrogen atoms forming the long hydrogen bonds, which agrees with (Murashov, 2005), where the PW91 functional (Perdew et al., 1992; Y. Wang & Perdew, 1991) was used and the author did not discuss the

long hydrogen bonds. In work (Yang & Wang, 2006) authors also used the PW91 functional (Perdew et al., 1992; Y. Wang & Perdew, 1991) and reported almost parallel to the surface orientation of OH groups. Overall, all three reported structures are in reasonable agreement with each other with tolerable differences in bond lengths and angles.

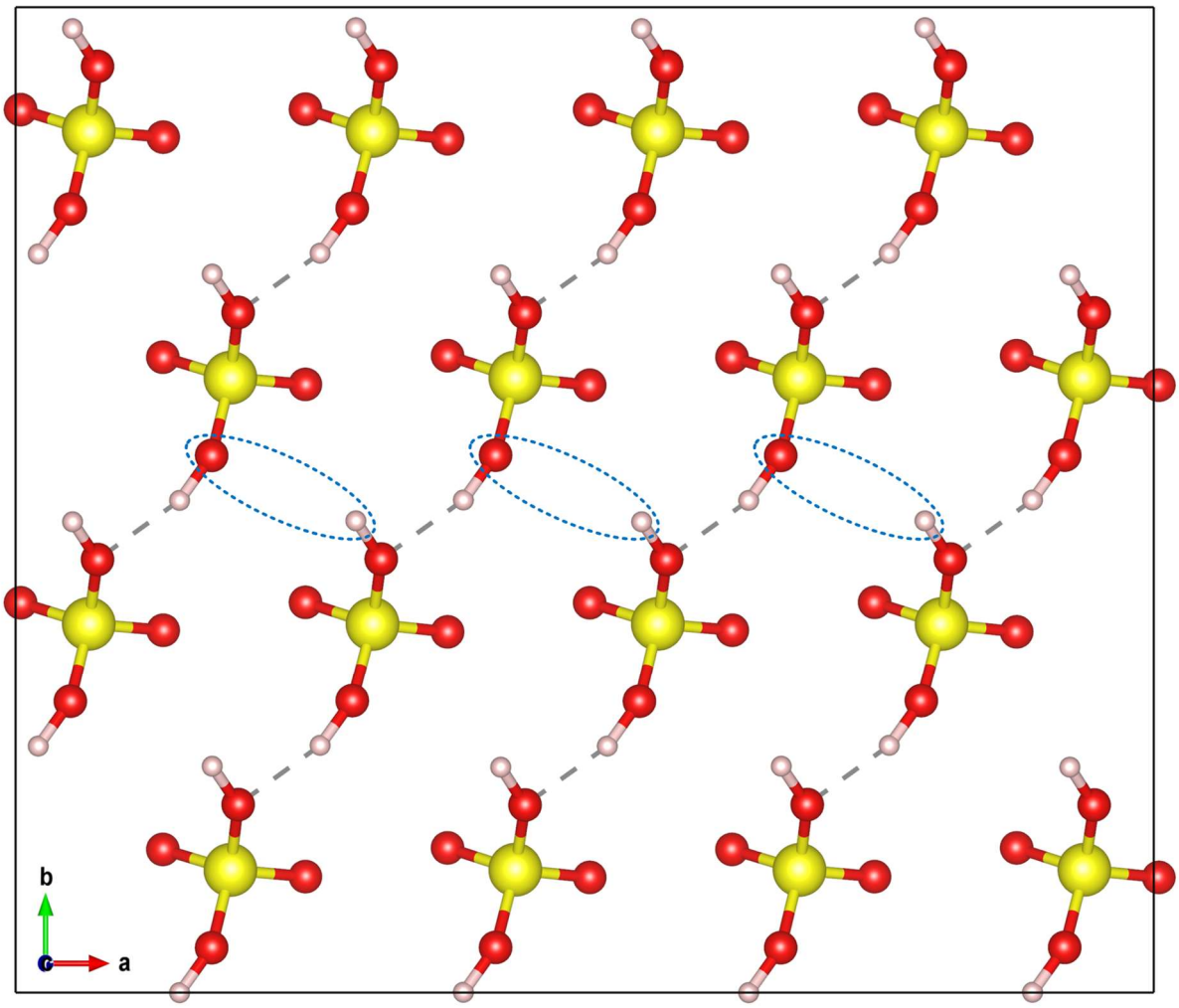

Figure 16. Top view of hydroxylated (001) quartz surface. Only top SiO_4H_2 groups are shown. Yellow balls are silicon atoms, red balls are oxygen atoms, white balls are hydrogen atoms. Short (strong) hydrogen bonds are shown with straight dashed lines. To highlight the zigzag structure of alternating strong and weak hydrogen bonds three long (weak) hydrogen bonds are shown with dashed blue ellipses along a horizontal line.

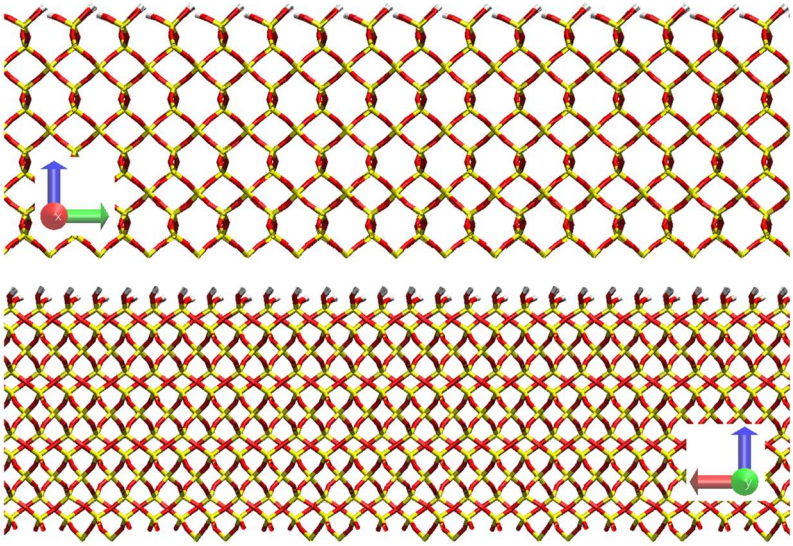

Figure 17. Side views (top: along x direction; bottom: along y direction) of a four-layer slab (four heights of the primitive quartz unit cell) of hydroxylated quartz. Atoms are shown with bonds, yellow - silicon atoms, red - oxygen atoms, white - hydrogen atoms.

Pristine quartz surface was modelled and reconstructed in (Y.-W. Chen et al., 2008; de Leeuw et al., 1999; Eder et al., 2015; Feya et al., 2018; Malyi et al., 2014). According to available information the pristine surface has two very close in energy structures the 6-member triangle-like rings and the 6-member ellipse-like rings. To the best of our knowledge the latter and the most stable structure was predicted in (Y.-W. Chen et al., 2008). It was then studied in (Eder et al., 2015; Feya et al., 2018; Malyi et al., 2014), with experimental confirmation reported in (Eder et al., 2015). The most stable 6-member ellipse-like rings (001) pristine quartz surface is shown in Figure 18, side views of this surface are shown in Figure 19.

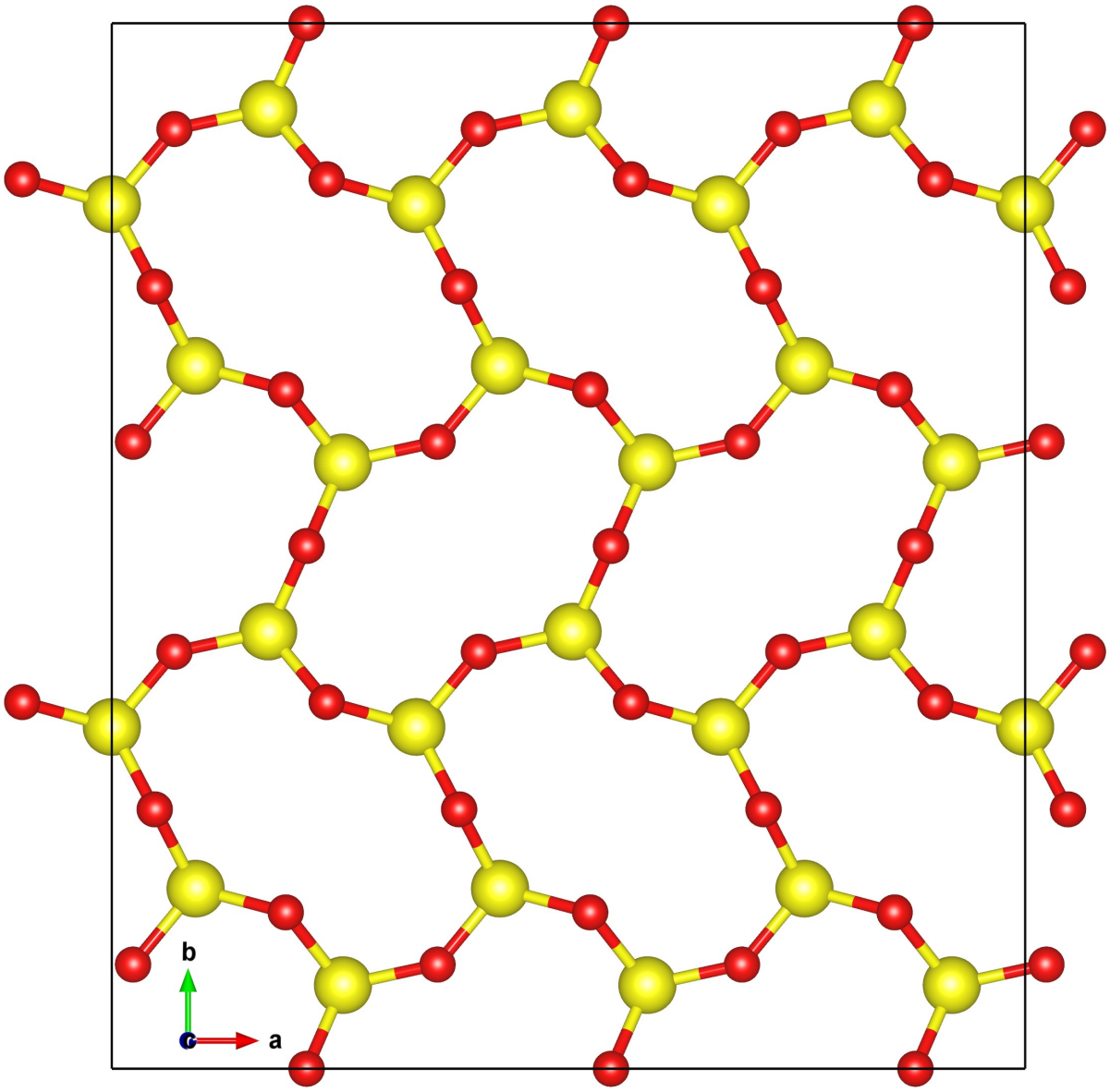

Figure 18. Top view of pristine (001) quartz surface. Only top layer atoms are shown. Yellow balls are silicon atoms and red balls are oxygen atoms.

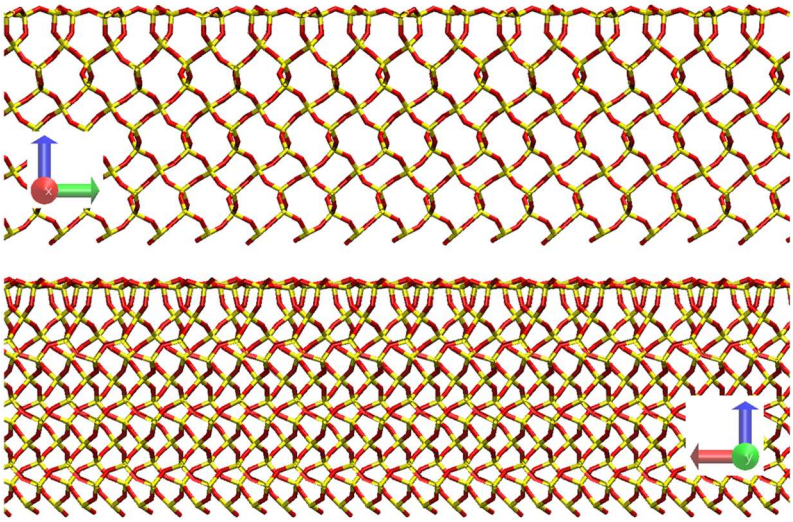

Figure 19 Side views (top: along x direction; bottom: along y direction) of a four-layer slab (four heights of the primitive quartz unit cell) of pristine quartz. Atoms are shown with bonds, yellow - silicon atoms, red - oxygen atoms.

2.8. Conclusions

Carbon dioxide capture and storage was proposed as a technologically and economically feasible solution to reduce carbon dioxide content in earth's atmosphere and thus avert global warming. To ensure secure long term underground storage of carbon dioxide prospective storage formations must be carefully assessed against number of requirements. Among the most crucial ones is the CO_2 wettability of rocks under reservoir conditions. Composition of those rocks vary significantly but is influenced by the fact that quartz is the second most abundant mineral in earth's continental crust. It is thus CO_2 wettability of quartz which dominates overall CO_2 trapping performance of storage and cap rocks.

Trapping performance of rocks is diminished if they are CO_2 wet. It is widely believed that pristine quartz becomes CO_2 wet at reservoir pressures. It is also an accepted view point that in reality quartz surface is exposed to water and gets hydroxylated and hence water wet. It is thus reasonable to assume that if depleted oil or gas reservoirs are used for storage of CO_2, quartz surfaces of rocks in those reservoirs which were previously exposed to hydrocarbons might be covered with chemisorpt hydrocarbon molecules. CO_2 wettability of these chemically modified rocks is poorly understood and there is a substantial knowledge gap in modern literature and engineering knowledge regarding CO_2 trapping capacity of alkylated quartz.

3. Computational methods

3.1. Overview

With development of information technology, parallel computing, computational hardware and software, methods of computational chemistry and materials science became accessible to broader communities and can be applied to study engineering problems. Among all the molecular dynamics is of particular interest, specifically in petroleum engineering, as it can be used to understand physicochemical processes at the pore level of geological formations. With electronic structure calculations now routinely tackling several hundred atoms, classical mechanics simulations reach the level of several tens of thousands atoms. In terms of time scale the molecular mechanics computations model longer than nanosecond processes. Quality and scope of this modelling was increasing steadily over the last decades with development of modern force fields covering wide range of molecules and crystals. Theoretical predictions are now so trustworthy that they established certain standards in research reporting. Experiential results are often required to be accompanied by theoretical predictions as a gesture of good scientific manners. Moreover, a realm of research activity and output was formed and is based solely on computational results which provide insights otherwise inaccessible. Following up these advances it was chosen to use molecular dynamics as the main method of research, and in this chapter theoretical approaches behind obtained and reported in this dissertation results are outlined.

3.2. Force fields

A collection of mathematical functions which for a given atomic configuration evaluates its energy is called a force field. The mathematical expressions composing a force field may have different forms which normally rooted to the nature of interatomic interactions. A simplified force field may have the following potential energy terms:

$$U(r_1, r_2, \dots r_N) = \sum_{i_{bond}=1}^{N_{bond}} U_{bond}(i_{bond}, r_a, r_b) + \sum_{i_{angle}=1}^{N_{angle}} U_{angle}(i_{angle}, r_a, r_b, r_c)$$
$$+ \sum_{i_{dihd}=1}^{N_{dihd}} U_{dih}\ (i_{dihd}, r_a, r_b, r_c, r_d) + \sum_{i=1}^{N-1} \sum_{j>i}^{N} U_{vdw,electrostatics}(i, j, |r_i - r_j|),$$

where r_1, r_2, ... r_N are positions of the atomic sites, system's configuration; Ubond, Uangle, Udihd are empirical functions representing potential energy of chemical bonds, valance and dihedral angles, Uvdw and Uelectrostatics describe van der Waals and the Coulomb interactions. The first three terms model intramolecular interactions.

In a more general and universal case required for some molecular geometries a force field may include tethered particles and inversion angles forces, external field potentials, see for example (I.T. Todorov & Smith, 2016). Analytical expressions of every term in a force field relay on certain parameters which may be obtained from several sources such as ab-initio calculations and experimental data (X-ray diffraction, infrared spectroscopy, to name a few). Bond stretching term is often represented by a harmonic potential:

$$U(r) = \frac{k_b}{2}(r - r_0)^2,$$

where k_b is the force constant, r is the distance between atoms a and b, and r_0 is the equilibrium bond length.

Common potentials to model angle bending are the harmonic and the harmonic cosine or trigonometric potentials. The harmonic bending potential has analogous to the harmonic stretching potential form:

$$U(\theta) = \frac{k_a}{2}(\theta - \theta_0)^2,$$

where k_a is the force constant, θ is the angle between atoms a, b and c, and θ_0 is the equilibrium bond angle.

The harmonic cosine or trigonometric potential has the following form:

$$U(\theta) = \frac{k_a}{2}(\cos\theta - \cos\theta_0)^2,$$

where k_a is the force constant, θ is the angle between atoms a, b and c, and θ_0 is the equilibrium bond angle.

Energy of torsion is usually expressed in a form of cosine function:

$$U(\varphi) = A[1 + \cos(m\varphi - \delta)],$$

where φ is the torsional angle, A determines the height of the potential barrier, m is the periodicity (number of minima or maxima between 0 and 2π), δ is the phase or equilibrium angle.

The van der Waals interactions can be modelled with variety of analytical functions including the Lennard-Jones, Buckingham and the 12-6 potentials. As an example here the 12-6 potential is used:

$$U(r) = \frac{A}{r^{12}} - \frac{B}{r^6},$$

where A and B are the parameters, and r is the interatomic distance.

Hard repulsive wall of the 12-6 or Lennard-Jones potentials is sometimes softened with the exponential function, like in the Buckingham potential (Buckingham, 1938):

$$U(r) = Aexp\left(-\frac{r}{\rho}\right) - \frac{C}{r^6},$$

where A, ρ and C are the parameters, and r is the interatomic distance.

Parameters of potentials describing van der Waals interactions are normally given for individual atoms. Interactions between unlike atoms are then obtained using combining rules, for example the Lorentz-Berthelot combining rules (Berthelot, 1898; Lorentz, 1881). In the case of classical Lennard-Jones potential (Jones, 1924) the rules distinguish the energy and the distance parameters:

$$U(r) = 4\varepsilon\left[\left(\frac{\sigma}{r}\right)^{12} - \left(\frac{\sigma}{r}\right)^{6}\right],$$

where parameters ε and σ are the depth of the potential well and the distance at which the potential is zero, respectively, and r is the interatomic distance.

For known the energy and the distance parameters of individual atoms, the interaction parameters between the unlike atoms are then obtained as the geometric mean for the energy parameter and as the arithmetic mean for the distance parameter:

$$\varepsilon_{ij} = \sqrt{\varepsilon_i \varepsilon_j},$$

$$\sigma_{ij} = (\sigma_i + \sigma_j)/2,$$

where i and j are indices of interacting atoms.

Unlike other terms for the potential energy, which only approximate the true values, the electrostatic potential energy is expressed exactly:

$$U(r) = \frac{1}{4\pi\epsilon_0}\frac{q_i q_j}{r_{ij}},$$

where ϵ_0 is the vacuum permittivity, q is the atomic charge, and r_{ij} is the distance between atoms with indices i and j.

The neat expression and simplicity of the electrostatic potential are deceptive as assigning charges to atomic sites introduces certain difficulties. From the experimental view point charges can be fit to reproduce thermodynamic data but this is only possible for small molecules (Leach, 2001). On the theoretical side, modern ab-initio calculations are often used to assign partial charges to atoms. In the Mulliken population analysis (Mulliken, 1955) an electron of a molecular orbital contributes to the electronic density of all atoms and to that of the overlapping regions. These contributions are called "populations" and they are naturally obtained from calculations where molecular orbitals are constructed as linear combinations of atomic orbitals (Piela, 2014). When basis functions are not localized, like in case of modelling of periodic systems with plane wave basis sets, the Bader charge analysis (Bader, 1994) is widely used to partition the charge density. It is intuitively understood that electron charge density is at its minimum somewhere in between nuclei of molecular or crystal systems. Sets of all points where the charge density is at its minimum form surfaces perpendicular to which the density is increasing. These minimum charge density surfaces (or zero flux surfaces) designate borders between atoms dividing charge density of molecules or crystals. The partitioning of the electron density in this way expresses the gist of the Bader charge analysis.

Assigning partial charges to atomic sites is not the only task which introduces peculiarities into handling of the electrostatic interactions. The long range nature of these interactions requires special techniques to accurately account for them in periodic or pseudo-periodic systems. A short-range force can be defined as the one which spatial action falls off faster than $1/r^d$, where d is the dimensionality of the system (Allen & Tildesley, 1987). Potentials describing van der Waals interaction are thus belonging to the short-range potentials, action of which

can be cut beyond some reasonably large cutoff distance. On the other hand, the electrostatic interactions are long range and should not be cut to avoid artefacts in molecular dynamics simulations. There are computational methods to treat electrostatic potentials in this rigorous manner. It is believed, see for example (I.T. Todorov & Smith, 2016), that the Ewald summation (Ewald, 1921) is the most suitable method for calculating electrostatic interactions in periodic or pseudo-periodic systems.

The electrostatic energy of a unit cell of a periodic system is given by the infinite over all unit cell replicas sum:

$$U_{electrostatics} = \frac{1}{4\pi\epsilon_0}\frac{1}{2}\sum_{R}^{*}\sum_{i=1}^{N}\sum_{j=1}^{N}\frac{q_i q_j}{|r_{ij}+R|},$$

where R is the vector which connects the unit cell and its images, indicates summation over all lattice vectors ($R = n_1a_1+n_2a_2+n_3a_3$, a are vectors forming edges of the unit cell, n are integers); the asterisk over the outermost sum indicates that for the unit cell (R = 0) interactions i = j are omitted (every charge interacts with every other charge in the unit cell and with all charge replicas including its own, but not with itself).

The sum is only conditionally convergent, meaning that results of the summation depend on the order in which terms are added up. Natural order of the summation is to start from the unit cell, then move to its nearby surrounding replicas and so on in approximately spherical layers.

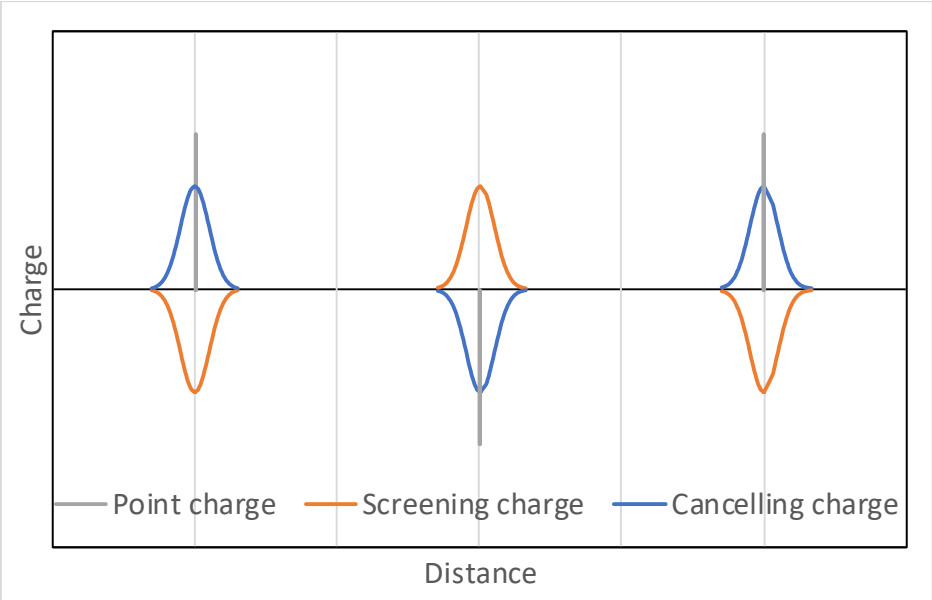

Figure 20. Point charges and auxiliary charge distributions in the Ewald sum.

To replace conditionally convergent infinite series the Ewald method proceeds as follows (Allen & Tildesley, 1987). Each point charge within the unit cell is augmented with a Gaussian charge distribution of opposite sign (screening distribution). This makes the electrostatic potential of screened charges short-ranged. Interactions between these augmented charges are then calculated in real space applying truncation just as for any other short-range potentials. To restore the original system another cancelling Gaussian charge distributions of opposite sign to initially introduced are placed at the same locations of the point charges, see Figure 20. Interactions between these latter distributions are summed up in the reciprocal space. The final step is to eliminate self-interactions of the cancelling charge distributions. As the result the electrostatic energy is represented by two absolutely convergent finite sums, one in the direct space U_{dir}, another in the reciprocal space U_{rec}, plus corrections U_{corr} (Essmann et al., 1995):

$$U_{electrostatics} = U_{dir} + U_{rec} + U_{corr}.$$

The correction term may not only include the self-interactions of the cancelling charge distributions but also intramolecular electrostatic interactions which, when they are incorporated into bond potentials, do not require explicit treatment.

To reduce the computational cost of the Ewald summation from $O(N^{3/2})$ to $O(N \log(N))$ the mesh-based Ewald methods use the discrete fast Fourier transform to approximate the sum

in the reciprocal space by a discrete convolution on an interpolating grid (Darden, York, & Pedersen, 1993; Essmann et al., 1995).

As it is seen from material of this section inter- and intramolecular potentials may take variety of functional forms to fit certain chemical environments. In addition to mentioned in this section potentials modern force fields may include explicit polarization effects and may account for coupling between stretching, bending and torsion (Gonzalez, 2011). When analytical expressions fall short in satisfying practical needs tabulated potential forms may be used. The treatment of short- and long-range potentials is different, specifically in periodic and pseudo-periodic boundary conditions. Special analytical and numeric techniques are used for the electrostatic interactions, namely the Ewald summation. Parametrisation of force fields, in particular assigning partial charges to atomic sites, requires application of methods of computational chemistry, specifically the population or the charge analyses.

Force fields are designed to represent quantum mechanical effects in classical terms using relatively simple analytical expressions, that is why they only work for specific molecular or crystal systems. Some of them reproduce properties of crystals and minerals, like the BKS potential (van Beest et al., 1990), the Heinz team force field (Emami et al., 2014) or the CLAYFF force field (Cygan et al., 2004). Some force fields reproduce properties of organic molecules or hydrocarbons, for example the MM3 (Allinger, Yuh, & Lii, 1989), the MM4 (Allinger, Chen, & Lii, 1996) and the DREIDING (Mayo et al., 1990) force fields. Potentials for inorganic molecules like water and carbon dioxide are well parametrized by the SPC model (H. J. C. Berendsen, Postma, van Gunsteren, & Hermans, 1981) or the TIP4P/2005 model (Abascal & Vega, 2005) for water; the EPM2 model (Harris & Yung, 1995) for carbon dioxide.

3.3. Molecular dynamics

In molecular dynamics a trajectory of a system consisting of N particles is generated by numerically solving the following system of equations of motion:

$$m_i \frac{d^2 r_i}{dt^2} = F_i,$$

where m is the mass of a particle, r is the position of a particle, F is the force acting on a particle, t is time and i = 1, 2, ... N is particle's index.

The force on a particle is found as a negative of the potential gradient:

$$F_i = -\frac{\partial}{\partial r_i} U(r_1, r_2, \dots r_N).$$

The gradient of the potential energy can be found numerically or analytically, the latter is preferred but not always possible.

To start the integration initial positions and velocities must be known. The positions are given by the atomic configuration and velocities are randomly assigned from a Maxwell-Boltzmann distribution corresponding to a certain temperature. The velocities are then adjusted so that the velocity and the angular momentum of the centre of mass are zero. With sufficiently small time step Δt and a = F/m, the integration process proceeds very roughly as follows: positions are updated r(t+Δt) = r(t) + v(t)Δt, velocities are updated v(t+Δt) = v(t) + a(t)Δt, forces and accelerations are recalculated for the new configuration, these steps are repeated for the whole simulation period. To improve accuracy and stability of the integration the Taylor expansions of the position vector for +/-Δt are summed together to cancel odd-degree terms and limit the local integration error (the truncation error) to the forth order in Δt (H. Berendsen & van Gunsteren, 1986; Gonzalez, 2011):

$$r(t + \Delta t) = 2r(t) - r(t - \Delta t) + a(t)\Delta t^2 + O(\Delta t^4).$$

The velocities here can be obtained from the position terms as follows:

$$v(t) = \frac{r(t + \Delta t) - r(t - \Delta t)}{2\Delta t} + O(\Delta t^2).$$

This basic Verlet integration scheme (Verlet, 1967) underpins many practical molecular dynamics integration algorithms including the velocity Verlet (Swope, Andersen, Berens, & Wilson, 1982), which has two major steps. At the first step velocities are propagated to t+Δt/2 and positions are propagated to t+Δt using half step velocities. In the second step the velocities are propagated to a full time step Δt (I.T. Todorov & Smith, 2016):

$$v\left(t + \frac{1}{2}\Delta t\right) = v(t) + \frac{\Delta t}{2}\frac{F(t)}{m},$$

$$r(t + \Delta t) = r(t) + \Delta t v\left(t + \frac{1}{2}\Delta t\right),$$

$$v(t + \Delta t) = v\left(t + \frac{1}{2}\Delta t\right) + \frac{\Delta t}{2}\frac{F(t + \Delta t)}{m}.$$

In between two steps forces at time t+Δt are required to be recalculated at new positions r(t+Δt). The local integration error due to discretisation for both the positions and the velocities for the velocity Verlet algorithm is of the third order in Δt. The global error of the algorithm growths as O(Δt^2) (Mazur, 1997).

Integration of the original equations of motion generates trajectories in the microcanonical or NVE ensemble where the number of particles N, the volume of the simulation box V and the total energy E of simulated systems are conserved. Conservation of the total energy does not guarantee that the potential and the kinetic contributions to it are kept constant. For systems undergoing equilibration this leads to changing temperature. To keep the temperature T constant in the canonical NVT ensemble, or to keep both the temperature T and the pressure P constant in the isothermal-isobaric NPT ensemble the equations of motion have to be modified. The modification is accomplished through weak coupling to an external bath of constant temperature and pressure (H. Berendsen & van Gunsteren, 1986; H. J. C. Berendsen, Postma, van Gunsteren, DiNola, & Haak, 1984):

$$\frac{dr_i}{dt} = v_i - \frac{\beta}{3\tau_P}(P_0 - P),$$

$$\frac{dv_i}{dt} = \frac{F_i}{m_i} + \frac{1}{2\tau_T}\left(\frac{T_0}{T} - 1\right)v_i,$$

where β is the isothermal compressibility; τ_P and τ_T are the time constants of coupling; P_0 and T_0 are the external reference pressure and temperature, respectively.

As it can be seen from the equations in the limit of very large coupling constants the method reproduces original equations of motion and the NVE ensemble. For small coupling constants however, the method does not sample the true canonical NVT ensemble (Gonzalez, 2011). To keep the average temperature of the system constant while allowing for canonically distributed temperature fluctuations the Nose-Hoover method is used (Hoover, 1985; Nosé, 1984). The general idea of the method is to make the heat bath an integral part of the simulated system by introducing an artificial particle with some mass and associated velocity. The magnitude of the mass determines the coupling and influences temperature fluctuations. The equations of motion are solved in modified Nose form.

Some chemical bonds or even geometries of whole molecules can be constrained or fixed in molecular dynamics simulations. To satisfy these constraints the SHAKE procedure (Ryckaert, Ciccotti, & Berendsen, 1977) is used. At first the atoms are moved as if they were unconstrained. Obtained deviations in bond parameters are used to calculate corrective forces used retrospectively. The last step is repeated until bond parameters satisfy the convergence criteria. With the velocity Verlet integration scheme the RATTLE version (Andersen, 1983) of the SHAKE algorithm is used.

From a molecular dynamics simulation many thermodynamic, structural or dynamical properties can be computed (I.T. Todorov & Smith, 2016). Thermodynamic properties as temperature and pressure can be obtained from the kinetic energy and the virial:

$$T = \frac{1}{k_B f} \sum_{i=1}^{N} m_i v_i^2,$$

$$P = \frac{N k_B T}{V} - \frac{1}{3V} \sum_{i=1}^{N} \sum_{j>i}^{N} r_{ij} F_{ij},$$

where k_B is the Boltzmann's constant, f is the number of degrees of freedom, V is the volume of the system.

As an example of the structural property, the radial distribution function in a single component system can be computed from a molecular dynamics simulation as:

$$g(r) = \frac{\rho(r)}{\rho} = \frac{V_{sim}}{V_{shell}(r)} \frac{1}{N} \left[\frac{1}{N} \sum_{i=1}^{N} \sum_{j \neq i}^{N} \delta(r - r_{ij}) \right],$$

where ρ is the density (number of particles per unit volume), V_{sim} is the volume of a simulation box, V_{shell} is the volume of a spherical shell positioned at distance r from the chosen atom.

The radial distribution function can be transformed into the x-ray diffraction structure factor S(Q) via the inverse Fourier transform (Keffer, 2016).

The dynamical properties range from the atomic mean square displacement to correlation functions (Gonzalez, 2011), e.g. the velocity autocorrelation function:

$$C(\tau) = \frac{1}{N}\sum_{i=1}^{N}\frac{1}{t_{max}}\sum_{t=t_0}^{t_{max}}\overline{v_i}(t)\cdot\overline{v_i}(t+\tau),$$

where τ and t denote time.

Fourier transform of the velocity autocorrelation function produces the vibrational density of states, which can be measured using inelastic neutron scattering spectroscopy.

3.4. Density functional theory

The density functional theory is based on two theorems of Hohenberg and Kohn (Hohenberg & Kohn, 1964). The first theorem establishes equivalence of the ground state electronic wave function and the ground state electronic density. The second theorem states that there exists an energy functional which can be minimized by the ground state electronic density, in other words it formulates the variational principle:

$$E[\rho] \geq E[\rho_0] = E_0,$$

where E is the energy functional, ρ is the electronic density, index 0 denotes the ground state.

To construct the energy functional Kohn and Sham used a fictitious system of non-interacting electrons subjected to an external potential (Kohn & Sham, 1965). In the Kohn-Sham formalism the kinetic energy of a many electron system is evaluated as the kinetic energy of non-interacting particles. The approximation introduces an error which is assigned to an undefined part in the energy functional - the exchange-correlation energy:

$$E[\rho(r)] = T_0[\rho(r)] + \frac{1}{2}\int\frac{\rho(r)\rho(r')}{|r-r'|}drdr' + E_{XC}[\rho(r)] + \int u(r)\rho(r)dr,$$

where r is the position vector, T_0 is the kinetic energy of non-interacting particles, E_{XC} is the exchange-correlation energy, u is the external potential.

Here and further on in this section atomic units are used, i.e. numerical values of the electron mass (m_e), the elementary charge (e), the reduced Plank's constant ($\hbar = h/(2\pi)$), and the Coulomb force constant ($1/(4\pi\epsilon_0)$) are set to unity.

To obtain the Kohn-Sham equations a constrained minimization of the energy functional is performed (Piela, 2007). The Lagrange multipliers method is used to maintain normalization of the electronic density and the variations of the total energy δE due to variations of the

orbitals $\delta\phi_i^*$ are demanded to vanish, which results in a system of one electron Schrodinger-like equations:

$$\left[-\frac{1}{2}\nabla^2 + \int \frac{\rho(r')}{|r-r'|}dr' + V_{XC}(r) + u(r)\right]\phi_i(r) = \varepsilon_i\phi_i(r),$$

where V_{XC} is the exchange-correlation potential, ε_i are the lowest eigenvalues of the Kohn-Sham equations which are the energies of non-interacting particle wave functions ϕ_i, pseudofunctions (not true wave functions) or the Kohn-Sham orbitals, which generate the electronic density according to:

$$\rho(r) = \sum_i \phi_i^*(r)\phi_i(r) = \sum_i |\phi_i(r)|^2.$$

In the energy functional $E[\rho]$ the kinetic energy $T_0[\rho]$ is found as a sum of kinetic energies of all electrons described by the Kohn-Sham orbitals:

$$T_0[\rho] = \sum_i \int \phi_i^*(r)(-\nabla^2)\phi_i(r)dr.$$

The dependence of the exchange-correlation energy $E_{XC}[\rho]$ on the electronic density is unknown. There are two classes of widely used approximations: the local density approximation and the generalized gradient approximation.

In the local density approximation the exchange and correlation energies are determined locally as functionals of homogeneous electronic density $\rho=N/V$, where N is the number of electrons and V is the volume of many electron system. As a simple example, the spin-polarized Wigner correlation functional reads as (Gill, 1998; Wigner, 1938):

$$E_C[\rho] = -4a\int \frac{\rho_\alpha\rho_\beta}{\rho}\left(\frac{1}{1+b\rho^{-1/3}}\right)dr,$$

where a and b are parameters; ρ_α and ρ_β are the densities of electrons with +1/2 and -1/2 spins, respectively, and $\rho = \rho_\alpha + \rho_\beta$.

The generalized gradient approximation attempts to correct locality of the local density approximation and acknowledges dependence of the exchange-correlation energy on the density in the whole space. This is done by incorporating the electronic density and its gradient

into the functional, for example, the Perdew and Yue exchange functional reads as (Perdew & Yue, 1986):

$$E_X[\rho] = -\frac{3}{4}\left(\frac{3}{\pi}\right)^{1/3} \int (1 + 1.296s^2 + 14s^4 + 0.2s^6)^{1/15} \rho^{4/3} dr,$$

where the reduced density gradient $s = |\nabla\rho|/(2k_F\rho)$, and $k_F = (3\pi^2\rho)^{1/3}$.

It should be mentioned that despite being approximate, some modern exchange-correlation functional, e.g. Perdew-Burke-Ernzerhof (Perdew et al., 1996), do not rely on empirical parameters but on universal physical constraints like the normalization condition on the exchange-correlation hole (Ernzerhof & Scuseria, 1999).

3.5. Conclusions

Alkylated quartz ability to store CO_2 was not studied before with methods of computational material science, which creates unique challenges. Traditionally molecular dynamics is used to simulate a water droplet on quartz surface in CO_2 environment. There are force fields to describe pristine and hydroxylated quartz surfaces, water and carbon dioxide molecules. Non-bond terms of those fields are mixed using certain rules to form a combined force field for overall quartz-water-CO_2 system. This approach only works if constituent molecules or crystals are not involved in chemical interactions and thus fails if chemisorption plays an important role in formation of the system to be modelled. In the last case a deeper integration of the force fields is required.

Required deeper integration of the force fields can have physicochemical substantiation which is based on demanding ab-initio approaches of the computational chemistry and material sciences. Just as in development of modern force fields, where accurate ab-initio potential energy surface can be approximated with some simplified mathematical models, important for coupling of molecular and crystal force fields parameters can be found using, for example the density functional theory.

The density functional theory is computationally demanding and necessary tool to initiate a new wave of molecular dynamics studies of CO_2 wettability of alkylated quartz surfaces. Found with aid of the density functional theory force field parameters for combined quartz-water-CO_2-hydrocarbons systems shall further be used to propose possible structures of alkylated

quartz surfaces and to investigate CO_2 trapping capacities of minerals partially or fully composed of alkylated quartz.

4. The suitability of spheroidal constructions to estimate the contact angle using snapshots of molecular dynamics simulations

4.1. Annotation

Accurate characterisation of wettability of minerals is important for efficient oil recovery and carbon geo-sequestration. In studies where molecular dynamics simulations are used to compute the contact angle, emphasis is often placed on results or theoretical details of the simulations themselves, overlooking potentially applicable methodologies for determination of the contact angle. In this chapter a concept of a method utilizing spheroidal geometric constructions to estimate the contact angle of a water droplet on silica surface in carbon dioxide atmosphere is outlined and applied to the final snapshots of two molecular dynamics simulation runs. Two carbon dioxide pressures and two wettability modes (hydrophilic and hydrophobic) are examined to assess the method's performance. The outcomes of these calculations are compared with results produced with the iso-density chart method; and good agreement with the latter approach is demonstrated. The proposed method can be used as an alternative, or in conjunction with other techniques, to increase the confidence in contact angle estimations via molecular mechanics calculations. Reliable contact angle estimations on the other hand, can guarantee accurate storage capacity and security of carbon capture and storage projects.

4.2. Introduction and motivation

Carbon capture and storage is a recognized technology that reduces concentration of carbon dioxide in the Earth's atmosphere (IPCC, 2005). Storage capacity and security of formations used to store CO_2 depend on wettability of minerals (Stefan Iglauer, 2017; Stefan Iglauer et al., 2015), specifically quartz in carbon dioxide environment, which was studied experimentally and theoretically (Stefan Iglauer et al., 2014).

There are number of works employing molecular dynamics to simulate the wetting behaviour of water on silica surfaces, in particular in the presence of carbon dioxide and often in the context of carbon geo-sequestration (Bagherzadeh et al., 2012; C. Chen et al., 2018; C. Chen et al., 2017; C. Chen, Wan, et al., 2015; C. Chen, Zhang, et al., 2015; Giovambattista et al., 2007; S. Iglauer et al., 2012; Javanbakht et al., 2015; Liang et al., 2017; Liu et al., 2010; McCaughan et al., 2013; Tenney & Cygan, 2014; Tsuji et al., 2013). In some studies, formation

of the meniscus between two slabs is modelled (Bagherzadeh et al., 2012), in others a cylindrical droplet is used (Tenney & Cygan, 2014). While these approaches offer smaller system sizes and less demanding computations, they may miss important wetting features, like preferential wetting directions on some surfaces (Deng et al., 2018). With increasing computational power of modern computers these techniques become less popular, thus the majority of researchers directly simulate a water droplet on the solid surface and further analyse the results (C. Chen et al., 2017; C. Chen, Wan, et al., 2015; Giovambattista et al., 2007; S. Iglauer et al., 2012; McCaughan et al., 2013).

However, the analysis of such simulation results is often limited to two-dimensional structures. From these, the contact angle is determined via second order polynomial fits to the two-dimensional water droplet profile (Giovambattista et al., 2007), or via drawing contours around two-dimensional water density plots (Bagherzadeh et al., 2012; C. Chen et al., 2017; C. Chen, Wan, et al., 2015; S. Iglauer et al., 2012; McCaughan et al., 2013).

These approaches are local, thus only a certain part of the droplet's profile cross section is considered. When tangential lines are fitted, the three-dimensional nature of the studied systems is lost, which introduces a bias (when projecting three-dimensional objects into two-dimensional space). The approaches lack appreciation of the physico-chemical aspects of droplet formation in the simulation environment. It is meant by the latter that in absence of gravity the system (water droplet) which is destined to minimize its surface energy (and thus the surface area) unavoidably adopts spheroidal shape. In some recent developments, three-dimensionality of spheroidal droplets was taken into account, with water density profiles constructed in cylindrical coordinates, with further fitting of two-dimensional circles to these profiles (S. Iglauer et al., 2012). However, no attempts have been made to use the most natural geometrical constructions and a coordinate system for spherically shaped objects, i.e. spheroidal constructions and the spherical coordinate system. In addition to this, in computational works dedicated to the simulation of wetting behaviour of water in a carbon dioxide environment, there is no discussion of the performance of the methods used to estimate the contact angles or their accuracies. This work thus has a twofold goal. Firstly, it is argued that a holistic method to estimate the contact angle can be developed that (i) treats the overall droplet in three dimensions, based on the spherical coordinate system, and (ii) respects intrinsic physics and the resulting geometry of the simulated structures using

spheroidal geometric construction. Secondly, an attempt is made to initiate a discussion on the performance of the approaches used to compute the contact angles and on the rational choice of parameters used in these approaches.

To this end a water droplet on a pristine (001) α-quartz surface in carbon dioxide environment under 4 and 10 MPa pressure and at 300 K temperature is used. The pristine quartz surface was previously modelled and reconstructed in (Y.-W. Chen et al., 2008; de Leeuw et al., 1999; Eder et al., 2015; Feya et al., 2018; Malyi et al., 2014). According to available information in the literature the pristine surface has two energetically very similar structures the 6-member triangle-like rings and the 6-member ellipse-like rings. To the best of our knowledge the latter and the most stable structure was predicted in (Y.-W. Chen et al., 2008). It was then studied in (Eder et al., 2015; Feya et al., 2018; Malyi et al., 2014), with experimental confirmation reported in (Eder et al., 2015). As far as it is known, there are no reports where the most stable 6-member ellipse-like rings pristine (001) α-quartz surface is explicitly mentioned in the context of its wettability or reconstructed using classical molecular dynamics.

4.3. Method development

Development of the method that is based on the spherical coordinate system requires identification of the smallest radius of a sphere which encapsulates all water molecules of the droplet. If position of this sphere's centre is known, its radius can be easily calculated as the distance to the furthest water molecule. It is thus necessary to find the location of the smallest circumscribing sphere. As it will be clear from the following discussion this is valid for hydrophobic surfaces; with some minor alterations the approach can then be generalized to also include hydrophilic surfaces.

The radius of the circumscribing sphere depends on position of its centre, and it is reasonable to assume that the centre of the minimal radius sphere lies on a normal of the surface which intersects the centre of mass of the droplet. To find the exact position of the centre the following scanning algorithm is introduced, see Figure 21. Suppose that the vertical line through the centre of mass of the water droplet is found as a locus of points with x and y coordinates of the mass centre. A step which divides the line into integer number of segments is selected, e.g. hundredth of the cell height. Looping over every point between segments is performed. For every point a distance to every atom of all molecules comprising the water

droplet is computed. The largest distance is taken as the encapsulating radius corresponding to the given point. The smallest radius identified is the radius of the sphere which was looked for, and the position of the sphere's centre is the position of the point to which this radius corresponds. The search interval is narrowed down next by taking one step backward and one step forward from the point found. This interval is divided into the same number of steps and the search is repeated. The interval is narrowed down until the step size is below a given accuracy threshold, in this work the threshold 10^{-6} A is used.

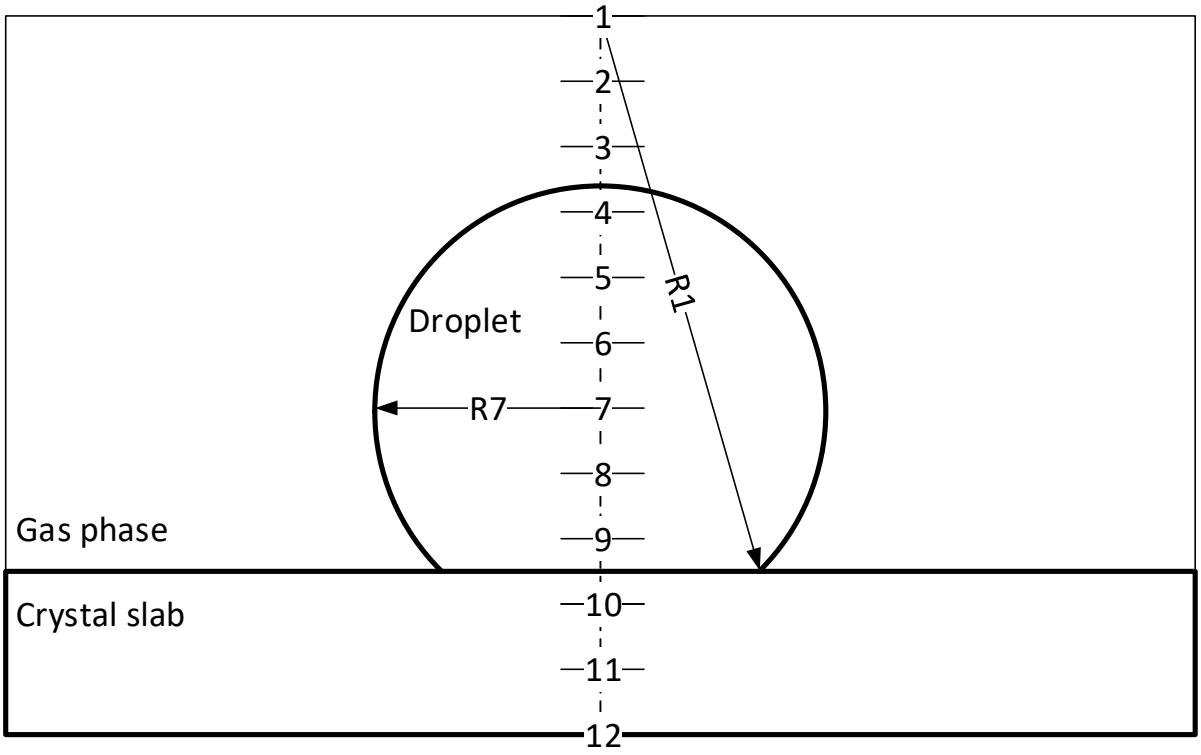

Figure 21. Simulation cell with schematic illustration of hydrophobic surface, water droplet and steps of the scanning algorithm.

The described procedure is exemplified for 12 initial steps in Figure 21. The radii of spheres encapsulating the droplet for steps 1 and 7 are shown as R1 and R7. In the first pass R7 is going to be identified as the smallest droplet encapsulating radius. In the second pass the search interval is going to be narrowed down to the interval between points 6 and 8. In this particular example the radius shown as R7 is going to remain the smallest encapsulating radius until the algorithm reaches the threshold value for the search interval. In a more general case the smallest encapsulating radius is refined over the course of algorithm execution. It is worth noting that there is no need to scan the whole cell. Obviously, the centre of the sphere is inside the droplet, so one only needs to scan from the top of the droplet to its bottom.

For hydrophilic surfaces the above described algorithm finds the wetted radius of the droplet (R_w), see Figure 22. With known droplet height (H_d) this value can be used to identify the position of the centre of the circumscribed sphere (Z_r) and its radius (R):

$$Z_r = Z_{top} - R,$$

$$R = \frac{R_w^2 + H_d^2}{2H_d}.$$

To obtain the latter expression note that in the hydrophilic case, see Figure 22:

$$R^2 = R_w^2 + (R - H_d)^2.$$

For the sake of completeness, it is worth noting that for any two points on circle's contour (R_1, Z_1) and (R_2, Z_2) within one quadrant, not just (0, Z_{top}) and (R_w, 0), a more general expression for the position Z_r can be derived:

$$Z_r = \frac{R_2^2 + Z_2^2 - R_1^2 - Z_1^2}{2(Z_2 - Z_1)}.$$

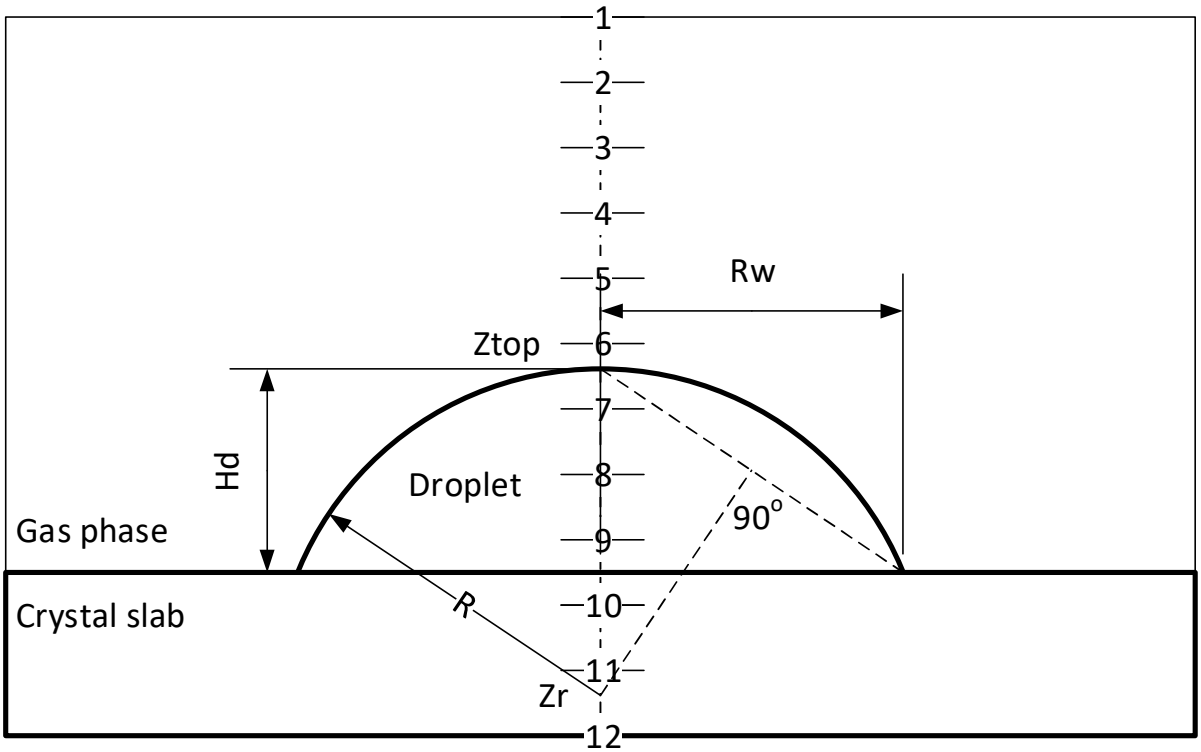

Figure 22. Simulation cell with schematic illustration of a hydrophilic surface, showing the water droplet, steps and elements of the scanning algorithm.

However, in actual simulations droplets rarely resemble perfect spheres or spherical caps. It is thus necessary to refine the radii found. This refinement is done for both, the wetted radius (hydrophilic case) and the radius of the circumscribed sphere. For the latter one density plots in spherical coordinates are constructed by changing the radius from zero to R in small steps dR and calculating the number of molecules in the spherical shell between R and dR, see Figure 23. For a hydrophobic surface the volume of the spherical shell is equal to the volume of a sphere of radius R+dR minus the volume of the sphere of radius R, and minus volume of the spherical cap. For a hydrophilic surface the volume of the spherical shell is equal to the volume of the spherical cap. The spherical cap, just as the spherical shell, is spatially limited between radii R and R+dR. The threshold density, i.e. the density where the water droplet ends (or starts), is assumed to be half the normal water density. The exact figure is taken as 0.033/2 water molecules per cubic angstrom, which corresponds to half of normal water density 1000 kg/m^3. Example plots of the water density in spherical coordinates are illustrated in Figure 28 and Figure 29. To refine the wetted radius in the hydrophilic case an analogous procedure is applied with the only difference being that the cylindrical coordinates are used instead of spherical coordinates. The location of the thin cylinder is at the z coordinate of the radius and its thickness is taken to be 3 A, close to the mean van der Waals diameter of water(Franks, 2000). The dR value is taken to be 0.25 A for both coordinate systems, the spherical and the cylindrical.

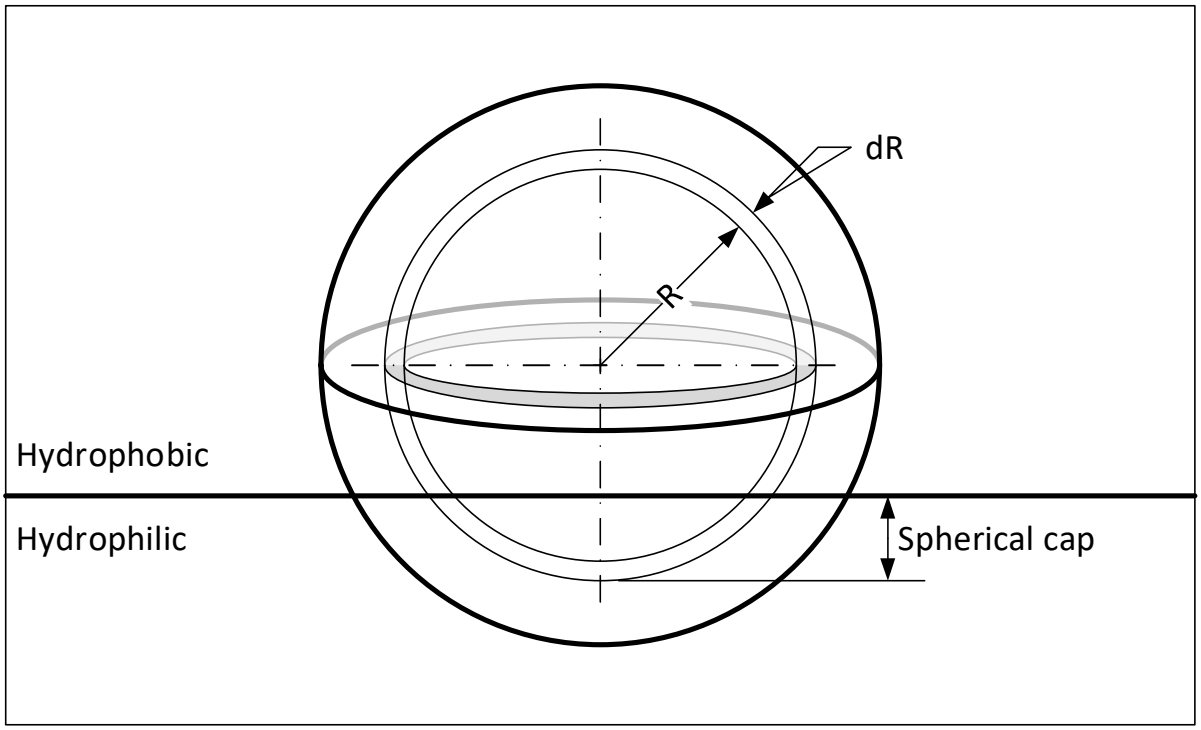

Figure 23. Calculation of water density in spherical coordinates for hydrophobic and hydrophilic surfaces.

When the radius of the water molecules encapsulating sphere, and its position relative to the surface are known calculations of the contact angle become trivial, see Figure 24. With Z_{top} measured from the surface, for the hydrophobic case the contact angle θ is given by:

$$\theta = 180° - \alpha,$$

$$\cos\alpha = \frac{Z_{top} - R}{R}.$$

And for the hydrophilic case the contact angle is:

$$\theta = \alpha,$$

$$\sin\alpha = \frac{R_w}{R}.$$

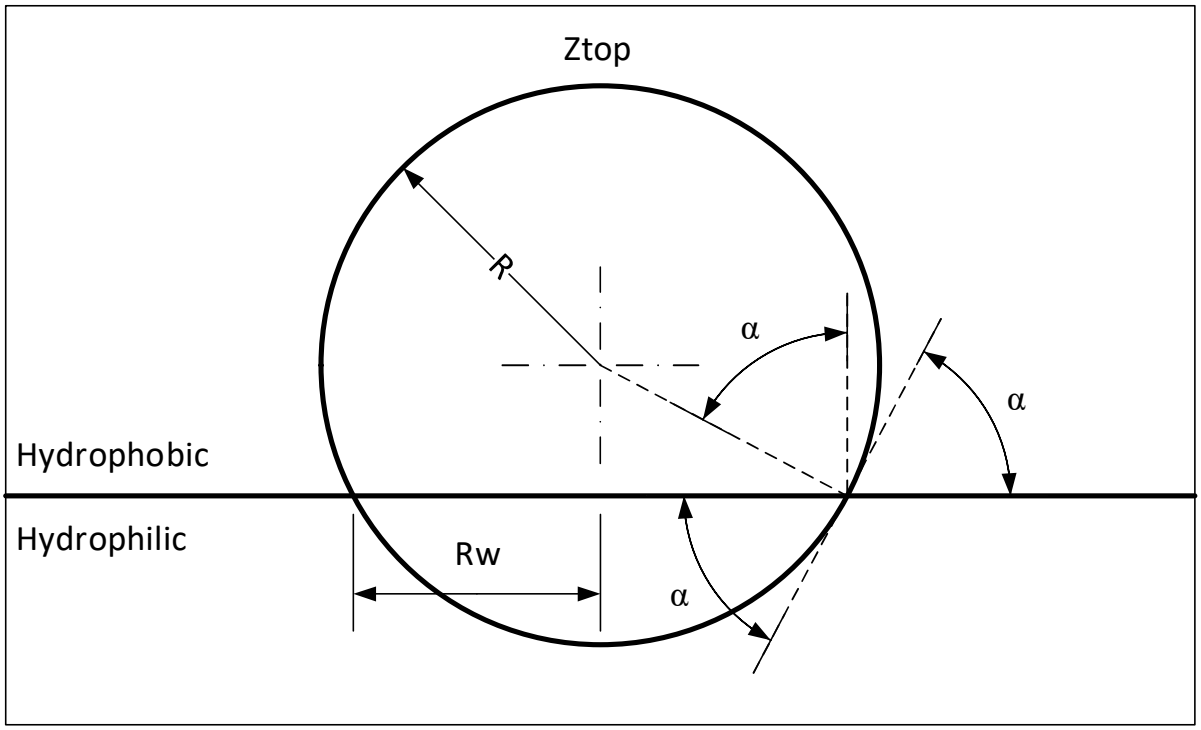

Figure 24. Illustration of contact angle calculations.

As treatment of hydrophilic and hydrophobic surfaces is different, it is important to distinguish between them. Thus the following inequality is used to decide if the surface is hydrophilic,

$$R > H_d.$$

Note that the formulae written in terms of Z_{top} can easily be rewritten in terms of the position of the centre of the circumscribed sphere once it has been found.

Contact angles computed with the circumscribed sphere method are compared with results obtained from the iso-density chart method. In the latter method the droplet is divided into thin circular layers, the thickness is taken to be 0.25 A; in each layer the water density is calculated in the cylindrical coordinate system starting from well outside of the droplet, i.e. the density is calculated in thin rings with dR=0.25 A. By proceeding towards the droplet centre the position of iso-density 0.033/2 water molecules per cubic angstrom is identified in each layer. The resulting line connecting all obtained data points plotted in coordinates height versus radius contours the extent of the droplet, see Figure 32 and Figure 33 for the example. The average radius of the lowest two points is used to set the intersection of the tangential line with the horizontal axis. The next 5, 7 and 9 data points are used to fit the tangential lines to the iso-density and thus three contact angles are determined. An average (over the three values) contact angle is compared with that obtained with the circumscribed sphere method.

Note that in both methods, when calculating water density profiles, the positions of the water molecules are approximated by positions of the oxygen atoms.

4.4. Computational details

A general purpose parallel molecular dynamics simulation package DL_POLY 4.08 was applied to perform computations (Bush, Todorov, & Smith, 2006; Ilian T. Todorov, Smith, Trachenko, & Dove, 2006). Results of the simulations were visualized with VMD (Humphrey, Dalke, & Schulten, 1996) and VESTA (Momma & Izumi, 2008) software, the latter one was also used for manipulations with molecular and periodic structures.

In all classical molecular dynamics simulations integration of the equations of motion was performed with the velocity Verlet algorithm (Swope et al., 1982). The time step in all simulations was set to 2 fs. In the NPT simulations the Nose-Hoover thermostat and barostat (Hoover, 1985; Nosé, 1984) with the relaxation constants 0.05 and 0.5 ps, respectively, were used. In the NVT simulations the Nose-Hoover thermostat with the relaxation constant 0.05 ps was used. Interactions cutoff distance was set to 17 A in all calculations. Electrostatics were computed with the smoothed particle mesh Ewald summation (Darden et al., 1993; Essmann et al., 1995).

4.4.1. Force fields

A set of force fields was employed in this study. The BKS potential (van Beest et al., 1990) was used for the pristine quartz surface. The potential was coupled with the TIP4P/2005 model for water (Abascal & Vega, 2005) and the EPM2 model for carbon dioxide (Harris & Yung, 1995). Only non-bond potential terms were utilized, with all H_2O and CO_2 molecules being treated as rigid bodies. Geometrical details of the rigid bodies are: CO distance (EPM2 CO_2) 1.149 A; OH distance (TIP4P/2005 H_2O) 0.9572 A; OM distance (TIP4P/2005 H_2O) 0.1546 A; HOH angle (TIP4P/2005 H_2O) 104.52°.

The Buckingham potential (Buckingham, 1938) was used to model oxygen-oxygen and silicon-oxygen interactions of the pristine quartz surface:

$$U(r) = Aexp\left(-\frac{r}{\rho}\right) - \frac{C}{r^6},$$

where U is the potential energy of interacting atoms separated by the distance r; A, ρ and C are the parameters of the potential, see Table 1. All silicon-silicon interactions were modelled with electrostatic forces only.

Table 1. The Buckingham potential parameters used for the pristine quartz surface (van Beest et al., 1990).

Interactions	A, kcal/mol	ρ, A	C, kcal/mol A^6	q, e	m, amu
O-O	$3.20304 \cdot 10^4$	0.3623188	$4.03609 \cdot 10^3$	O=-1.2	O=15.9994
Si-O	$4.15225 \cdot 10^5$	0.2052124	$3.07983 \cdot 10^3$	Si=2.4	Si=28.0855

The Lennard-Jones potential was used to model dispersion interactions of water, carbon dioxide and the ions for the pristine quartz surface:

$$U(r) = 4\varepsilon\left[\left(\frac{\sigma}{r}\right)^{12} - \left(\frac{\sigma}{r}\right)^{6}\right].$$

Parameters of the potential ε and σ are given in Table 2.

Table 2. The Lennard-Jones potential parameters used to model CO_2-H_2O-SiO_2 systems (Abascal & Vega, 2005; Harris & Yung, 1995; S. Iglauer et al., 2012; van Beest et al., 1990).

Atomic sites	ε, kcal/mol	σ, A	q, e	m, amu
C (CO_2)	0.05591	2.757	0.6512	12.0107
O (CO_2)	0.16001	3.033	-0.3256	15.9994
O (H_2O)	0.18523	3.1589	0	15.9994
H (H_2O)	0	0	0.5564	1.0080
M (H_2O)	0	0	-1.1128	0
Si (SiO_2)	0.12751	3.795	2.4	28.0855
O (SiO_2)	0.15504	3.154	-1.2	15.9994

The interaction parameters between the unlike atoms were obtained as the geometric mean for the energy parameter and as the arithmetic mean for the distance parameter (the Lorentz-Berthelot combining rules (Berthelot, 1898; Lorentz, 1881)):

$$\varepsilon_{ij} = \sqrt{\varepsilon_i \varepsilon_j},$$

$$\sigma_{ij} = (\sigma_i + \sigma_j)/2,$$

where i and j are indices of the unlike atoms.

4.4.2. Reconstruction of the pristine quartz surface

From the hexagonal unit cell of α-quartz (Levien et al., 1980) shown in Figure 25 a super cell 2x2x1 was created. An orthorhombic cell for further preparation of the pristine surface was then extracted from the super cell (Adeagbo et al., 2008), see Figure 25. There are 18 atoms in the orthorhombic cell, 6 silicon atoms and 12 oxygen atoms.

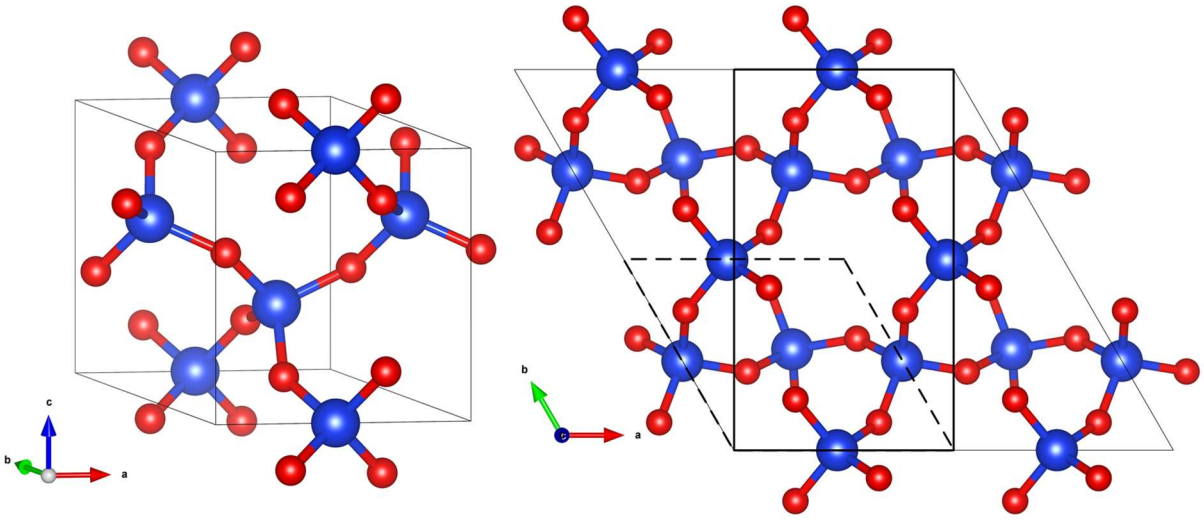

Figure 25. Quartz unit cells used in this work. Left: primitive hexagonal unit cell of α-quartz, isometric view. Right: reconstruction of the orthorhombic cell (solid bold rectangle) from 2x2x1 super cell, top view (dashed parallelogram shows the primitive cell). Red balls - oxygen atoms, blue balls - silicon atoms.

Crystallographic lattice vectors of the orthorhombic cell amount to: a=4.916 A, b=8.515 A, c=5.405 A. Out of this orthorhombic cell a super cell 12x7x12 was constructed and used to equilibrate the quartz crystal at 1 atm pressure and 300 K temperature for 10^5 steps. The system was simulated in the NPT ensemble. Lattice vectors of the equilibrated orthorhombic cell were found to be a=4.940 A, b=8.557 A, c=5.432 A, which are only 0.5% larger than the crystallographic values obtained from (Levien et al., 1980). Using this equilibrated orthorhombic cell a 20x12x4 slab was constructed. Every uncoordinated oxygen atom at the top of the slab was shifted from the host silicon atom towards the neighbouring silicon atom in x and y directions by 0.6 A to build precursors of the Si-O-Si bridges. After that the slab was relaxed at 10 K for 10^5 steps to form proper Si-O-Si bridges and the initial ordered surface structure. The system was simulated in the NVT ensemble. During the relaxation and in all subsequent simulations described in this work the bottom layer (in terms of the unit cell height) of the four-layer slab was kept frozen to emulate the bulk crystal. The surface was prepared in a simulation box which had the same dimensions as the box used for the fully

assembled quartz-water-CO_2 systems. Arrangement of the very top atoms of the surface is the same as in the lowest energy surface obtained in (Feya et al., 2018; Malyi et al., 2014). The surface consists of 6-member ellipse-like rings, Figure 26.

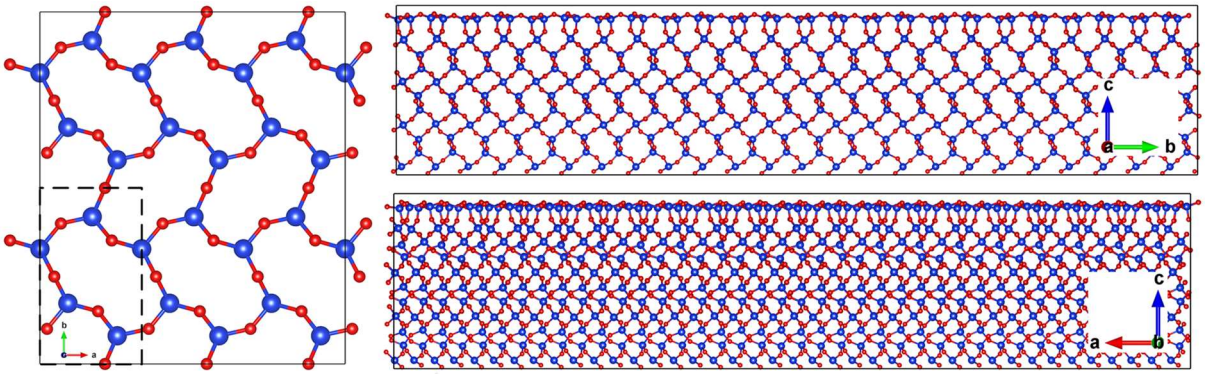

Figure 26. Four-layer quartz slab used in this work. Left: view of the super cell 3x2x1 along z direction with only top atoms shown for clarity (the orthorhombic unit cell is highlighted with dashed rectangle). Right: slab views along x (right top) and y (right bottom) directions. Red balls - oxygen atoms, blue balls - silicon atoms.

4.4.3. Simulation setups

Utilizing above described force fields and the pristine quartz surface two simulation models were constructed with two different carbon dioxide pressures (4 and 10 MPa). Temperature in all simulations was set to 300K. Preliminary equilibration of carbon dioxide and water with the subsequent construction of the models was performed.

Two boxes 120x120x80 A for carbon dioxide and 50x50x50 A for water (the TIP4P/2005 (Abascal & Vega, 2005) were used to pre-equilibrate uniformly distributed molecules at 300K. Density of carbon dioxide at given pressure and temperature were used to determine the volume per every molecule, this density was taken from the NIST data book at 300 K and at the relevant pressures of 4 and 10 MPa (webbook.nist.gov). Water density was taken to be 1000 kg/m^3. Dynamics of these three systems (one for H_2O and two for CO_2) were modelled in the NVT ensembles. Overall $5 \cdot 10^5$ steps were performed for CO_2 and 10^5 for H_2O.

On top of the pre-equilibrated quartz slabs a half sphere of radius 24 A was filled with water molecules from above described box. Overall 772 TIP4P/2005 water molecules fit into the half sphere. These "water droplets" were placed in the centre of the slabs. The rest of the space up to 60 A above from the surface was filled with pre-equilibrated carbon dioxide. There were 642 and 5559 CO_2 molecules above the pristine surface at 4 and 10 MPa, respectively. A gap of 1.5 A starting from four quartz unit cell heights (the slab's height) was left empty to avoid

overlap of atoms and molecules. Note that actual initial distance between top slab atoms and water and gas molecules was slightly larger due to surface construction during relaxation and disposition of molecules in the pre-equilibration boxes, thus molecules located exactly at the border were rejected upon filling the simulation boxes. Vacuum space of 70 A was provided above the gas phase. All simulations were performed with periodic boundary conditions in x and y directions. In z direction a repulsive force was initially set at 60 A above from the surface:

$$F = k(z_0 - z), z > z_0,$$

where k=0.24 kcal/mol (1 kJ/mol) - is the force constant, and z_0 is the position of the repulsive potential.

The position of this repulsive wall was then corrected in such a way that the density of the pre-equilibrated carbon dioxide filling space above the surface matched its physical density at given pressure and temperature. In all cases the potential was never displaced towards the surface by more than 6 A, see Table 3. Minimal distance to the repulsive potential of more than 54 A ensures that the contact angle at the surface is not affected by perturbations in the CO_2 density caused by the wall.

Dynamics of two prepared quartz-water-carbon dioxide systems were simulated in the NVT ensembles. Overall 10^6 steps were performed for every system, 2 ns simulation time, out of which 10^5 were equilibration steps. Dimensions of the simulation boxes were 98.81x102.68x151.73 A. Figure 27 demonstrates the initial simulation setups for two studied systems. Main computational details are summarized in Table 3.

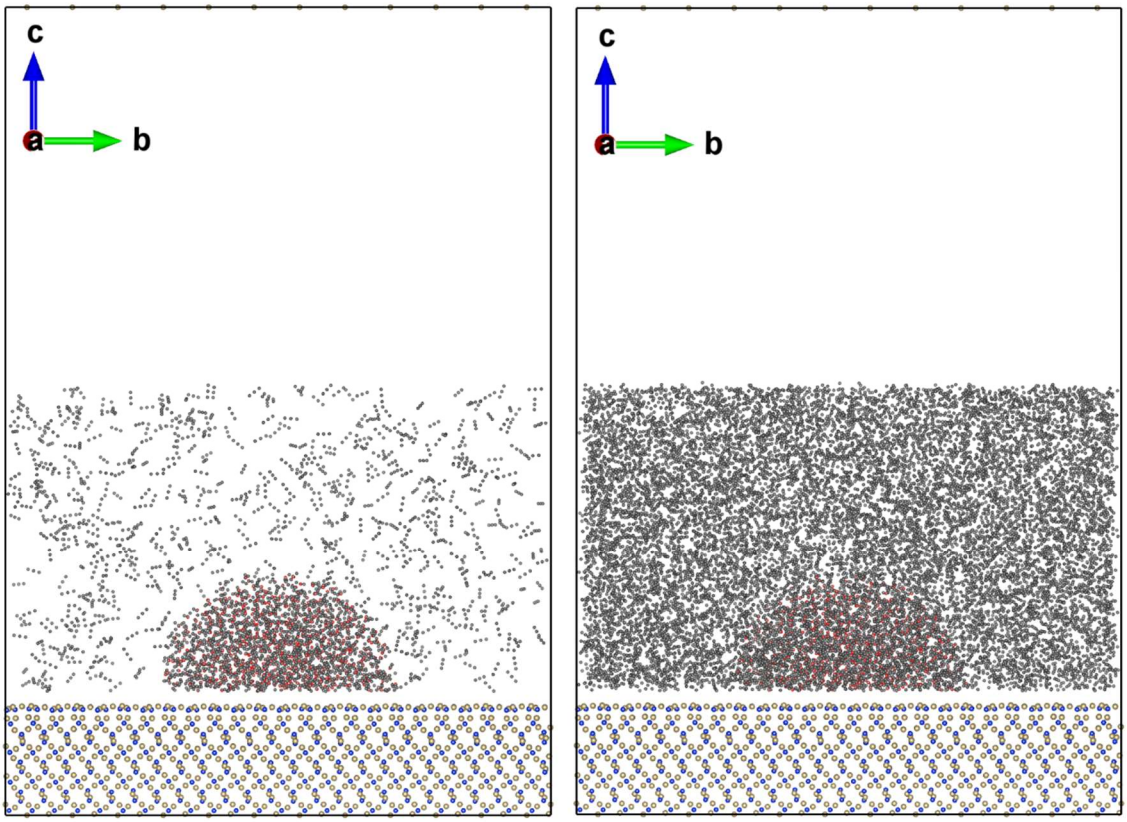

Figure 27. Initial simulation setups for systems investigated at two CO_2 pressures - 4 MPa (left) and 10 MPa (right). The hemispherical water droplets above the quartz surfaces surrounded by CO_2 molecules are clearly visible.

Table 3. Summary of computational details.

Parameters	System 1	System 2
CO_2 pressure, MPa	4	10
Temperature, K	300	
Force fields	BKS, TIP4P/2005, EPM2	
Interactions cutoff, A	17	
Time step, ps	0.002	
Number of steps (equilibration steps)	10^6 (10^5)	
Ensemble	NVT	
Thermostat	Nose-Hoover	
Thermostat relaxation constant, ps	0.05	
Repulsive potential z_0, A	54.64	54.31
Repulsive potential k, kcal/mol	0.24	
Half sphere droplet radius, A	24	

Parameters	System 1	System 2
H_2O molecules	772	
CO_2 molecules	642	5559
Slab top layer	240(Si_6O_{12})	
Slab two middle layers	480(Si_6O_{12})	
Slab frozen (bottom) layer	240(Si_6O_{12})	
Slab unit cell dimensions, A	4.94x8.56x5.43	
Slab dimensions in unit cells	20x12x4	
Simulation box dimensions, A	98.81x102.68x151.73	

4.5. Method application and discussion

For both systems investigated the very last snapshots of the simulations were analysed using above described methodology. Obtained results of the contact angle analysis are summarized in Table 4.

Table 4. Contact angle computational results.

Initial simulation setup	System 1	System 2
CO_2 pressure, MPa	4	10
Circumscribed sphere radius, A	31.375	22.125
Position of sphere's centre with respect to the surface, A	-12.82	1.88
Contact angle (circumscribed sphere method), degrees	65.9	94.9
Contact angle (iso-density chart method), degrees	69.0 (+/-4.7)	92.6 (+/-2.6)

It is noteworthy to see how the two methods, the circumscribed sphere method and the iso-density chart method, arrived at essentially the same results using different routes. The largest discrepancy in found contact angles is in the range of 5%. Thus, the surface at 4 MPa of CO_2 pressure is hydrophilic (the contact angle is less than 90°), the surface at 10 MPa of CO_2 pressure is slightly hydrophobic (the contact angle is more than 90°). These results are in agreement with previously reported simulation data where the contact angles were found to be 70° and 80° at 300 K and 4 and 10 MPa of CO_2 pressure, respectively (S. Iglauer et al., 2012). In an experimental study conducted at 298 K, during repeated exposure to CO_2, the contact

angles of water droplets on quartz substrates were found to be 90° and 80° at 4 and 10 MPa of pressure, respectively (Bikkina, 2011), which is in reasonable agreement with obtained here values.

It should be noted here that simulations executed in this work are organized such that the initial atomic configurations are close to the equilibrium (the contact angle of the hemispherical droplet is 90°, c.f. to computed above 65.9° and 94.9°). In addition to this, all elements of the initial setups (the slab, CO_2, water molecules of the droplet) are relaxed and pre-equilibrated. It thus follows that 2 ns simulation time is sufficient for statistically significant results extracted from a single simulation snapshot. Quantitative validation for the latter statement can be produced using tails of generated trajectories. From the last 50 000 steps (0.1 ns simulation time) five simulation snapshots separated by 10 000 steps were extracted and the contact angles were computed using the circumscribed sphere method. For the systems at 4 and 10 MPa CO_2 pressure the contact angles amounted to 62.6° (+/-3.3) and 96.5° (+/-1.7), respectively. Small error bars indicate that the systems are well equilibrated and obtained results used for comparison with works mentioned in the previous paragraph are significant.

Water density profiles constructed in spherical coordinates are shown in Figure 28 and Figure 29. Approaching the spheres' centres from the infinity, the threshold water density (0.033/2 water molecules per cubic angstrom) signals where the droplets start. A common feature of both plots is relatively slow increase in the density in the beginning and its abrupt decrease in the end. A slow threshold approach makes refinement of droplets' radii relatively reliable, as the density increases from zero to 0.033/2 water molecules per cubic angstrom over the distance of several angstroms.

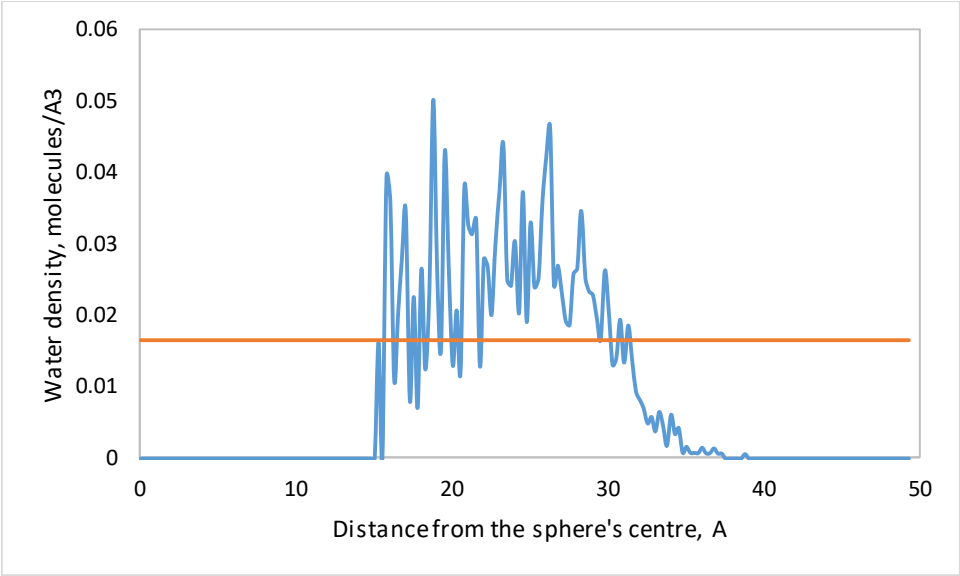

Figure 28. Water density in spherical coordinates for the system at 4 MPa CO_2 pressure. Horizontal line shows half of water's normal density.

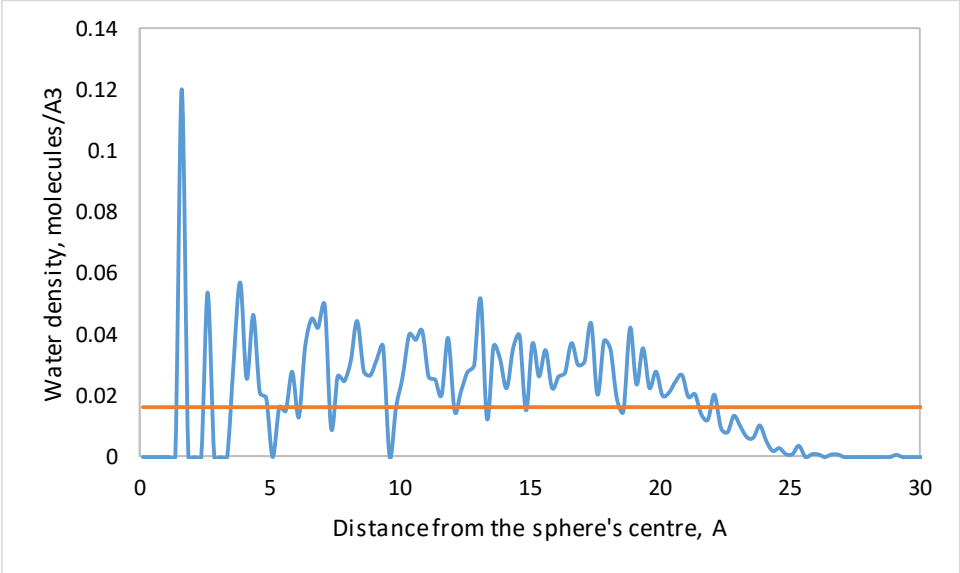

Figure 29. Water density in spherical coordinates for the system at 10 MPa CO_2 pressure. Horizontal line shows half of water's normal density.

Spheres circumscribed around water droplets and their relative positions with respect to the surfaces are presented in Figure 30 and Figure 31. As expected, circumscribed spheres average fuzzy borders of the droplets eliminating the directional bias.

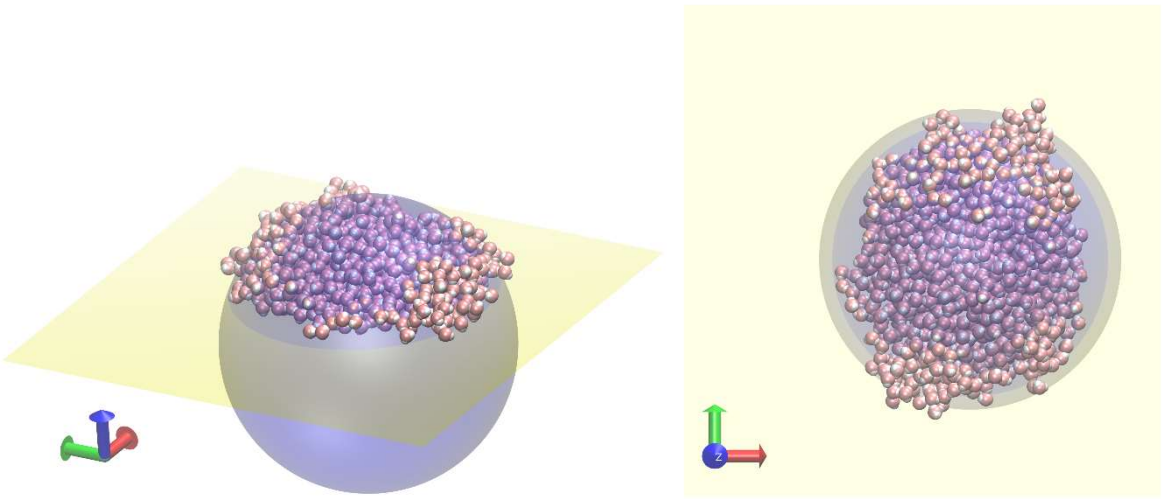

Figure 30. Water droplet and its circumscribed sphere on the quartz surface at 4 MPa CO_2 pressure, isometric view (left) and top view (right). Orange balls are oxygen atoms and white balls are hydrogen atoms of the TIP4P/2005 water.

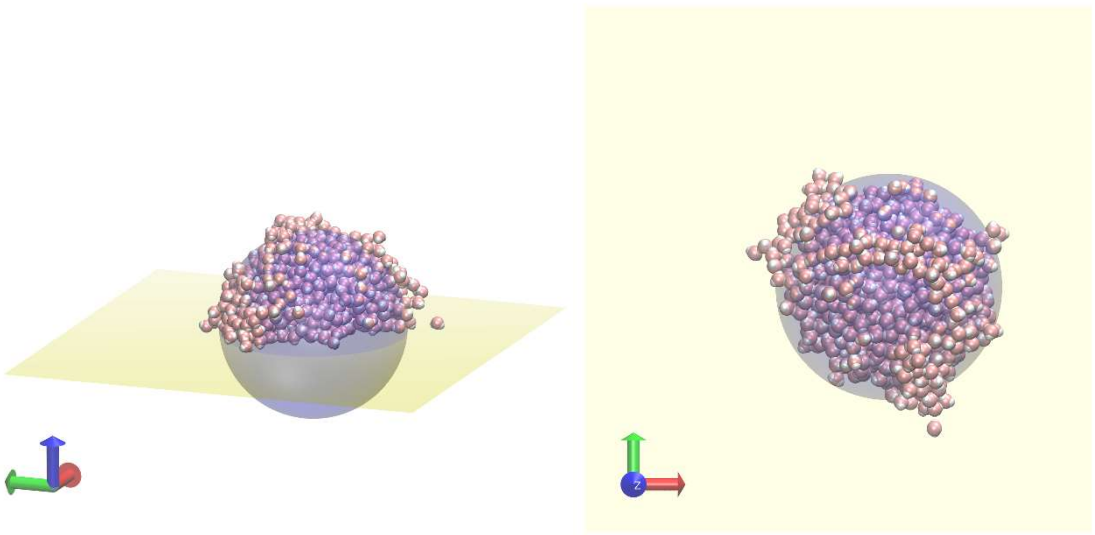

Figure 31. Water droplet and its circumscribed sphere on the quartz surface at 10 MPa CO_2 pressure, isometric view (left) and top view (right). Orange balls are oxygen atoms and white balls are hydrogen atoms of the TIP4P/2005 water.

Iso-density charts used to compare results of the contact angle calculations with the circumscribed sphere method are shown in Figure 32 and Figure 33. The circumscribed spheres almost average the iso-density constructed in cylindrical coordinates, especially at 10 MPa CO_2 pressure. The contact angles calculated using three sets of data points (5, 7 and 9) average the iso-densities close to the surface and show good agreement between each

other (error bars are less than 7%): 69.0° (+/-4.7°) and 92.6° (+/-2.6°) for systems at 4 and 10 MPa of CO_2 pressure, respectively.

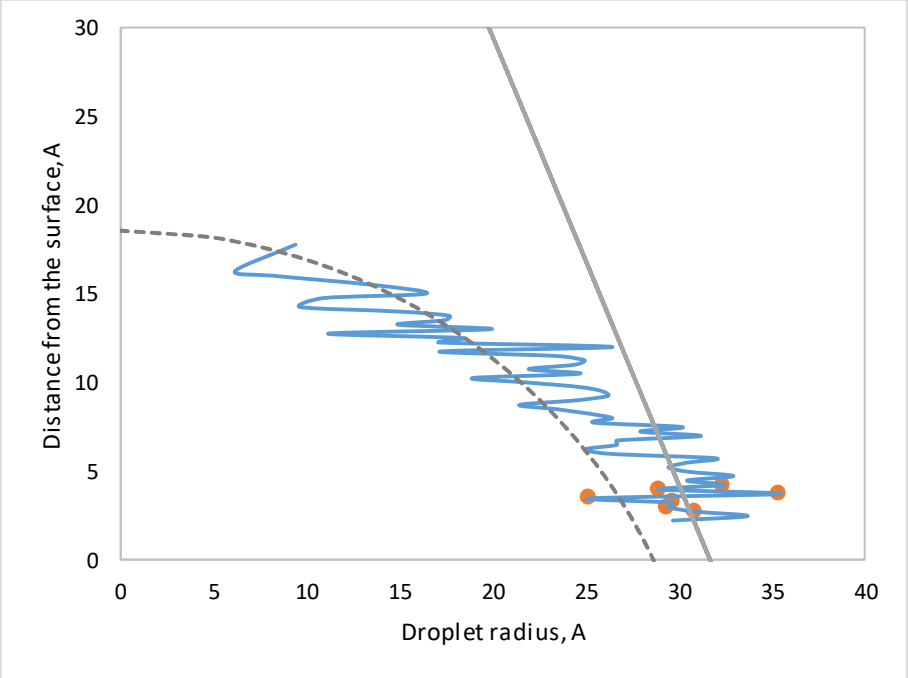

Figure 32. Iso-density chart constructed in cylindrical coordinates for a water droplet on a pristine quartz surface at 4 MPa CO_2 pressure. Blue line shows half of water normal density. Red dots depict data points used to fit the tangential line, the straight line (5, 7 and 9 points were used for the averaging, the case for 7 points is shown). The dashed line shows the circumscribed sphere contour found in the spherical coordinates.

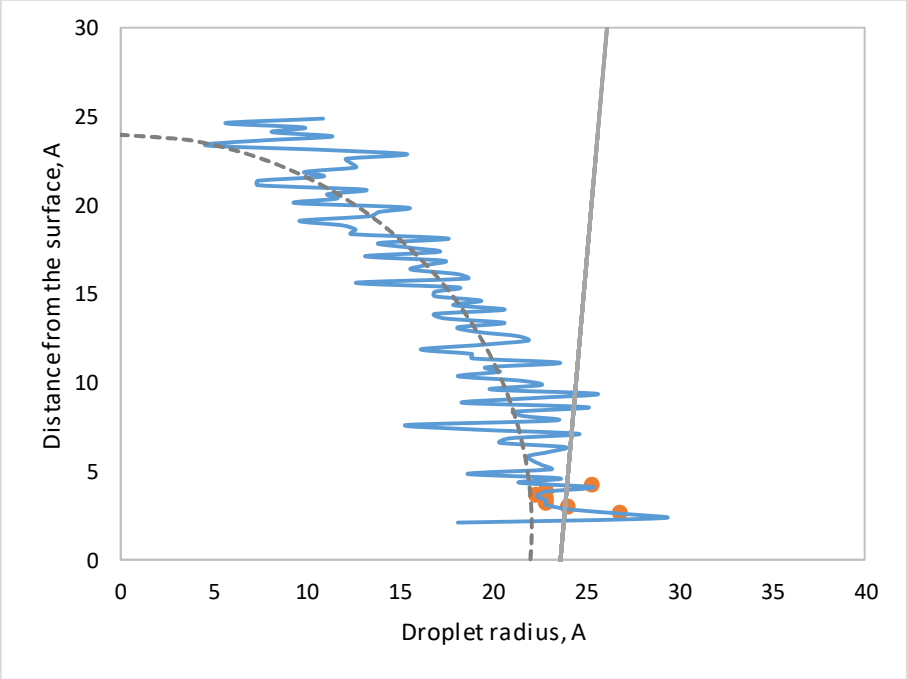

Figure 33. Iso-density chart constructed in cylindrical coordinates for a water droplet on a pristine quartz surface at 10 MPa CO_2 pressure. Blue line shows half of water normal density. Red dots depict data points used

to fit the tangential line, the straight line (5, 7 and 9 points were used for the averaging, the case for 7 points is shown). The dashed line shows the circumscribed sphere contour found in the spherical coordinates.

Obtained numerical parameters and overall agreement between two methods used to determine the contact angle, as well as visual inspection of the simulation snapshots and the diagrammatic data demonstrate that the spheroidal constructions and the spherical coordinate system have promising potential in the area. The algorithms proposed here are simple and can be intuitively understood, and the required computational effort to analyse a simulation snapshot is minor.

4.6. Conclusions

The concept of how to determine computational contact angles of a liquid droplet resting on a solid surface from individual snapshots of molecular dynamics simulations have been formulated, implemented and analysed in this study. Spherical coordinates to circumscribe a sphere around given configuration of water molecules form the basis of the method, which is thus natural and consistent with the droplet's geometric computational framework. The method also shows good agreement with the iso-density chart method which was applied here.

The contact angle of a water droplet on the most stable 6-member ellipse-like rings (001) surface of α-quartz, which was reconstructed here using classical molecular dynamics, was found to be 66 and 95° at 4 and 10 MPa of CO_2 pressure, respectively.

Procedures used to compute the contact angles on basis of molecular dynamics output have deficiencies and limitations when applied on their own. The circumscribed sphere method in its current implementation is best suited for hydrophobic surfaces, but otherwise sensitive to the integrity of the water droplet and may need pre-processing for droplets with poorly defined borders to remove escaped (from the main body of water) molecules. The iso-density chart method is less sensitive to integrity, but local in nature and thus requires caution when fitting the tangential line. Without a universal unbiased method, a combination of several approaches can complement each other in providing a confident estimate of the contact angle from molecular dynamics computations.

5. Application of the CLAYFF and the DREIDING force fields for modelling of alkylated quartz surfaces

Chapter 5 is not available in this version of the thesis.

The chapter has been published as:
Abramov, A., & Iglauer, S. (2019). Application of the CLAYFF and the DREIDING Force Fields for Modeling of Alkylated Quartz Surfaces. *Langmuir, 35*(17), 5746-5752. doi:10.1021/acs.langmuir.9b00527

6. Wettability of fully hydroxylated and alkylated (001) alpha-quartz surface in carbon dioxide atmosphere

Chapter 6 is not available in this version of the thesis.

The chapter has been published as:
Abramov, A., Keshavarz, A., & Iglauer, S. (2019). Wettability of fully hydroxylated and alkylated (001) alpha-quartz surface in carbon dioxide atmosphere. *The Journal of Physical Chemistry C, 123*(14), 9027–9040. Doi: 10.1021/acs.jpcc.9b00263

The Open Access version of this paper is available at:
https://ro.ecu.edu.au/ecuworkspost2013/6061/

7. Conclusions

Carbon dioxide capture and storage was proposed as a technologically and economically feasible solution to reduce carbon dioxide content in earth's atmosphere and thus avert global warming. To ensure secure long term underground storage of carbon dioxide prospective storage formations must be carefully assessed against number of requirements. Among the most crucial ones is the CO_2 wettability of rocks under reservoir conditions. The composition of those rocks vary significantly and are influenced by the fact that quartz is the second most abundant mineral in the earth's continental crust. Thus the CO_2 wettability of quartz dominates the overall CO_2 trapping performance of storage and cap rocks. If depleted oil or gas reservoirs are used for storage of CO_2 quartz surfaces of rocks in reservoirs which have been previously exposed to hydrocarbons might be covered with chemisorpt hydrocarbon molecules. The CO_2 wettability of these chemically modified rocks is poorly understood and there is a substantial knowledge gap in modern literature and engineering knowledge regarding CO_2 trapping capacity of alkylated quartz.

To model quartz surfaces with chemisorpt hydrocarbons both CLAYFF and DREIDING force fields were coupled at atomic site charge level using the DFT and the Bader charge analysis. The charge of the hydroxyl hydrogen substituted with a pentyl group was reallocated to the newly formed oxygen-carbon bond connecting the C_5H_{11} group and quartz surface. Redistribution of the charge in proportion 0.796 to 0.204 for the carbon and the oxygen atoms, respectively, is shown to be consistent with the DFT results in terms of the absolute charge difference between the DFT charges and the force field charges on atoms of the OC bond; and in terms of the relative charges on both oxygen atoms of the geminal silanol group. Actual values of charges on the oxygen and the carbon atoms are computed to be -0.863301 and 0.338301 e.

Augmented with modified charges of the OC bond, CLAYFF and the DREIDING force fields were applied to solve a practical problem of calculating the contact angle of a water droplet on alkylated quartz surfaces in a CO_2 environment. A systematic computational study of wettability of fully hydroxylated and alkylated (001) α-quartz surface under 10 MPa pressure of carbon dioxide at 300 K with respect to surface concentration of pentyl groups was performed. Considered concentrations of the alkyl groups varied from 0.29 to 4.63 C_5H_{11}/nm^2. It was shown that when the surface density of pentyl groups increases from 0.29 to

3.18 C_5H_{11}/nm^2 the contact angle of a water droplet changes from 10-20 to 180°, thus the surface becomes completely hydrophobic.

A comprehensive description of wettability of alkylated quartz surface requires three parameters: the theoretical contact angle, the apparent contact angle and the hidden contact angle. These contact angles are determined at the tip level of pentyl groups and the level of the quartz surface. The hidden contact angle is calculated as the angle of a water "skirt", which is formed between the level of the quartz surface and the tip level of pentyl groups. The hidden contact angle remains relatively small (less than 90°) up to the threshold pentyl density of 2.604 C_5H_{11}/nm^2, after which it rather abruptly increases to 180°. Such a behaviour is termed as the binary wettability, when the surface is either hydrophilic or extremely hydrophobic, with intermediate wetting regime observed only in a very narrow range of the surface pentyl density of 0.29 C_5H_{11}/nm^2. It was concluded that this binary wettability of alkylated quartz surface originates from the steric effects preventing water molecules from reaching the quartz surface.

Additionally, the concept and the method of how to determine computational contact angles of a liquid droplet resting on a solid surface from individual snapshots of molecular dynamics simulations have been formulated, implemented and analysed. Spherical coordinates to circumscribe a sphere around given configuration of water molecules form the basis of the method, which is thus natural and consistent with the droplet's geometric computational framework. The method also shows good agreement with the iso-density chart method which was used here. Apart from proposed original method to determine the computational contact angle, this research contributes to the scientific and engineering community in two ways. Firstly, there is a fundamental contribution in the form of modified and adapted for the modelling of the alkylated quartz force fields. Secondly, there is a practical contribution in the form of a deeper understanding of the wetting processes of chemically modified with hydrocarbons quartz surfaces.

8. References

Abascal, J. L. F., & Vega, C. (2005). A general purpose model for the condensed phases of water: TIP4P/2005. *The Journal of Chemical Physics, 123*(23), 234505. doi:10.1063/1.2121687

Adeagbo, W. A., Doltsinis, N. L., Klevakina, K., & Renner, J. (2008). Transport Processes at α-Quartz–Water Interfaces: Insights from First-Principles Molecular Dynamics Simulations. *ChemPhysChem, 9*(7), 994-1002. doi:10.1002/cphc.200700819

Al-Yaseri, A. Z., Lebedev, M., Barifcani, A., & Iglauer, S. (2016). Receding and advancing (CO2+brine+quartz) contact angles as a function of pressure, temperature, surface roughness, salt type and salinity. *The Journal of Chemical Thermodynamics, 93*, 416-423. doi:https://doi.org/10.1016/j.jct.2015.07.031

Al-Yaseri, A. Z., Roshan, H., Lebedev, M., Barifcani, A., & Iglauer, S. (2016). Dependence of quartz wettability on fluid density. *Geophysical Research Letters, 43*(8), 3771-3776. doi:10.1002/2016GL068278

Ali, M., Al-Anssari, S., Arif, M., Barifcani, A., Sarmadivaleh, M., Stalker, L., . . . Iglauer, S. (2019). Organic acid concentration thresholds for ageing of carbonate minerals: Implications for CO2 trapping/storage. *Journal of Colloid and Interface Science, 534*, 88-94. doi:https://doi.org/10.1016/j.jcis.2018.08.106

Allen, M. P., & Tildesley, D. J. (1987). *Computer Simulation of Liquids*: Clarendon Press.

Allinger, N. L., Chen, K., & Lii, J.-H. (1996). An improved force field (MM4) for saturated hydrocarbons. *Journal of Computational Chemistry, 17*(5-6), 642-668.

Allinger, N. L., Yuh, Y. H., & Lii, J. H. (1989). Molecular mechanics. The MM3 force field for hydrocarbons. 1. *Journal of the American Chemical Society, 111*(23), 8551-8566. doi:10.1021/ja00205a001

Andersen, H. C. (1983). Rattle: A "velocity" version of the shake algorithm for molecular dynamics calculations. *Journal of Computational Physics, 52*(1), 24-34. doi:https://doi.org/10.1016/0021-9991(83)90014-1

Anderson, R. S., & Anderson, S. P. (2010). *Geomorphology: The Mechanics and Chemistry of Landscapes*: Cambridge University Press.

Arif, M., Barifcani, A., Lebedev, M., & Iglauer, S. (2016). Structural trapping capacity of oil-wet caprock as a function of pressure, temperature and salinity. *International Journal of Greenhouse Gas Control, 50*, 112-120. doi:https://doi.org/10.1016/j.ijggc.2016.04.024

Atkins, P. W., & De Paula, J. (2006). *Atkins' Physical chemistry* (8 ed.): Oxford University Press.

Bachu, S. (2003). Screening and ranking of sedimentary basins for sequestration of CO2 in geological media in response to climate change. *Environmental Geology, 44*(3), 277-289. doi:10.1007/s00254-003-0762-9

Bader, R. F. W. (1994). *Atoms in Molecules: A Quantum Theory*: Oxford University Press.

Bagherzadeh, S. A., Englezos, P., Alavi, S., & Ripmeester, J. A. (2012). Influence of Hydrated Silica Surfaces on Interfacial Water in the Presence of Clathrate Hydrate Forming Gases. *The Journal of Physical Chemistry C, 116*(47), 24907-24915. doi:10.1021/jp305529d

Balascio, J. F., & Lind, T. (1997). The growth of piezoelectric alpha quartz crystals. *Current Opinion in Solid State and Materials Science, 2*(5), 588-592. doi:https://doi.org/10.1016/S1359-0286(97)80050-2

Berendsen, H., & van Gunsteren, W. (1986). *Practical algorithms for dynamic simulations*.

Berendsen, H. J. C., Postma, J. P. M., van Gunsteren, W. F., DiNola, A., & Haak, J. R. (1984). Molecular dynamics with coupling to an external bath. *The Journal of Chemical Physics, 81*(8), 3684-3690. doi:10.1063/1.448118

Berendsen, H. J. C., Postma, J. P. M., van Gunsteren, W. F., & Hermans, J. (1981). Interaction Models for Water in Relation to Protein Hydration. In B. Pullman (Ed.), *Intermolecular Forces: Proceedings of the Fourteenth Jerusalem Symposium on Quantum Chemistry and Biochemistry Held in Jerusalem, Israel, April 13–16, 1981* (pp. 331-342). Dordrecht: Springer Netherlands.

Berthelot, D. (1898). Sur le mélange des gaz. *Comptes rendus hebdomadaires des séances de l'Académie des Sciences, 126*, 1703-1855.

Bikkina, P. K. (2011). Contact angle measurements of CO2-water-quartz/calcite systems in the perspective of carbon sequestration. *International Journal of Greenhouse Gas Control, 5*(5), 1259-1271. doi:https://doi.org/10.1016/j.ijggc.2011.07.001

Bleiziffer, P., Schaller, K., & Riniker, S. (2018). Machine Learning of Partial Charges Derived from High-Quality Quantum-Mechanical Calculations. *Journal of Chemical Information and Modeling, 58*(3), 579-590. doi:10.1021/acs.jcim.7b00663

Blöchl, P. E. (1994). Projector augmented-wave method. *Physical Review B, 50*(24), 17953-17979. doi:10.1103/PhysRevB.50.17953

Bracco, G., & Holst, B. (2013). *Surface Science Techniques*: Springer.

Broseta, D., Tonnet, N., & Shah, V. (2012). Are rocks still water-wet in the presence of dense CO2 or H2S? *Geofluids, 12*(4), 280-294. doi:10.1111/j.1468-8123.2012.00369.x

Broyden, C. G. (1970). The Convergence of a Class of Double-rank Minimization Algorithms 1. General Considerations. *IMA Journal of Applied Mathematics, 6*(1), 76-90. doi:10.1093/imamat/6.1.76

Buckingham, R. A. (1938). The classical equation of state of gaseous helium, neon and argon. *Proceedings of the Royal Society of London. Series A. Mathematical and Physical Sciences, 168*(933), 264-283. doi:10.1098/rspa.1938.0173

Bush, I. J., Todorov, I. T., & Smith, W. (2006). A DAFT DL_POLY distributed memory adaptation of the Smoothed Particle Mesh Ewald method. *Computer Physics Communications, 175*(5), 323-329. doi:https://doi.org/10.1016/j.cpc.2006.05.001

Cassie, A. B. D., & Baxter, S. (1944). Wettability of porous surfaces. *Transactions of the Faraday Society, 40*(0), 546-551. doi:10.1039/TF9444000546

Cerutti, D. S., Rice, J. E., Swope, W. C., & Case, D. A. (2013). Derivation of Fixed Partial Charges for Amino Acids Accommodating a Specific Water Model and Implicit Polarization. *The journal of physical chemistry. B, 117*(8), 2328-2338. doi:10.1021/jp311851r

Chen, C., Chai, Z., Shen, W., & Li, W. (2018). Effects of Impurities on CO2 Sequestration in Saline Aquifers: Perspective of Interfacial Tension and Wettability. *Industrial & Engineering Chemistry Research, 57*(1), 371-379. doi:10.1021/acs.iecr.7b03873

Chen, C., Chai, Z., Shen, W., Li, W., & Song, Y. (2017). Wettability of Supercritical CO2–Brine–Mineral: The Effects of Ion Type and Salinity. *Energy & Fuels, 31*(7), 7317-7324. doi:10.1021/acs.energyfuels.7b00840

Chen, C., Wan, J., Li, W., & Song, Y. (2015). Water contact angles on quartz surfaces under supercritical CO2 sequestration conditions: Experimental and molecular dynamics simulation studies. *International Journal of Greenhouse Gas Control, 42*, 655-665. doi:https://doi.org/10.1016/j.ijggc.2015.09.019

Chen, C., Zhang, N., Li, W., & Song, Y. (2015). Water Contact Angle Dependence with Hydroxyl Functional Groups on Silica Surfaces under CO2 Sequestration Conditions. *Environmental Science & Technology, 49*(24), 14680-14687. doi:10.1021/acs.est.5b03646

Chen, Y.-W., Cao, C., & Cheng, H.-P. (2008). Finding stable α-quartz (0001) surface structures via simulations. *Applied Physics Letters, 93*(18), 181911. doi:10.1063/1.3021398

Cygan, R. T., Liang, J.-J., & Kalinichev, A. G. (2004). Molecular Models of Hydroxide, Oxyhydroxide, and Clay Phases and the Development of a General Force Field. *The Journal of Physical Chemistry B, 108*(4), 1255-1266. doi:10.1021/jp0363287

Dake, L. P. (1978). *Fundamentals of reservoir engineering*: Elsevier Scientific Publishing Company.

Darden, T., York, D., & Pedersen, L. (1993). Particle mesh Ewald: An N·log(N) method for Ewald sums in large systems. *The Journal of Chemical Physics, 98*(12), 10089-10092. doi:10.1063/1.464397

de Leeuw, N. H., Higgins, F. M., & Parker, S. C. (1999). Modeling the Surface Structure and Stability of α-Quartz. *The Journal of Physical Chemistry B, 103*(8), 1270-1277. doi:10.1021/jp983239z

Demuth, T., Jeanvoine, Y., Hafner, J., & Ángyán, J. G. (1999). Polymorphism in silica studied in the local density and generalized-gradient approximations. *Journal of Physics: Condensed Matter, 11*(19), 3833.

Deng, Y., Xu, L., Lu, H., Wang, H., & Shi, Y. (2018). Direct measurement of the contact angle of water droplet on quartz in a reservoir rock with atomic force microscopy. *Chemical Engineering Science, 177*, 445-454. doi:https://doi.org/10.1016/j.ces.2017.12.002

Drelich, J., Miller, J. D., & Good, R. J. (1996). The Effect of Drop (Bubble) Size on Advancing and Receding Contact Angles for Heterogeneous and Rough Solid Surfaces as Observed with Sessile-Drop and Captive-Bubble Techniques. *Journal of Colloid and Interface Science, 179*(1), 37-50. doi:https://doi.org/10.1006/jcis.1996.0186

Eder, S. D., Fladischer, K., Yeandel, S. R., Lelarge, A., Parker, S. C., Søndergård, E., & Holst, B. (2015). A Giant Reconstruction of α-quartz (0001) Interpreted as Three Domains of Nano Dauphine Twins. *Scientific Reports, 5*, 14545. doi:10.1038/srep14545

Emami, F. S., Puddu, V., Berry, R. J., Varshney, V., Patwardhan, S. V., Perry, C. C., & Heinz, H. (2014). Force Field and a Surface Model Database for Silica to Simulate Interfacial Properties in Atomic Resolution. *Chemistry of Materials, 26*(8), 2647-2658. doi:10.1021/cm500365c

Ernzerhof, M., & Scuseria, G. E. (1999). Assessment of the Perdew–Burke–Ernzerhof exchange-correlation functional. *The Journal of Chemical Physics, 110*(11), 5029-5036. doi:10.1063/1.478401

Espinoza, D. N., & Santamarina, J. C. (2010). Water-CO2-mineral systems: Interfacial tension, contact angle, and diffusion—Implications to CO2 geological storage. *Water Resources Research, 46*(7). doi:10.1029/2009WR008634

Essmann, U., Perera, L., Berkowitz, M. L., Darden, T., Lee, H., & Pedersen, L. G. (1995). A smooth particle mesh Ewald method. *The Journal of Chemical Physics, 103*(19), 8577-8593. doi:10.1063/1.470117

Ewald, P. P. (1921). Die Berechnung optischer und elektrostatischer Gitterpotentiale. *Annalen der Physik, 369*(3), 253-287. doi:10.1002/andp.19213690304

Feya, O. D., Wang, Q., Lepeshkin, S. V., Baturin, V. S., Uspenskii, Y. A., & Oganov, A. R. (2018). Tetrahedral honeycomb surface reconstructions of quartz, cristobalite and stishovite. *Scientific Reports, 8*(1), 11947. doi:10.1038/s41598-018-29853-1

Fletcher, R. (1970). A new approach to variable metric algorithms. *The Computer Journal, 13*(3), 317-322. doi:10.1093/comjnl/13.3.317

Franks, F. (2000). *Water: A Matrix of Life: Edition 2*: The Royal Society of Chemistry.

Garcia, R., Osborne, K., & Subashi, E. (2008). Validity of the “Sharp-Kink Approximation” for Water and Other Fluids. *The Journal of Physical Chemistry B, 112*(27), 8114-8119. doi:10.1021/jp712181m

Garcia, R., Osborne, K., & Subashi, E. (2009). Validity of the “Sharp-Kink Approximation” for Water and Other Fluids. *The Journal of Physical Chemistry B, 113*(23), 8199-8199. doi:10.1021/jp903787d

GCCSI. (2018). The Global Status of CCS.

Giannozzi, P., Andreussi, O., Brumme, T., Bunau, O., Nardelli, M. B., Calandra, M., . . . Baroni, S. (2017). Advanced capabilities for materials modelling with Q uantum ESPRESSO. *Journal of Physics: Condensed Matter, 29*(46), 465901.

Giannozzi, P., Baroni, S., Bonini, N., Calandra, M., Car, R., Cavazzoni, C., . . . Wentzcovitch Renata, M. (2009). QUANTUM ESPRESSO: a modular and open-source software project for quantum simulations of materials. *Journal of Physics: Condensed Matter, 21*(39), 395502.

Gill, P. M. W. (1998). *Encyclopedia of Computational Chemistry* (Vol. 1): John Wiley & Sons.

Giovambattista, N., Debenedetti, P. G., & Rossky, P. J. (2007). Effect of Surface Polarity on Water Contact Angle and Interfacial Hydration Structure. *The Journal of Physical Chemistry B, 111*(32), 9581-9587. doi:10.1021/jp071957s

Goldfarb, D. (1970). A Family of Variable-Metric Methods Derived by Variational Means. *Mathematics of Computation, 24*(109), 23-26. doi:https://doi.org/10.1090/S0025-5718-1970-0258249-6

Gonzalez, M. A. (2011). Force fields and molecular dynamics simulations. *JDN 18 - Neutrons et Simulations, 12*, 169-200. doi:https://doi.org/10.1051/sfn/201112009

Goumans, T. P. M., Wander, A., Brown, W. A., & Catlow, C. R. A. (2007). Structure and stability of the (001) α-quartz surface. *Physical Chemistry Chemical Physics, 9*(17), 2146-2152. doi:10.1039/B701176H

Hager, W. H. (2012). Wilfrid Noel Bond and the Bond number. *Journal of Hydraulic Research, 50*(1), 3-9. doi:10.1080/00221686.2011.649839

Harris, J. G., & Yung, K. H. (1995). Carbon Dioxide's Liquid-Vapor Coexistence Curve And Critical Properties as Predicted by a Simple Molecular Model. *The Journal of Physical Chemistry, 99*(31), 12021-12024. doi:10.1021/j100031a034

Hebach, A., Oberhof, A., Dahmen, N., Kögel, A., Ederer, H., & Dinjus, E. (2002). Interfacial Tension at Elevated PressuresMeasurements and Correlations in the Water + Carbon Dioxide System. *Journal of Chemical & Engineering Data, 47*(6), 1540-1546. doi:10.1021/je025569p

Henkelman, G., Arnaldsson, A., & Jónsson, H. (2006). A fast and robust algorithm for Bader decomposition of charge density. *Computational Materials Science, 36*(3), 354-360. doi:https://doi.org/10.1016/j.commatsci.2005.04.010

Hohenberg, P., & Kohn, W. (1964). Inhomogeneous Electron Gas. *Physical Review, 136*(3B), B864-B871. doi:10.1103/PhysRev.136.B864

Hoover, W. G. (1985). Canonical dynamics: Equilibrium phase-space distributions. *Physical Review A, 31*(3), 1695-1697. doi:10.1103/PhysRevA.31.1695

Humphrey, W., Dalke, A., & Schulten, K. (1996). VMD: Visual molecular dynamics. *Journal of Molecular Graphics, 14*(1), 33-38. doi:https://doi.org/10.1016/0263-7855(96)00018-5

Iglauer, S. (2017). CO2–Water–Rock Wettability: Variability, Influencing Factors, and Implications for CO2 Geostorage. *Accounts of Chemical Research, 50*(5), 1134-1142. doi:10.1021/acs.accounts.6b00602

Iglauer, S., Al-Yaseri, A. Z., Rezaee, R., & Lebedev, M. (2015). CO2 wettability of caprocks: Implications for structural storage capacity and containment security. *Geophysical Research Letters, 42*(21), 9279-9284. doi:10.1002/2015GL065787

Iglauer, S., Mathew, M. S., & Bresme, F. (2012). Molecular dynamics computations of brine–CO2 interfacial tensions and brine–CO2–quartz contact angles and their effects on structural and residual trapping mechanisms in carbon geo-sequestration. *Journal of Colloid and Interface Science, 386*(1), 405-414. doi:https://doi.org/10.1016/j.jcis.2012.06.052

Iglauer, S., Pentland, C. H., & Busch, A. (2014). CO2 wettability of seal and reservoir rocks and the implications for carbon geo-sequestration. *Water Resources Research, 51*(1), 729-774. doi:10.1002/2014WR015553

Iler, R. K. (1979). *The Chemistry of Silica: Solubility, Polymerization, Colloid and Surface Properties and Biochemistry of Silica*: John Wiley & Sons (Wiley-Interscience Publication).

IPCC. (2005). *Carbon Dioxide Capture and Storage*. Retrieved from https://www.ipcc.ch/report/srccs/

IPCC. (2013). *Climate Change 2013: The Physical Science Basis*. Retrieved from https://www.ipcc.ch/report/ar5/wg1/

IPCC. (2014). *Climate Change 2014: Mitigation of Climate Change*. Retrieved from https://www.ipcc.ch/report/ar5/wg3/

IPCC. (2018). *Global Warming of 1.5 °C*. Retrieved from http://www.ipcc.ch/report/sr15/

Javanbakht, G., Sedghi, M., Welch, W., & Goual, L. (2015). Molecular Dynamics Simulations of CO2/Water/Quartz Interfacial Properties: Impact of CO2 Dissolution in Water. *Langmuir, 31*(21), 5812-5819. doi:10.1021/acs.langmuir.5b00445

Jones, J. E. (1924). On the determination of molecular fields. - II. From the equation of state of a gas. *Proceedings of the Royal Society of London. Series A, 106*(738), 463-477. doi:10.1098/rspa.1924.0082

Kaveh, N. S., Rudolph, E. S. J., van Hemert, P., Rossen, W. R., & Wolf, K. H. (2014). Wettability Evaluation of a CO2/Water/Bentheimer Sandstone System: Contact Angle, Dissolution, and Bubble Size. *Energy & Fuels, 28*(6), 4002-4020. doi:10.1021/ef500034j

Keffer, D. (2016). *Structural Properties from Molecular Dynamics Simulation*.

Koh, P. T. L., Hao, F. P., Smith, L. K., Chau, T. T., & Bruckard, W. J. (2009). The effect of particle shape and hydrophobicity in flotation. *International Journal of Mineral Processing, 93*(2), 128-134. doi:https://doi.org/10.1016/j.minpro.2009.07.007

Kohn, W., & Sham, L. J. (1965). Self-Consistent Equations Including Exchange and Correlation Effects. *Physical Review, 140*(4A), A1133-A1138. doi:10.1103/PhysRev.140.A1133

Lamb, R. N., & Furlong, D. N. (1982). Controlled wettability of quartz surfaces. *Journal of the Chemical Society, Faraday Transactions 1: Physical Chemistry in Condensed Phases, 78*(1), 61-73. doi:10.1039/F19827800061

Leach, A. R. (2001). *Molecular Modelling: Principles and Applications*.

Levien, L., Prewitt, C. T., & Weidner, D. J. (1980). Structure and elastic properties of quartz at pressure. *American Mineralogist, 65*(9-10), 920-930.

Liang, Y., Tsuji, S., Jia, J., Tsuji, T., & Matsuoka, T. (2017). Modeling CO2–Water–Mineral Wettability and Mineralization for Carbon Geosequestration. *Accounts of Chemical Research, 50*(7), 1530-1540. doi:10.1021/acs.accounts.7b00049

Liu, S., Yang, X., & Qin, Y. (2010). Molecular dynamics simulation of wetting behavior at CO2/water/solid interfaces. *Chinese Science Bulletin, 55*(21), 2252-2257. doi:10.1007/s11434-010-3287-0

Lorentz, H. A. (1881). Ueber die Anwendung des Satzes vom Virial in der kinetischen Theorie der Gase. *Annalen der Physik, 248*(1), 127-136. doi:10.1002/andp.18812480110

Malyi, O. I., Kulish, V. V., & Persson, C. (2014). In search of new reconstructions of (001) α-quartz surface: a first principles study. *RSC Advances, 4*(98), 55599-55603. doi:10.1039/C4RA10726H

Marshall, C. P., & Fairbridge, R. W. (1999). *Encyclopedia of Geochemistry*: Springer.

Mautner, M. N., Abdelsayed, V., El-Shall, M. S., Thrower, J. D., Green, S. D., Collings, M. P., & McCoustra, M. R. S. (2006). Meteorite nanoparticles as models for interstellar grains: Synthesis and preliminary characterisation. *Faraday Discussions, 133*(0), 103-112. doi:10.1039/B518207G

Mayo, S. L., Olafson, B. D., & Goddard, W. A. (1990). DREIDING: a generic force field for molecular simulations. *The Journal of Physical Chemistry, 94*(26), 8897-8909. doi:10.1021/j100389a010

Mazur, A. K. (1997). Common Molecular Dynamics Algorithms Revisited: Accuracy and Optimal Time Steps of Störmer–Leapfrog Integrators. *Journal of Computational Physics, 136*(2), 354-365. doi:https://doi.org/10.1006/jcph.1997.5740

Mazurek, A., Pogorzelski, S. J., & Boniewicz-Szmyt, K. (2009). Adsorption of natural surfactants present in sea waters at surfaces of minerals: contact angle measurements. *v. 51*.

McCaughan, J., Iglauer, S., & Bresme, F. (2013). Molecular Dynamics Simulation of Water/CO2-quartz Interfacial Properties: Application to Subsurface Gas Injection. *Energy Procedia, 37*, 5387-5402. doi:https://doi.org/10.1016/j.egypro.2013.06.457

Momma, K., & Izumi, F. (2008). VESTA: a three-dimensional visualization system for electronic and structural analysis. *Journal of Applied Crystallography, 41*(3), 653-658. doi:10.1107/S0021889808012016

Monkhorst, H. J., & Pack, J. D. (1976). Special points for Brillouin-zone integrations. *Physical Review B, 13*(12), 5188-5192. doi:10.1103/PhysRevB.13.5188

Mulliken, R. S. (1955). Electronic Population Analysis on LCAO–MO Molecular Wave Functions. I. *The Journal of Chemical Physics, 23*(10), 1833-1840. doi:10.1063/1.1740588

Murashov, V. V. (2005). Reconstruction of Pristine and Hydrolyzed Quartz Surfaces. *The Journal of Physical Chemistry B, 109*(9), 4144-4151. doi:10.1021/jp0402075

Nash, T., Allison, A. C., & Harington, J. S. (1966). Physico-Chemical Properties of Silica in Relation to its Toxicity. *Nature, 210*, 259. doi:10.1038/210259a0

Nosé, S. (1984). A molecular dynamics method for simulations in the canonical ensemble. *Molecular Physics, 52*(2), 255-268. doi:10.1080/00268978400101201

Perdew, J. P., Burke, K., & Ernzerhof, M. (1996). Generalized Gradient Approximation Made Simple. *Physical Review Letters, 77*(18), 3865-3868. doi:10.1103/PhysRevLett.77.3865

Perdew, J. P., Chevary, J. A., Vosko, S. H., Jackson, K. A., Pederson, M. R., Singh, D. J., & Fiolhais, C. (1992). Atoms, molecules, solids, and surfaces: Applications of the generalized gradient approximation for exchange and correlation. *Physical Review B, 46*(11), 6671-6687. doi:10.1103/PhysRevB.46.6671

Perdew, J. P., & Yue, W. (1986). Accurate and simple density functional for the electronic exchange energy: Generalized gradient approximation. *Physical Review B, 33*(12), 8800-8802. doi:10.1103/PhysRevB.33.8800

Piela, L. (2007). *Ideas of Quantum Chemistry*: Elsevier.

Piela, L. (2014). Appendix S - Population Analysis. In L. Piela (Ed.), *Ideas of Quantum Chemistry (Second Edition)* (pp. e143-e147). Oxford: Elsevier.

Roshan, H., Al-Yaseri, A. Z., Sarmadivaleh, M., & Iglauer, S. (2016). On wettability of shale rocks. *Journal of Colloid and Interface Science, 475*, 104-111. doi:https://doi.org/10.1016/j.jcis.2016.04.041

Ryckaert, J.-P., Ciccotti, G., & Berendsen, H. J. C. (1977). Numerical integration of the cartesian equations of motion of a system with constraints: molecular dynamics of n-alkanes. *Journal of Computational Physics, 23*(3), 327-341. doi:https://doi.org/10.1016/0021-9991(77)90098-5

Sanville, E., Kenny, S. D., Smith, R., & Henkelman, G. (2007). Improved grid-based algorithm for Bader charge allocation. *Journal of Computational Chemistry, 28*(5), 899-908. doi:10.1002/jcc.20575

Saraji, S., Goual, L., Piri, M., & Plancher, H. (2013). Wettability of Supercritical Carbon Dioxide/Water/Quartz Systems: Simultaneous Measurement of Contact Angle and Interfacial Tension at Reservoir Conditions. *Langmuir, 29*(23), 6856-6866. doi:10.1021/la3050863

Sarmadivaleh, M., Al-Yaseri, A. Z., & Iglauer, S. (2015). Influence of temperature and pressure on quartz–water–CO2 contact angle and CO2–water interfacial tension. *Journal of Colloid and Interface Science, 441*, 59-64. doi:https://doi.org/10.1016/j.jcis.2014.11.010

scripps.ucsd.edu. The Scripps CO2 Program. Retrieved from https://scripps.ucsd.edu/programs/keelingcurve/2018/05/02/carbon-dioxide-in-the-atmosphere-hits-record-high-monthly-average/

serc.carleton.edu. Metamorphic P-T Phase Diagrams. Retrieved from https://serc.carleton.edu/research_education/equilibria/metamorphic_diagrams.html

Shanno, D. F. (1970). Conditioning of Quasi-Newton Methods for Function Minimization. *Mathematics of Computation, 24*(111), 647-656. doi:https://doi.org/10.1090/S0025-5718-1970-0274029-X

Sklodowska, A., & Matlakowska, R. (1997). Influence of exopolymers produced by bacterial cells on hydrophobicity of substrate surface. *Biotechnology Techniques, 11*(11), 837-840. doi:10.1023/A:1018437627618

Span, R., & Wagner, W. (1996). A New Equation of State for Carbon Dioxide Covering the Fluid Region from the Triple-Point Temperature to 1100 K at Pressures up to 800 MPa. *Journal of Physical and Chemical Reference Data, 25*(6), 1509-1596. doi:10.1063/1.555991

Swamy, V., Saxena, S. K., Sundman, B., & Zhang, J. (1994). A thermodynamic assessment of silica phase diagram. *Journal of Geophysical Research: Solid Earth, 99*(B6), 11787-11794. doi:10.1029/93JB02968

Swope, W. C., Andersen, H. C., Berens, P. H., & Wilson, K. R. (1982). A computer simulation method for the calculation of equilibrium constants for the formation of physical clusters of molecules: Application to small water clusters. *The Journal of Chemical Physics, 76*(1), 637-649. doi:10.1063/1.442716

Tang, W., Sanville, E., & Henkelman, G. (2009). A grid-based Bader analysis algorithm without lattice bias. *Journal of Physics: Condensed Matter, 21*(8), 084204.

Tenney, C. M., & Cygan, R. T. (2014). Molecular Simulation of Carbon Dioxide, Brine, and Clay Mineral Interactions and Determination of Contact Angles. *Environmental Science & Technology, 48*(3), 2035-2042. doi:10.1021/es404075k

Todorov, I. T., & Smith, W. (2016). *The DL_POLY_4 user manual. Version 4.08*. Retrieved from https://www.scd.stfc.ac.uk/Pages/DL_POLY.aspx

Todorov, I. T., Smith, W., Trachenko, K., & Dove, M. T. (2006). DL_POLY_3: new dimensions in molecular dynamics simulations via massive parallelism. *Journal of Materials Chemistry, 16*(20), 1911-1918. doi:10.1039/B517931A

Tsuji, S., Liang, Y., Kunieda, M., Takahashi, S., & Matsuoka, T. (2013). Molecular Dynamics Simulations of the CO2-Water-silica Interfacial Systems. *Energy Procedia, 37*, 5435-5442. doi:https://doi.org/10.1016/j.egypro.2013.06.462

van Beest, B. W. H., Kramer, G. J., & van Santen, R. A. (1990). Force fields for silicas and aluminophosphates based on ab initio calculations. *Physical Review Letters, 64*(16), 1955-1958. doi:10.1103/PhysRevLett.64.1955

Verlet, L. (1967). Computer "Experiments" on Classical Fluids. I. Thermodynamical Properties of Lennard-Jones Molecules. *Physical Review, 159*(1), 98-103. doi:10.1103/PhysRev.159.98

Wang, D.-M., Xu, Y.-M., He, D.-M., Guan, J., & Zhang, O.-M. (2009). Investigation of mineral composition of oil shale. *Asia-Pacific Journal of Chemical Engineering, 4*(5), 691-697. doi:10.1002/apj.319

Wang, Y., & Perdew, J. P. (1991). Spin scaling of the electron-gas correlation energy in the high-density limit. *Physical Review B, 43*(11), 8911-8916. doi:10.1103/PhysRevB.43.8911

webbook.nist.gov. NIST Chemistry WebBook. Retrieved from https://webbook.nist.gov/chemistry/

Wenzel, R. N. (1936). RESISTANCE OF SOLID SURFACES TO WETTING BY WATER. *Industrial & Engineering Chemistry, 28*(8), 988-994. doi:10.1021/ie50320a024

Wigner, E. (1938). Effects of the electron interaction on the energy levels of electrons in metals. *Transactions of the Faraday Society, 34*(0), 678-685. doi:10.1039/TF9383400678

www.bbc.com. Final call to save the world from 'climate catastrophe'. Retrieved from https://www.bbc.com/news/science-environment-45775309

www.chemicalogic.com. Carbon Dioxide Phase Diagram. Retrieved from http://www.chemicalogic.com/Pages/DownloadPhaseDiagrams.html

www.energy.psu.edu. CO2 Calculator. A web computational tool. Retrieved from http://www.energy.psu.edu/tools/CO2-EOS/

www.globalccsinstitute.com. The Global CCS Institute. Retrieved from www.globalccsinstitute.com

www.quantum-espresso.org. Quantum ESPRESSO. Retrieved from www.quantum-espresso.org

Yang, J., & Wang, E. G. (2006). Water adsorption on hydroxylated alpha-quartz (0001) surfaces: From monomer to flat bilayer. *Physical Review B, 73*(3), 035406. doi:10.1103/PhysRevB.73.035406

Yu, M., & Trinkle, D. R. (2011). Accurate and efficient algorithm for Bader charge integration. *The Journal of Chemical Physics, 134*(6), 064111. doi:10.1063/1.3553716

Zhuravlev, L. T. (2000). The surface chemistry of amorphous silica. Zhuravlev model. *Colloids and Surfaces A: Physicochemical and Engineering Aspects, 173*(1), 1-38. doi:https://doi.org/10.1016/S0927-7757(00)00556-2